Adaptive Filter for Harmonic Suppression for Sensorless PMSM Drives

Emil Christiansen & Kasper Juul Clausen

Mechatronic Control Engineering, MCE4-1025

STUDENT REPORT

AALBORG UNIVERSITY

AALBORG UNIVERSITY

STUDENT REPORT

Title:
Adaptive Filter for Harmonic Suppression
for Sensorless PMSM Drives

Theme:
Master's Thesis

Project Period:
Spring Semester 2023

Project Group:
MCE4-1025

Participant(s):
Emil Christiansen
Kasper Juul Clausen

Supervisor(s):
Dong Wang

Page Numbers: 95

Date of Completion:
June 2, 2023

Abstract:

Sensorless control of permanent magnet synchronous motors (PMSMs) requires accurate rotor position estimation. However, due to inverter nonlinearity and flux spatial harmonics, (6 ± 1)th order harmonic distortion in the estimated back-EMF corresponding to 6th order ripples in the estimated position and speed appears. This thesis presents a complex coefficient synchronous frequency filter (CCSFF) and a bilinear recursive least squares (BRLS) adaptive filter to suppress the 6th order harmonics in the estimated position and speed. The influence of the parameter design of the respective methods is analyzed, and the methods are experimentally verified. Sufficient 6th order harmonic suppression in various steady state conditions is obtained using the CCSFF, with the harmonic suppression capability improved as speed increases. An adaptive approach to the parameter design of the CCSFF ensures fine dynamic performance. The BRLS adaptive filter ensures better harmonic suppression capability in various steady state conditions by tracking and compensating the specified harmonic components in the estimated back-EMF without affecting the system's dynamic performance.

Summary

This master's thesis concerns sensorless control of permanent magnet synchronous motors (PMSMs). Sensorless control of PMSMs requires accurate position and speed estimation. Due to voltage source inverter (VSI) nonlinearities and flux spatial harmonics, the estimated back-EMF is distorted by (6 ± 1)th order harmonics. The (6 ± 1)th order harmonic in the estimated back-EMF will introduce 6th order harmonics in the estimated position and speed, which may affect the performance of the sensorless control. In this thesis, two filters are proposed to suppress the harmonics caused by inverter nonlinearities and flux spatial harmonics. The two methods are implemented in a sensorless field oriented control (FOC) structure with a back-EMF based position estimator, including a closed-loop flux observer (CLFO) and a phase-locked loop (PLL). The idea is to detect and suppress (6 ± 1)th order harmonic in the estimated flux, hence the 6th order harmonics in the estimated position and speed. The filter methods are analyzed and experimentally verified using a laboratory setup.

An analysis of measured current, estimated flux, estimated rotor position, and estimated speed from the laboratory are performed to examine the effects of the inverter nonlinearities and flux spatial harmonics. The analysis shows obvious (6 ± 1)th order harmonics in the measured currents and estimated flux. Furthermore, obvious 6th order harmonic ripples are seen in the estimated position and speed.

The first filter is a complex coefficient synchronous frequency filter (CCSFF) with zero phase shift in steady state. Combining the CCSFF with a PLL shows great potential in suppressing the (6 ± 1)th order harmonic in the estimated flux. The suppression capability is strictly related to the operation speed and the bandwidth of the CCSFF. However, the bandwidth can be varied easily by adjusting the parameters. By lowering the bandwidth more sufficient harmonic suppression capability is achieved. However, the dynamic performance during transient is worsen, hence larger phase shift is present during speed and load variation. Adopting an adaptive approach to the CCSFF-PLL bandwidth, improves the dynamic performance of the CCSFF without affecting the filtering capability.

The second filter is a bilinear recursive least squares (BRLS) adaptive filter with zero phase shift in steady state. Combining the BRLS adaptive filter with the PLL shows even greater potential in suppressing the (6 ± 1)th order harmonic in a wide speed range compared to the CCSFF. The BRLS adaptive filter does not affect the dynamic performance, hence zero phase shift is added to the system during speed and load variations.

As both filters shows great suppression capability in the estimated position and speed, the influence of a more accurate position and speed estimation is examined. In low to mid speed range the improved position and speed estimation attenuate the (6 ± 1)th order harmonics distortion in the phase current as the current loop is capable of compensating for the ripples caused by inverter nonlinearities and flux spatial harmonics. However, the compensation is heavily affected by the operational speed and the current loop which is not capable of compensating for the ripples. Hence other methods may be considered to additionally improve the distortions in the currents.

Preface

This Master's thesis is made by group MCE4-1025 at the 10th semester at MSc. education in Mechatronic Control Engineering within the department AAU Energy at Aalborg University.

In this thesis, the Harvard method [Surname, Year] is used to refer to sources. At the end of the report, sources are listed alphabetically by surname.

Figures, tables, and equations are numbered in chronological order within the chapters, e.g. figure 1.2 means, chapter 1, figure 2. Equations are referenced in parentheses, e.g. (2.4). Chapters denoted by letters refer to appendixes which are placed at the end of the report.

The following software is used to draft this thesis:

- Draw.io - Used for figures and graphics.
- Matlab - Used for data processing.
- Overleaf - Used for word processing.
- Simulink - Used for model development and simulation.
- dSPACE - Used for implementation and testing with the laboratory setup.

Nomenclature

Abbreviation	Description
BRLS	Bilinear Recursive Least Square
CCSFF	Complex Coefficient Synchronous Frequency Filter
CLFO	Closed Loop Flux Observer
FFT	Fast Fourier Transform
FOC	Field Oriented Control
GUI	Graphical User Interface
IPMSM	Interior Permanent Magnet Synchronous Motor
PLL	Phase-locked Loop
PM	Permanent Magnet
PMSM	Permanent Magnet Synchronous Motor
SVM	Space Vector Modulation
VSI	Voltage Source Inverter

Symbol	Description	Unit
$\dot{\Box}$	Derivative with respect to time	[-]
$\hat{\Box}$	Estimated component	[-]
$\tilde{\Box}$	Error component	[-]
B	Viscous friction coefficient	$[\text{Nm} \cdot \text{s}]$
c	Constant	[-]
e	Back-EMF	[V]
$G_{j,i}$	Transfer function, where $j = p, c$ and $i = d, q, speed$	[-]
h	Index number	[-]
i_i	Current components in reference frame, where $i = a, b, c, d, q, \alpha, \beta$	[A]
J	Equivalent system inertia	$[\text{kg} \cdot \text{m}^2]$
k	Damping factor	[-]
$k_{i,j}$	Controller integral component, where $i = d, q, speed$	[-]
$k_{p,i}$	Controller proportional component, where $i = d, q, speed$	[-]
L_i	Synchronous inductance in reference frame, where $i = d, q$	[mH]
n_{pp}	Number of pole pairs	[-]
R_s	Single phase resistance	$[\Omega]$
S_D	Scaling factor	[-]
t	Time	[s]
T	Time period	[s]
T_d	Time delay	[s]
T_s	Switching period	[s]

Continues on next page

Symbol	Description	Unit
u_i	Voltage components in reference frame, where $i = a, b, c, d, q, \alpha, \beta$	[V]
$\boldsymbol{w}$	Filter coefficient vector	[-]
w_i	Variable for the derivation of filter structure in reference frame, where $i = \alpha, \beta$	[-]
z_i	Flux component in reference frame, where $i = \alpha, \beta$	[Wb]
τ_c	Coulomb torque coefficient	[Nm]
τ_f	Frictional torque	[Nm]
τ_e	Electromagnetic torque	[Nm]
τ_l	Load torque	[Nm]
λ	Forgetting factor	[-]
λ_{mpm}	Peak permanent magnet flux linkage	[Wb]
λ_i	Flux linkage components in reference frame, where $i = d, q, \alpha, \beta$	[Wb]
λ_{fi}	Fundamental flux linkage component in reference frame, where $i = \alpha, \beta$	[Wb]
λ_{hi}	Harmonic flux linkage component in reference frame, where $i = \alpha, \beta$	[Wb]
θ_e	Electrical rotor position	[rad]
ω_c	Bandwidth	[rad/s]
ω_e	Electrical rotor speed	[rad/s]
ω_m	Mechanical rotor speed	[rad/s]
ω_n	Natural frequency	[rad/s]
ϵ_i	Error signal component in reference frame, where $i = \alpha, \beta$	[Wb]
$\boldsymbol{\phi}$	Harmonic information vector	[-]
ϕ_m	Phase margin	[deg]
ζ	Damping ratio	[-]

Contents

Introduction 1

Permanent magnet synchronous motors (PMSMs) have gained traction in various industrial applications due to their characteristics such as high efficiency, high power density, and high torque to volume ratio. To use the PMSMs in different applications, an appropriate control structure is required. In such control systems, information on the rotor position of the PMSMs is essential to obtain accurate control performance. Besides costs, including an encoder or resolver as position feedback to the control system will increase the system size and reduce reliability. Thus, sensorless control methods have been extensively studied. There are two main categories within sensorless control which are based on the operational speed range of the PMSM application; high-frequency (HF) injection methods and back-EMF based methods. HF injection methods are utilized at zero and low speed, which is typically up to 10% of the rated speed of the PMSM [Wang et al., 2018],[Xie et al., 2016],[Seilmeier and Piepenbreier, 2015]. The HF injection methods utilize rotor saliency, hence the method is only applicable for interior PMSMs (IPMSMs). For the mid to high-speed range, typically back-EMF based control methods are utilized [Chen et al., 2020],[Wang et al., 2019],[Lee and Ha, 2012]. The back-EMF is proportional to the speed, hence the back-EMF is more reliable as the speed increases.

In the mid to high-speed range with the back-EMF based sensorless control, several methods for position estimation can be considered, including closed-loop flux observer (CLFO) [Wang et al., 2019],[Chen et al., 2020], Kalman filter [Dhaouadi et al., 1991],[Bolognani et al., 2003],[Allaoui et al., 2021], model reference adaptive system (MRAS) [Lin et al., 2019] or sliding mode observer (SMO) [Wu et al., 2020],[Wu et al., 2022].

In sensorless control systems for PMSMs typically only current measurements are available, hence the reference voltages may be used to estimate the rotor position dependent on the estimation method. When using a voltage source inverter (VSI), a voltage difference between the reference voltage from the control system and the actual output voltage of the VSI is present. This voltage difference can be considered as nonlinearities of the VSI. The nonlinearities of the VSI are caused by different characteristics such as dead time, switching delays, parasitic capacitance, and on-state voltages in the VSI. [Park and Sul, 2012] The inverter nonlinearities which cause the voltage difference may affect the performance of the sensorless control system. The nonlinearities of the inverter also affect the output current with harmonic distortions. Hence, the inverter nonlinearities can affect the performance of the control system. [Park and Sul, 2012]

The inverter nonlinearities cause distortion in the estimated back-EMF in the $\alpha\beta$ reference frame where the distortion is dominated by the (6 ± 1)th order harmonic components. These harmonic distortions in the estimated back-EMF will appear as a 6th order harmonic component in the estimated position and speed. The distortion in the position and speed estimation will affect the performance of the sensorless control system. Hence, different studies have been made to try to compensate for the voltage error of the inverter, caused

by nonlinearities. [Wu et al., 2020],[Park and Sul, 2012],[Kim et al., 2010]
However, even if the compensation of the inverter nonlinearities is performed perfectly (which in practice may be difficult to obtain), flux spatial harmonics will also cause (6 ± 1)th order harmonic distortion in the estimated back-EMF. Flux spatial harmonics are present due to a nonideal air-gap magnetic field in the PMSM. Hence, methods to detect and suppress the harmonic distortion caused both by the inverter nonlinearities and flux spatial harmonics may be considered. [Wu et al., 2020] [Wu et al., 2022]

To suppress the harmonic distortion in the estimated position and speed, caused both by the inverter nonlinearities and flux spatial harmonics, a filtering approach may be considered, to simply filter out the harmonics contained in the estimated back-EMF before this signal is used to estimate the rotor position and speed. Different filtering methods have been studied including resonant filters and adaptive filters. However, due to the phase characteristic of the resonant filter, its performance is sensitive to the resonant frequency. The resonant frequency may be difficult to track accurately in variable-speed drives during transients and load torque disturbance, which may degrade the performance of the sensorless control system for variable-speed PMSM drives. [Freijedo et al., 2011]
Adaptive filters seem to be the better choice for detecting and suppressing harmonic components due to their bandpass filtering characteristics and frequency adaptability. Different adaptive filters have been studied for harmonic detection and suppression. In Wu et al. [2022], a complex-coefficient synchronous frequency filter (CCSFF)-based sliding mode observer combined with a quadrature phase-locked loop is proposed to detect and suppress the estimated back-EMF distortion. According to Wu et al. [2022], the CCSFF possesses frequency adaptability and bandpass-filtering characteristics that eliminate the harmonic distortion, and a smooth back-EMF signal is obtained. This ensures improved position estimation, improving the control system's performance. Wu et al. [2020] propose a bilinear recursive least squares (BRLS) adaptive filter integrated into a sliding-mode position observer to suppress the dominant harmonic components in the estimated back-EMF. According to Wu et al. [2020], the BRLS filter has the ability to detect and suppress specified harmonic components in both steady-state and dynamic operational conditions. The filter is robust to variation in motor parameters, and the BRLS algorithm itself is independent of motor parameters.

1.1 Project specification

As previously described, dominating (6 ± 1)th order harmonic components are present in the estimated back-EMF, due to nonlinearities of the inverter and flux spatial harmonics. This corresponds to a 6th order harmonic component in the estimated position and speed, which affects the performance of sensorless control of PMSMs. It may be more convenient to use a filtering approach to eliminate the harmonic distortion rather than use voltage error compensation methods, due to also existing flux spatial harmonics. Adaptive filters have the ability to track the change in specified frequency components caused by changes in the working condition.

This leads to the following problem statement for the work of this thesis.
How can adaptive filters be used for suppression of the 6th order harmonic component in the estimated position and speed?

The adaptive filters proposed in [Wu et al., 2022] and [Wu et al., 2020] are in this thesis further examined for suppression of the 6th order harmonic component in the estimated position and speed. The two methods are compared based on the following criteria:

- Dynamic performance.
- Harmonic suppression capability at steady state.

To evaluate the adaptive filters, they are implemented in a sensorless Field-oriented control (FOC) based control system including a closed-loop flux observer (CLFO) and a phase-locked loop (PLL) for position estimation. The adaptive filters are verified through experimental tests using a laboratory test setup which is further described in section 1.2. The thesis includes an introduction to the sensorless control system and the position estimation method. Further, an analysis of the harmonics in the estimated back-EMF and its effect on the estimated position and speed is performed. The adaptive filters are analyzed and the parameter design is elaborated.

1.2   System description

The methods to suppress 6th order harmonics in the estimated position and speed are examined and evaluated based on experimental tests using the laboratory setup illustrated in figure 1.1. The schematic of the system with the connection of the different components is illustrated in figure 1.2
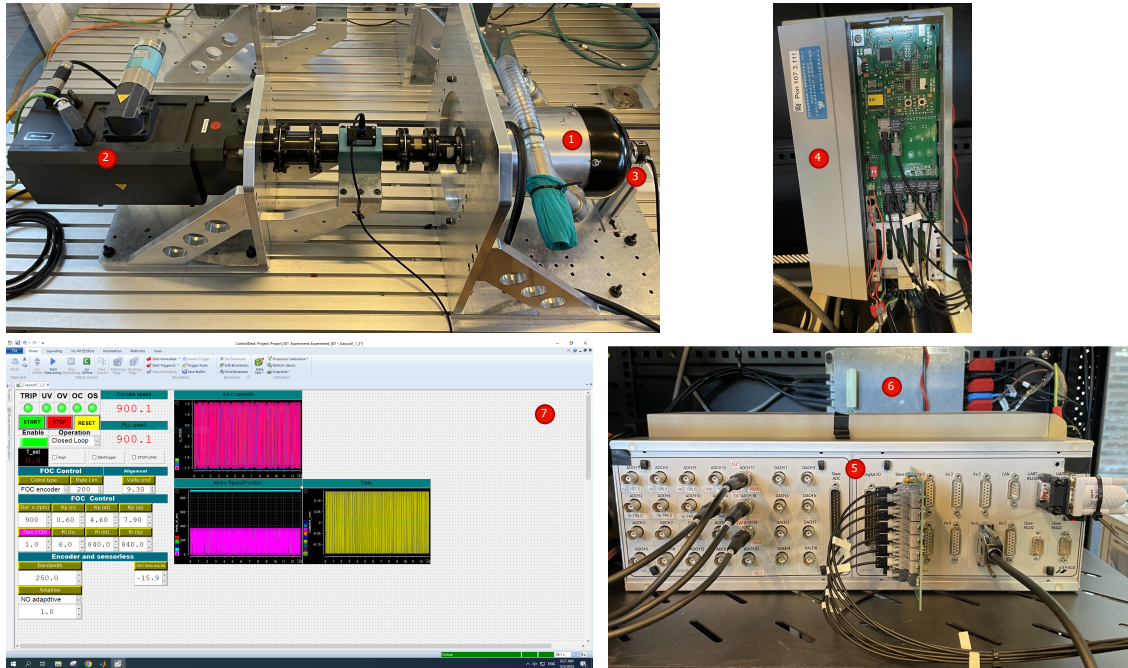

Figure 1.1. Test setup used for examination and evaluation of the harmonic suppression methods. 1. PMSM, 2. Programmable load motor, 3. Encoder, 4. Voltage Source Inverter, 5. dSPACE module, 6. Current sensor, 7. dSPACE Graphical User Interface.
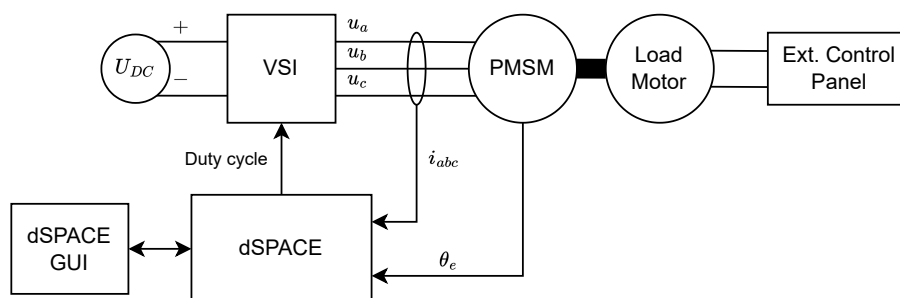

Figure 1.2. Schematic of the laboratory setup.

The PMSM is a three-pole pair $11\,\mathrm{kW}$ motor. Specifications and parameters are listed in table 1.1. An incremental encoder is connected to the shaft of the PMSM to obtain the position and speed information of the rotor. The encoder is primarily used to compare with the estimated rotor position and speed. The load motor can be operated in torque control to provide a desired load to the shaft of the PMSM during tests. Furthermore, the load motor can be operated in speed control to drive the PMSM, which is applicable for

different experimental tests such as parameter identification of the PMSM. The dSPACE module is used for digital signal processing and is based on Simulink environment. The dSPACE module is used to implement and apply the control structure and data collection. From the dSPACE Graphical User Interface (GUI) the control is operated and desired signals can be monitored during operation.

The Voltage Source Inverter (VSI) is a Danfoss inverter of type FC-302P7K5T5E20H1 with each output controlled individually by a duty cycle signal. The inverter parameters are listed in table 1.1.

PMSM			Inverter		
Parameter	Value	Unit	Parameter	Value	Unit
Rated power	11000	W	Maximum current	16	A
Rated speed	3600	rpm	Switching frequency	5	kHz
Rated torque	29.2	Nm	Dead time	2	μs
Rated current	16.8	Arms			
Rated voltage	380	Vrms			
n_{pp}	3	-			
R_s	0.36	Ω			
λ_{mpm}	0.1199	Wb			
L_d	1.99	mH			
L_q	3.40	mH			
B	$1.4 \cdot 10^{-3}$	Nm $\cdot$ s			
τ_c	0.5672	Nm			
J	$1.44 \cdot 10^{-2}$	kg $\cdot$ m^2			

Table 1.1. PMSM and inverter parameters. The parameters for the PMSM are obtained from previous studies [Christiansen and Clausen, 2022].

The specifications of the PMSM are provided by Aalborg University while the inverter specification is obtained from the nameplate. Accurate parameter identification is essential to obtain good control performance of the PMSM, as the majority of the designed control structure is based on these. Due to this, the PMSM parameters such as the single-phase electrical resistance R_s, the permanent magnet (PM) flux linkage λ_{mpm}, the d- and q-axis inductance, the inertia J, the viscous and Coulomb friction coefficients B, and τ_c are found experimental. The parameters are identified by performing different tests with the PMSM. As previous work has been carried out using the laboratory setup, the methods for identifying the model parameters are not presented in this thesis. However, the identified parameters obtained from previous studies are listed in table 1.1. Information about the identification methods used to obtain the model parameters is found in [Christiansen and Clausen, 2022].

Sensorless control 2

In this chapter, a sensorless FOC structure is presented to elaborate on the harmonic distortion in the estimated position and speed. Later the sensorless FOC is used together with the proposed filter methods. This chapter includes a mathematical model of the PMSM and a concept description of the FOC structure along with the design of the PI controllers. Furthermore, the structure of the position estimator is presented, including the CLFO, used to estimate the flux linkage based on the back-emf measurement, and a PLL, used to smoothen the estimated position and speed signal. The designed sensorless control structure is validated based on an experimental test with the laboratory setup. The obtained parameters used in the sensorless control structure are listed in table A.1.

2.1 PMSM model

To design the control structure applied in this thesis, the PMSM voltage equations and the equations of motions are introduced. The voltage equations of the PMSM in the dq reference frame are given in (2.1) [Krause et al., 2013].

$$u_d = R_s \cdot i_d + \dot{\lambda}_d - \omega_e \cdot \lambda_q$$
$$u_q = R_s \cdot i_q + \dot{\lambda}_q + \omega_e \cdot \lambda_d \tag{2.1}$$

Where u_d, u_q, i_d and i_q are the stator dq-axis voltages and currents respectively. R_s is the single phase resistance, λ_d and λ_q are the dq-axis flux linkages and ω_e is the electrical rotor speed. The dq-axis flux linkages are given in (2.2).

$$\lambda_d = L_d \cdot i_d + \lambda_{mpm} \qquad , \qquad \dot{\lambda}_d = L_d \cdot \dot{i}_d$$
$$\lambda_q = L_q \cdot i_q \qquad , \qquad \dot{\lambda}_q = L_q \cdot \dot{i}_q \tag{2.2}$$

Where L_d and L_q are the dq-axis inductances and λ_{mpm} is the rotor permanent magnet flux linkage.
The expression for the electromagnetic torque is given in (2.3) [Krause et al., 2013].

$$\tau_e = \frac{3}{2} \cdot n_{pp} \cdot (\lambda_d \cdot i_q - \lambda_q \cdot i_d) \tag{2.3}$$

Where n_{pp} is the number of pole pairs. Substituting (2.2) into (2.3) and rearranging, the electromagnetic torque is expressed as (2.4).

$$\tau_e = \frac{3}{2} \cdot n_{pp} \cdot (\lambda_{mpm} \cdot i_q + (L_d - L_q) \cdot i_q \cdot i_d) \tag{2.4}$$

The angular rotor speed is calculated in (2.5).

$$\dot{\omega}_m = \frac{\tau_e - \tau_f - \tau_l}{J} \tag{2.5}$$

Where ω_m is the mechanical rotor speed, τ_e is the electromagnetic torque, τ_f is the frictional torque, and τ_l is the load torque.

2.2 Sensorless FOC

The control structure considered in this thesis is based on sensorless FOC. The sensorless control scheme is illustrated in figure 2.1.

Figure 2.1. Sensorless FOC structure.

The sensorless FOC structure has a closed-loop speed control, utilizing two inner PI-based closed-loops to control the dq-currents. The FOC is used to orient the stator current vector in a synchronous rotating dq reference frame. The current vector is oriented on the q-axis, meaning the d-axis current is controlled to zero. The q-axis current is calculated using the speed control loop.

The FOC structure contains three PI controllers: One in each current loop and one in the speed loop. The PI controllers are designed based on the dynamics of the different control loops. The transfer functions of the three control loops are obtained using the PMSM voltage equations (2.1) and the equation of motion (2.5) along with the expression of the electromagnetic torque (2.4). For simplicity the back-EMF, Coulomb friction, and load torque are neglected. The transfer functions are shown in (2.6), (2.7) and (2.8).

$$G_{p,d} = \frac{i_d}{u_d} = \frac{1}{(s \cdot L_d + R_s) \cdot (s \cdot T_d + 1)} \tag{2.6}$$

$$G_{p,q} = \frac{i_q}{u_q} = \frac{1}{(s \cdot L_q + R_s) \cdot (s \cdot T_d + 1)} \tag{2.7}$$

$$G_{p,speed} = \frac{\omega_m}{i_q} = \frac{3 \cdot n_{pp} \cdot \lambda_{mpm}}{2} \cdot \frac{1}{(s \cdot J + B)} \tag{2.8}$$

Where T_d is a modeled time delay given as $T_d = 1.5 \cdot T_s$ with T_s representing the switching period. These delays are due to the digital implementation of the control which implies the sampling of signals and the processing of the control algorithm [Zigmund et al., 2011].

For the two current loops it is desired to achieve similar responses, thus the bandwidth of the two control loops is designed to be similar. As seen from (2.6) and (2.7) the two current loops have a common pole located at $-\frac{1}{T_d}$ due to the modeled delay. However, the location of the second pole is different for the two systems due to the difference in the dq-inductances. Hence, to achieve similar current responses, the PI controller design for the respective current loops is different. The PI controllers are designed based on a pole/zero cancellation methodology, whereof the zero of the PI controller is placed at the pole location $-\frac{R_s}{L_{dq}}$ to cancel the dynamics caused by this pole. By analyzing the dynamics of the two current loops, the controllers in (2.9) and (2.10) are obtained for the i_d and i_q current loop, respectively. The controllers are designed with the criteria of a desired bandwidth $\omega_c \approx 2000 \, \text{rad/s}$. When $\omega_c \approx 2000 \, \text{rad/s}$ the systems phase margins become $\phi_m \approx 55°$ which is a good trade-off between stability and rise time [Lina et al., 2014].

$$G_{c,d} = k_{i,d} \cdot \frac{\frac{k_{p,d}}{k_{i,d}} \cdot s + 1}{s} = 840 \cdot \frac{0.0055 \cdot s + 1}{s} \tag{2.9}$$

$$G_{c,q} = k_{i,q} \cdot \frac{\frac{k_{p,q}}{k_{i,q}} \cdot s + 1}{s} = 840 \cdot \frac{0.0094 \cdot s + 1}{s} \tag{2.10}$$

The designed PI controllers are implemented in the control structure using the laboratory setup. The current response for i_d and i_q are examined individually. A test is performed by making a step change in the current reference for the respective current component while the opposite current component is controlled to zero. Figure 2.2 illustrates the dq-current responses with the PI controllers given in (2.9) and (2.10) from tests using the laboratory setup.
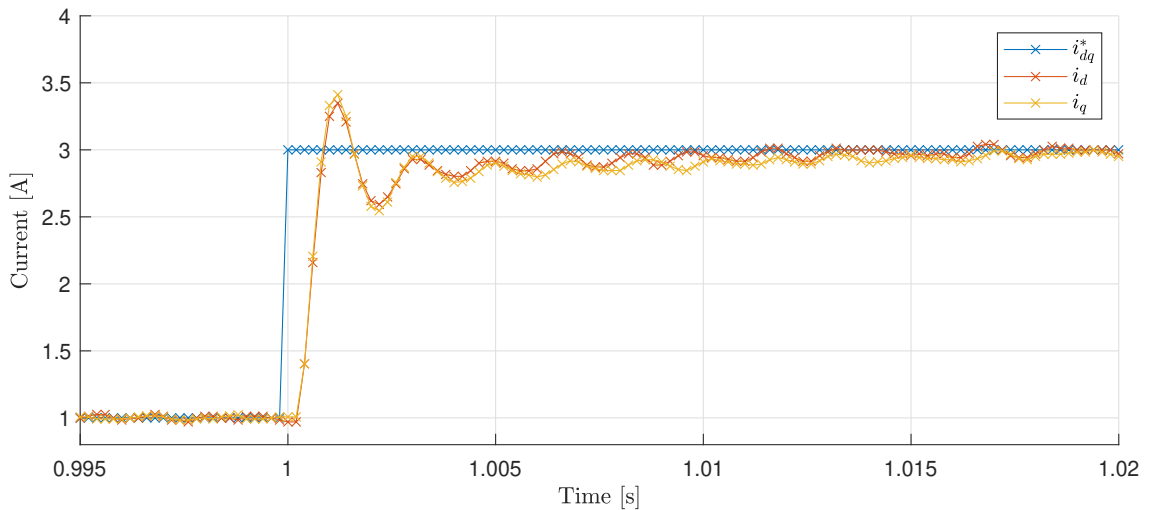
Figure 2.2. Step responses of the dq-currents with the PI controllers in (2.9) and (2.10) from tests using the laboratory setup.

It is seen that the responses of the d- and q-current are similar. The bandwidth of the controllers is designed to be similar, hence equally fast responses are expected. It is seen from the figure, that both current responses have a similar rise- and settling time. The designed controllers are therefore deemed to be acceptable for current control.

With the current controllers deemed acceptable, the PI controller for the speed loop is designed. The zero is placed by utilizing the system's frequency response. Similar to the current controllers, an overshoot in the speed response is deemed acceptable. However, it is desired to reduce the overshoot slightly compared to the current loop. A criterion of phase margin $\phi_m \approx 70°$ is set for the speed loop. The designed PI controller for the speed loop is given in (2.11). Using the designed controller for the speed loop, a bandwidth $\omega_c \approx 24\,\text{rad/s}$ is obtained.

$$G_{c,speed} = k_{i,speed} \cdot \frac{\frac{k_{p,speed}}{k_{i,speed}} \cdot s + 1}{s} = 6 \cdot \frac{0.1 \cdot s + 1}{s} \tag{2.11}$$

The designed speed controller is implemented in the control structure using the laboratory setup and the performance of the speed loop is examined. A test is performed with the PMSM run at 1800 rpm using the encoder as feedback. The PMSM is loaded 2 Nm using the load motor. To examine the speed response, a step load is applied to the system increasing the load from 2 Nm to 6 Nm at time $t = 1\,\text{s}$. Furthermore, at time $t = 4\,\text{s}$ the load is decreased from 6 Nm to 2 Nm. The test is illustrated in figure 2.3.
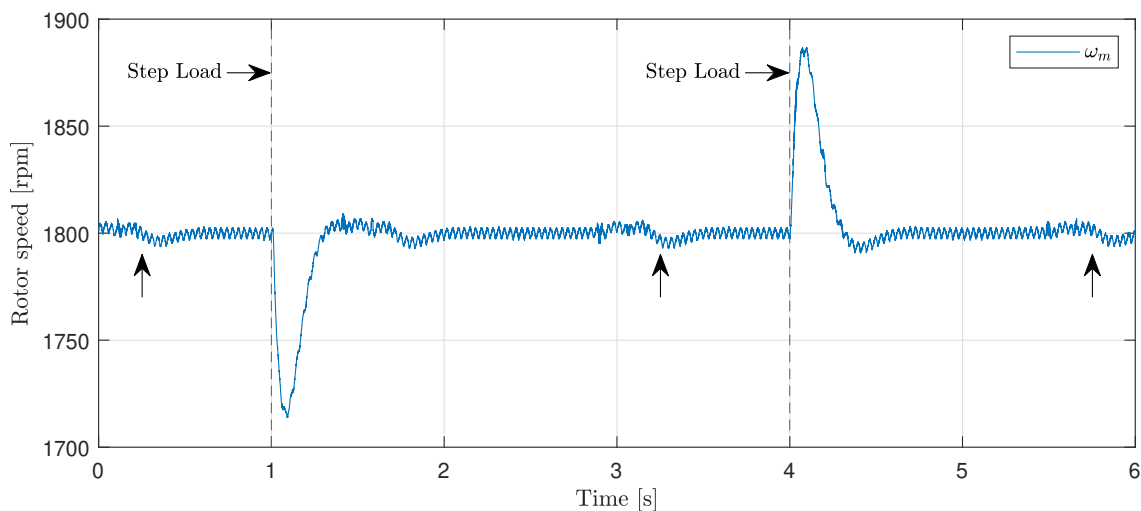
Figure 2.3. Speed response using the encoder as feedback and the PI controller in (2.11). Test is performed using the laboratory setup when a 4 Nm step load is applied.

It is observed that the speed response has some periodic fluctuations, as indicated in the figure with arrows. From previous studies with the laboratory setup, the periodic dynamics, as seen in the figure, are elaborated. In [Christiansen and Clausen, 2022], it is found that the implementation of the control structure does not cause the periodic dynamics. Hence, it may be caused by hardware issues. No further analysis is performed to find the exact cause of the periodic dynamics, and the influence of the dynamics is distinguished.

From the speed response it is seen that when the load is increased to 6 Nm, the rotor speed drops instantaneously. However, the speed converges relatively fast to the reference of 1800 rpm. When the load is decreased to 2 Nm again, the speed increases before it converges to the reference. Based on the speed response illustrated in figure 2.3, the designed PI controller for the speed loop is deemed acceptable.

2.3 Position estimator

To run the PMSM sensorless, the rotor position needs to be estimated to orient the current vector on the q-axis. Ideally, it is desired to orient the current vector precisely on the q-axis. However, as the rotor position is an estimate of the real rotor position, the alignment of the reference frames may not be perfect. Thus, an error between the real and estimated rotor position may occur. The real and estimated reference frame is defined as illustrated in figure 2.4. Where $\tilde{\theta}_e$ is the electrical rotor position error defined as in (2.12).

$$\tilde{\theta}_e = \hat{\theta}_e - \theta_e \tag{2.12}$$
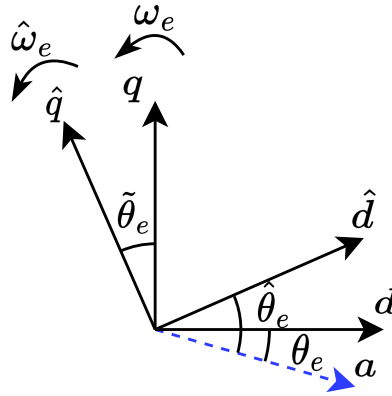
Figure 2.4. Illustration of the reference frames.

To estimate the position, a CLFO with a PLL is designed. The structure of the CLFO is based on the PMSM voltage equation in the $\alpha\beta$ reference frame as given in (2.13) and (2.14).

$$\boldsymbol{u}_{\alpha\beta} = R_s \cdot \boldsymbol{i}_{\alpha\beta} + \dot{\boldsymbol{\lambda}}_{\alpha\beta} \tag{2.13}$$

$$\boldsymbol{\lambda}_{\alpha\beta} = (L_d \cdot i_d + \lambda_{mpm} + j \cdot L_q \cdot i_q) \cdot e^{j\theta_e} \tag{2.14}$$

It is observed from (2.14) that the flux linkage contains information on the rotor position. Hence, the rotor position can be estimated if the flux linkage is known. The flux linkage can be obtained by integration of the voltage command and the resistive voltage as given in (2.15).

$$\boldsymbol{\lambda}_{\alpha\beta} = \int \boldsymbol{u}_{\alpha\beta} - R_s \cdot \boldsymbol{i}_{\alpha\beta} \, dt \tag{2.15}$$

From the parameters listed in table1.1, it is seen that the PMSM has saliency ($L_d \neq L_q$). Thus, a current vector in the $\alpha\beta$ reference frame can not be obtained from (2.14). The dq components are dependent on the rotor position, hence the dq components are eliminated by manipulation of the flux linkage equation (2.14) as given in (2.16).

$$\boldsymbol{\lambda}_{\alpha\beta} = (L_d \cdot i_d + \lambda_{mpm} \underbrace{-L_q \cdot i_d + L_q \cdot i_d}_{Added\ zero\ term} + jL_q \cdot i_q) \cdot e^{j\theta_e}$$

$$= \left((L_d - L_q) \cdot i_d + \lambda_{mpm} + L_q \cdot \boldsymbol{i}_{dq} \right) \cdot e^{j\theta_e}$$

$$= L_q \cdot \boldsymbol{i}_{\alpha\beta} + \left(\underbrace{(L_d - L_q) \cdot i_d + \lambda_{mpm}}_{\lambda_{\alpha\beta,af}} \right) \cdot e^{j\theta_e} \tag{2.16}$$

The term $(L_d - L_q) \cdot i_d + \lambda_{mpm}$ is known as active flux [Boldea et al., 2008]. For the remainder of this thesis, the active flux is referred to as $\lambda_{\alpha\beta,af}$. The rotor position can be estimated as (2.19).

$$\boldsymbol{\lambda}_{\alpha\beta} - L_q \cdot \boldsymbol{i}_{\alpha\beta} = \left((L_d - L_q) \cdot i_d + \lambda_{mpm} \right) \cdot e^{j\theta_e} \tag{2.17}$$

$$\angle(\boldsymbol{\lambda}_{\alpha\beta} - L_q \cdot \boldsymbol{i}_{\alpha\beta}) = \angle e^{j\theta_e} \tag{2.18}$$

$$\bar{\theta}_e = tan^{-1}\left(\frac{\lambda_\beta - L_q \cdot i_\beta}{\lambda_\alpha - L_q \cdot i_\alpha} \right), \quad \begin{cases} \lambda_\alpha = \int (u_\alpha - R_s \cdot i_\alpha)\ dt \\ \lambda_\beta = \int (u_\beta - R_s \cdot i_\beta)\ dt \end{cases} \tag{2.19}$$

From (2.19) it is seen that an estimate of the rotor position is obtained using the flux linkage $\lambda_{\alpha\beta}$.

2.3.1   Closed Loop Flux Observer

The flux linkage $\lambda_{\alpha\beta}$ can be estimated utilizing a CLFO that compares the flux linkage based on the measured current and the voltage command. The principle of the CLFO is illustrated by the block diagram in figure 2.5.
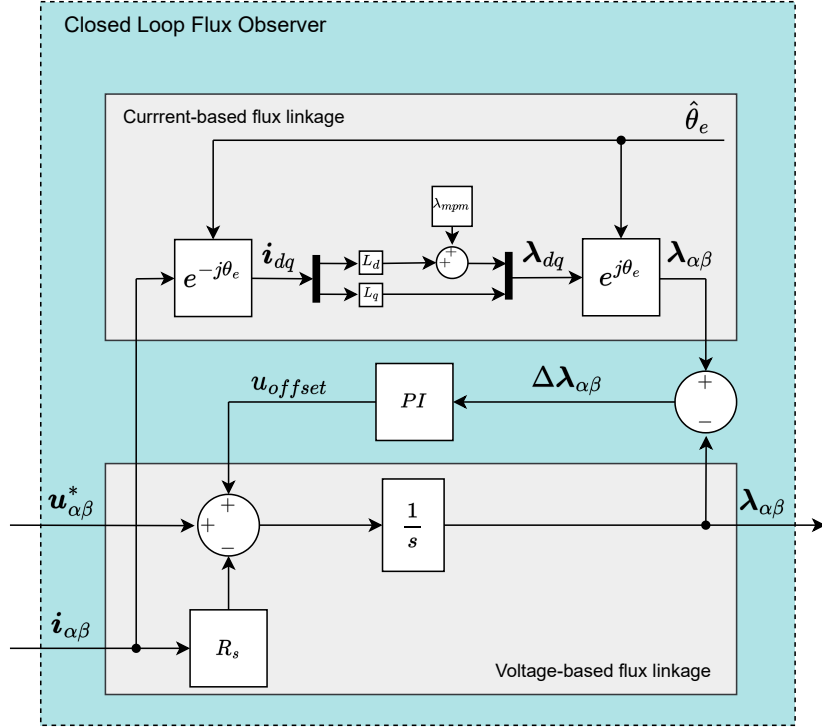
Figure 2.5. Block diagram of the CLFO.

In the voltage-based flux linkage, DC-drift may occur due to the integration. The advantage of the CLFO is that it suppresses the DC-drift by comparing it to the current-based flux linkage. The current-based flux linkage is obtained without an integrator, hence it is not affected by the drift and can be used as a reference. The error between the current-based and the voltage-based flux linkage is then assumed to be caused by the DC-drift and is fed through a PI controller to compensate for the offset.

The PI parameters in the CLFO are designed based on previous experiences in the laboratory [Christiansen and Clausen, 2022]. The bandwidth of the CLFO PI is desired to be approximate $10\,\%$ of the rated speed. This implies that the current-based flux linkage is dominant at low speed range, and the voltage-based flux linkage is dominating at mid-high speed range. The parameters are determined to $k_p = 50$ and $k_i = 100$.

2.3.2   Phase-locked Loop

The estimated position in (2.19) can be noisy due to the arctan function, which is undesirable. To avoid this, a PLL is implemented to suppress high-frequency noise. A block diagram of the CLFO-PLL position estimator is illustrated in figure 2.6.
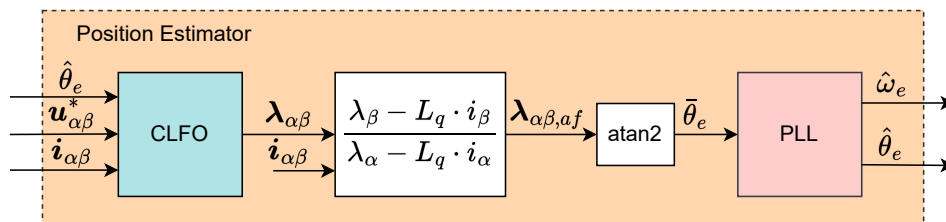
Figure 2.6. Block diagram of the position estimator.

The rotor position $\bar{\theta}_e$ obtained from the active flux $\lambda_{\alpha\beta,af}$ is fed through the PLL. The PLL functions as a low-pass filter, such high-frequency noise in the estimate position obtained from (2.19) are suppressed, and a more smooth position estimation is obtained [Wang et al., 2017]. Furthermore, an estimation of the rotor speed is obtained from the PLL. The structure of the PLL is illustrated in figure 2.7.
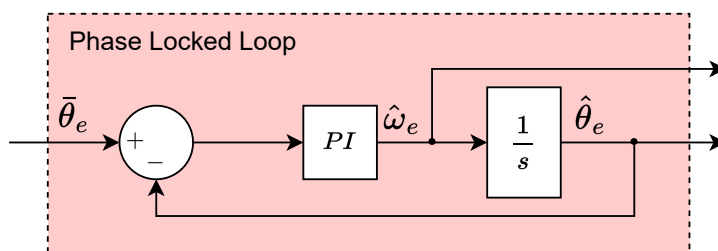
Figure 2.7. Block diagram of the PLL.

The PLL PI parameters are designed theoretically based on its bandwidth ω_c. To ease the calculation of the PLL parameters, a linear relationship between the natural frequency ω_n and a desired bandwidth ω_c is established. The transfer function of a PLL system is given in (2.20).

$$G_{PLL}(s) = \frac{\text{Output}}{\text{Input}} = \frac{s \cdot k_p + k_i}{s^2 + s \cdot k_p + k_i} \tag{2.20}$$

From (2.20) it is seen that the PLL system is a second order system. By introducing the structure of a second order system in (2.21) the PLL parameters can be defined as in (2.22).

$$G(s) = \frac{s \cdot 2 \cdot \zeta \cdot \omega_n + \omega_n^2}{s^2 + s \cdot 2 \cdot \zeta \cdot \omega_n + \omega_n^2} \tag{2.21}$$

$$k_p = 2 \cdot \zeta \cdot \omega_n, \quad k_i = w_n^2 \tag{2.22}$$

Where ζ is the damping ratio and ω_n is the natural frequency. Setting the damping ratio to $\zeta = 1$ the parameters in the PLL can be designed as in (2.23).

$$k_p = 2 \cdot \omega_n, \quad k_i = w_n^2 \tag{2.23}$$

Utilizing (2.23), a linear relationship between the natural frequency ω_n and the bandwidth ω_c is established from the bode diagram of the PLL system illustrated in figure 2.8.
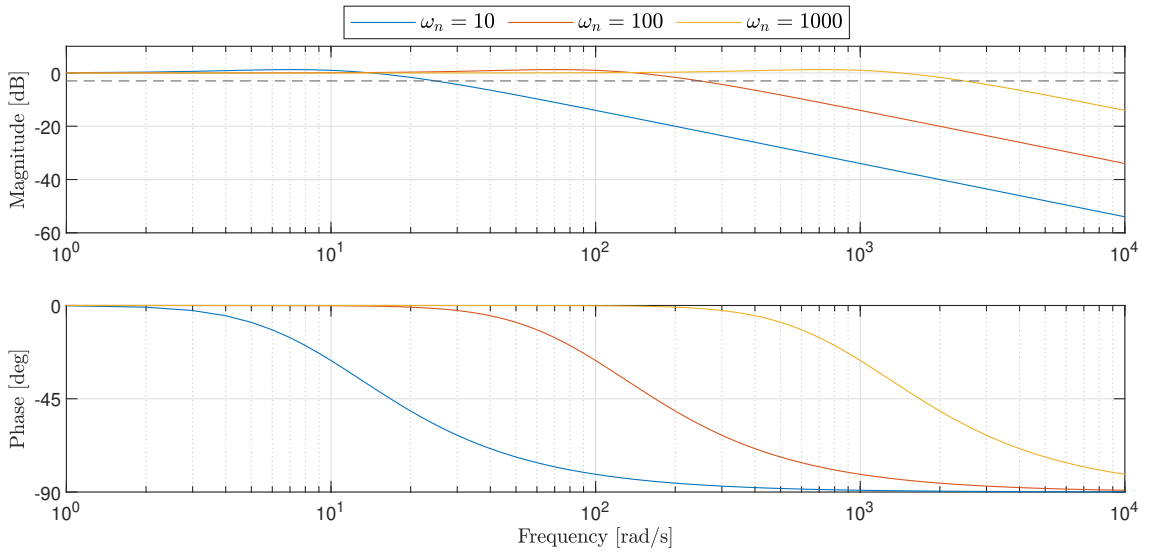

Figure 2.8. Bode diagram of the PLL system.

From the bode diagram, the bandwidth is allocated at $-3\,\text{dB}$. Based on this, a linear relationship between the natural frequency ω_n and the bandwidth ω_c is established such that $\omega_c = 2.48 \cdot \omega_n$.

The bandwidth of the PLL system is desired to be high to ensure fast dynamics in the position estimation to avoid phase shift in the transient operation. However, the speed noise can be significant due to high PI gains. Hence the bandwidth is chosen to be designed as $\omega_c = 500\,\text{rad/s}$, which corresponds to parameters $k_p = 403$ and $k_i = 40648$ according to (2.23).

2.3.3 Validation

The designed CLFO-PLL position estimator is implemented in the control system and tested in the laboratory setup to examine the performance. A test is performed with the PMSM run at 1800 rpm with 2 Nm load applied using the CLFO-PLL position estimator as feedback for the position and speed. The encoder is only used for comparison of the position and speed. A step load is applied to the system increasing the load from 2 Nm to 6 Nm at time $t = 1\,\text{s}$. Furthermore, at time $t = 4\,\text{s}$ the load is decreased from 6 Nm to 2 Nm. The test is illustrated in figure 2.9.
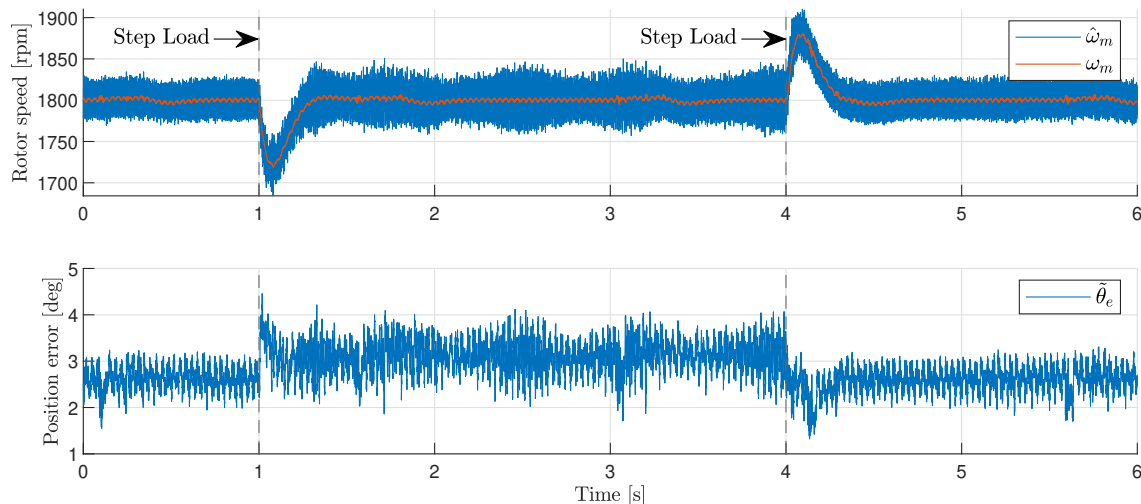
Figure 2.9. Speed response and position error with implemented CLFO-PLL position estimator.

It is seen that the estimated speed $\hat{\omega}_m$ and the real speed ω_m have similar responses. However, the estimated speed is significantly more noisy. When examining the position error it is seen that the estimated position $\hat{\theta}_e$ is leading the real position θ_e based on the definition of the position error in (2.12). The estimated position leads more as the load is increased to 6 Nm. At the time when the load is increased it is seen that the position error peaks. This implies that the position estimation is not fast enough to detect the real position in the transient period. The same tendency is seen when the load is decreased to 2 Nm again.

This thesis aims to examine the possibility of using adaptive filters to suppress harmonic distortion in the estimated position, caused by inverter nonlinearities and spatial flux harmonics. As described in section 1.1 the filters are evaluated based on their harmonic suppression capability and dynamic performance. Thus, minor offset and phase shift are acceptable as long as the filters' performance is compared to the performance of the designed position estimator. Hence, the position estimator is deemed to be sufficient for further use.

Harmonic analysis 3

In this chapter, the effects of the inverter nonlinearities and flux spatial harmonics in the estimated back-EMF and the estimated position are analyzed. Firstly, the estimated back-EMF and the position error are analyzed theoretically. Secondly, measured currents, estimated active flux, and position error are analyzed based on an experimental test performed with the laboratory setup. The obtained signals from the test are analyzed using Fast Fourier Transform (FFT) analysis to examine the frequency components of the respective signals. Lastly, the effects of current measurement errors are analyzed both theoretically and verified with measurements from experimental tests.

3.1 Effects of harmonic distortion

As described in chapter 1, the inverter nonlinearities and flux spatial harmonics cause harmonics distortion, which will introduce $(6h \pm 1)$th order harmonic components in the estimated back-EMF, where $h = 1, 2, 3...$ The flux linkage is related to the back-EMF as expressed in (3.1), hence it is expected that the $(6h \pm 1)$th order harmonic components will be introduced in the active flux used for position estimation. Figure 3.1 illustrates the relation between the flux and the back-EMF of the PMSM.

$$\boldsymbol{e}_{\alpha\beta} = \frac{d\boldsymbol{\lambda}_{\alpha\beta}}{dt} \tag{3.1}$$
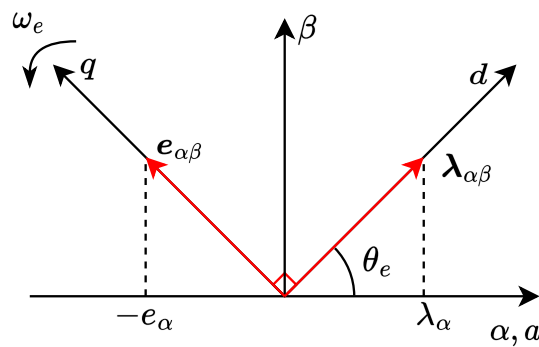
Figure 3.1. Illustration of flux and back-EMF relationship.

Using the relation seen in figure 3.1, the flux linkage of the PMSM expressed in the $\alpha\beta$ reference frame is given in (3.2).

$$\lambda_\alpha = \lambda_{\alpha\beta} \cdot \cos(\theta_e)$$
$$\lambda_\beta = \lambda_{\alpha\beta} \cdot \sin(\theta_e) \tag{3.2}$$

To analyze the effect of the $(6h \pm 1)$th order harmonic components in the estimated flux linkage, the estimated flux linkage is written including a fundamental and a harmonic term as in (3.3).

$$
\hat{\lambda}_\alpha = \lambda_{f\alpha} + \lambda_{h\alpha}
$$
$$
\hat{\lambda}_\beta = \lambda_{f\beta} + \lambda_{h\beta} \tag{3.3}
$$

Where λ_f and λ_h are denoted as the fundamental and the harmonic component in the estimated flux linkage, respectively. The estimated flux linkage is expanded to (3.4). For simplicity, the notation $(\pm(6h \pm 1) \cdot \omega_e \cdot t)$ is used as composition of $-(5h) \cdot \omega_e \cdot t$ and $(7h) \cdot \omega_e \cdot t$.

$$
\hat{\lambda}_\alpha = \underbrace{\lambda_1 \cdot \cos(\omega_e \cdot t)}_{\lambda_{f\alpha}} + \underbrace{\sum_{h=1}^{n} \lambda_{6h\pm1} \cdot \cos\big(\pm (6h \pm 1) \cdot \omega_e \cdot t \big)}_{\lambda_{h\beta}}
$$
$$
\hat{\lambda}_\beta = \underbrace{\lambda_1 \cdot \sin(\omega_e \cdot t)}_{\lambda_{f\beta}} + \underbrace{\sum_{h=1}^{n} \lambda_{6h\pm1} \cdot \sin\big(\pm (6h \pm 1) \cdot \omega_e \cdot t \big)}_{\lambda_{h\beta}} \tag{3.4}
$$

Where λ_1, and $\lambda_{6h\pm1}$ are the magnitude of the fundamental and the $(6h \pm 1)$th order harmonic components, respectively.

Adopting the principle of a quadrature PLL, the rotor position error is analyzed to examine the effects of the harmonic distortion in the estimated flux linkage to the estimated position. The position error obtained from a quadrature PLL is given in (3.5). Combining (3.5) with $\hat{\theta}_e = \hat{\omega}_e \cdot t$ the rotor position error is given as in (3.6).

$$
\tilde{\theta}_e \approx \sin(\tilde{\theta}_e) = -\hat{\lambda}_\alpha \cdot \sin(\hat{\theta}_e) + \hat{\lambda}_\beta \cdot \cos(\hat{\theta}_e) \tag{3.5}
$$

$$
\tilde{\theta}_e = \lambda_1 \cdot \sin\big((\omega_e - \hat{\omega}_e) \cdot t\big) + \sum_{h=1}^{n} \lambda_{6h\pm1} \cdot \sin\big(\pm (6h \pm 1) \cdot \omega_e - \hat{\omega}_e) \cdot t \big) \tag{3.6}
$$

Using the approximation of $\omega_e \approx \hat{\omega}_e$, the rotor position error becomes (3.7).

$$
\tilde{\theta}_e = \lambda_1 \cdot \sin\big((\omega_e - \hat{\omega}_e) \cdot t\big) + \sum_{h=1}^{n} \lambda_{6h-1} \cdot \sin\big(- (6h) \cdot \hat{\omega}_e) \cdot t \big)
$$
$$
+ \sum_{h=1}^{n} \lambda_{6h+1} \cdot \sin\big((6h) \cdot \hat{\omega}_e) \cdot t\big) \tag{3.7}
$$

From (3.7) it is observed that the $(6h \pm 1)$th order harmonic components of the estimated flux linkage affect the rotor position error. It is seen that the $(6h)$th order harmonic component is introduced to the rotor position error, hence the estimated position will likewise contain $(6h)$th order harmonic fluctuations.

3.2   Harmonic distortion in measurements

In this section, measured and estimated signals are analyzed based on tests performed with the laboratory setup introduced in section 1.2 to examine the harmonic distortion in the signals. The frequency spectrum of the signals is examined utilizing FFT analysis to clarify whether the expected harmonic distortion is present. The PMSM is run with the sensorless FOC designed in chapter 2 during the tests. The PMSM is run at 1800 rpm with 2 Nm load applied using the load motor.

Figure 3.2 illustrates the measured current represented in the $\alpha\beta$ reference frame. The sequence illustrated is arbitrarily chosen from the data obtained from the laboratory test. Furthermore, the frequency spectrum of the current is illustrated as well.
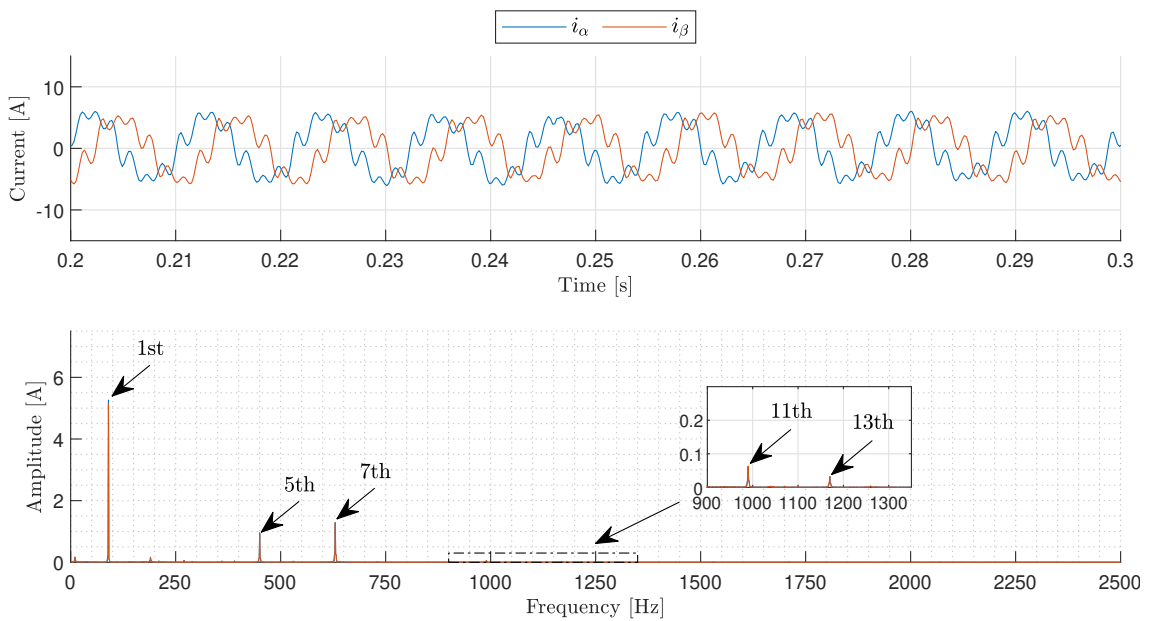
Figure 3.2. Measured current in the $\alpha\beta$ reference frame along with the frequency spectrum obtained by FFT analysis. The PMSM is run at 1800 rpm with 2 Nm load.

From the measured $\alpha\beta$ current waveforms it is seen that the current is heavily distorted, as the measured current deviate from a pure sinusoidal signal. The frequency spectrum shows that the current contains obvious $(6h \pm 1)$th order harmonics. As expected, the current signals are mainly distorted by the (6 ± 1)th order harmonic components. However, the signal also contains the (12 ± 1)th order harmonic components. The high-order harmonics have low amplitude, meaning they have a small impact on the signal and are neglected further.

The analysis in section 3.1 shows how $(6h \pm 1)$th order harmonics are present in the estimated flux linkage. For position estimation, the concept of active flux is utilized. It is expected to see the same $(6h \pm 1)$th order harmonics in the estimation of the active flux. Figure 3.3 illustrates the estimated active flux represented in the $\alpha\beta$ reference frame obtained from the CLFO. Furthermore, the frequency spectrum is illustrated as well.
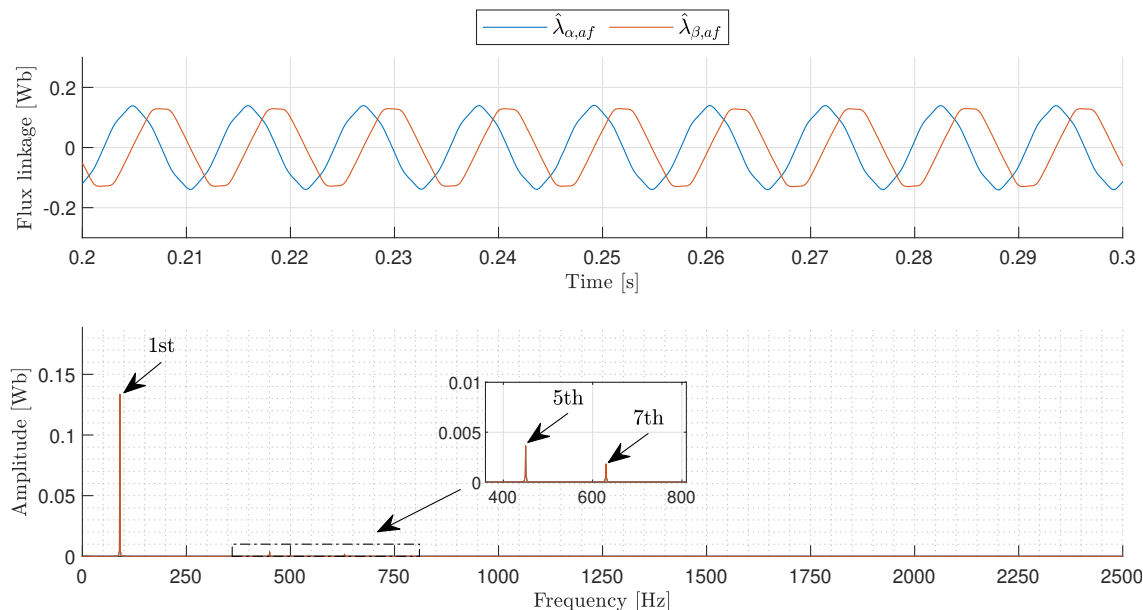
Figure 3.3. Estimated active flux in the $\alpha\beta$ reference frame along with the frequency spectrum obtained by FFT analysis. The PMSM is run at 1800 rpm with 2 Nm load.

As the measured currents are distorted by the $(6h \pm 1)$th order harmonic components it is expected that the estimated active flux is distorted by these harmonics as well. From the estimated active flux waveform it is observed that the signal does not appear heavily distorted, as is the case with the measured current in figure 3.2. However, the estimated active flux is distorted to some extent. This is also seen from the frequency spectrum, as (6 ± 1)th order harmonic components are seen. The influence of the (12 ± 1)th order harmonic components and higher are neglected, as the amplitude of the harmonics does not impact the distortion significantly. Thus, only the (6 ± 1)th order harmonic components will be considered in the estimated active flux for the remainder of this thesis.

Figure 3.4 illustrates the position error between the sensorless position estimator and the encoder. The position error is defined as in (2.12), where the real rotor position θ_e is obtained using the encoder. The position error contains an offset and some fluctuation hence, the frequency spectrum is performed for the fluctuating part of the position error for better possibilities to examine the harmonic components in the fluctuating part. The frequency spectrum of the fluctuation in the position error is illustrated in the figure as well. The fluctuation in the position error is expected to be dominated by a $(6h)$th harmonic component based on the analysis described in section 3.1.
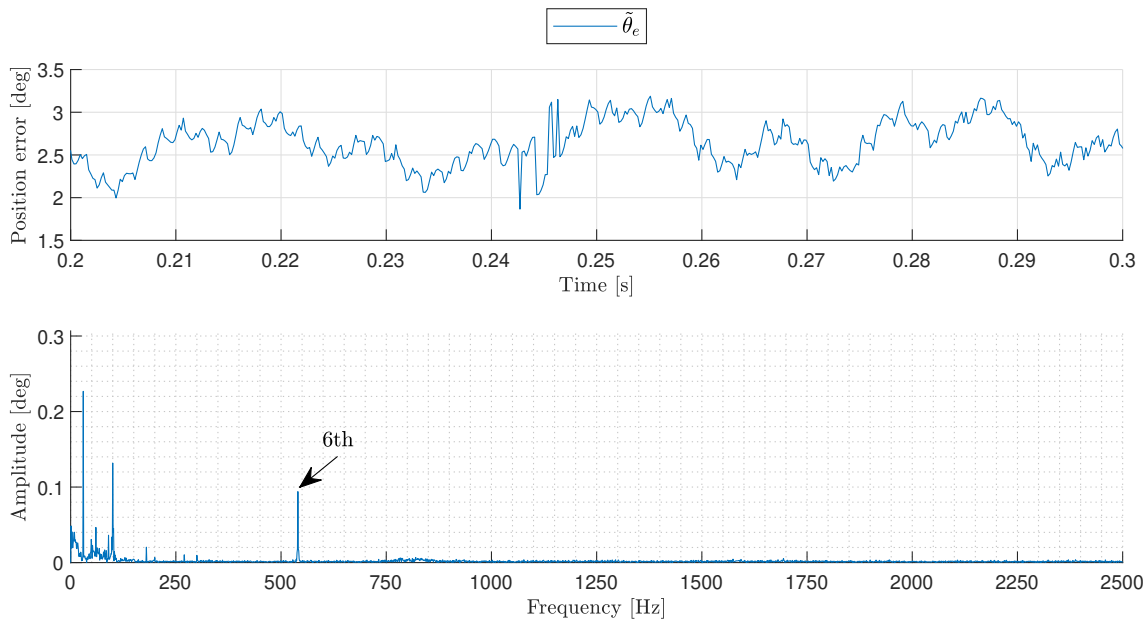
Figure 3.4. Position error along with the frequency spectrum obtained by FFT analysis. The PMSM is run at 1800 rpm with 2 Nm load.

It is seen that the position error has an offset, and some fluctuation around the offset value occurs. It is observed from the illustration of the position error that the fluctuation contains multiple frequencies, hence other frequency components than the $(6h)$th harmonic component are introduced to the position error. This is supported by the frequency spectrum of the position error fluctuation. It is seen that the fluctuation contains a dominant 6th order harmonic component. However, the position error also includes some low frequency fluctuations. As this deviates from the expectations of the cause of fluctuation in the position error, the introduced lower frequency components are examined in the following section.

3.3 Examination of frequency components

As seen in figure 3.4 the position error contains lower frequency components and is not only dominated by the $(6h)$th order harmonic component as expected. Thus, the cause of the low frequency components in the position error is examined in this section.

The position error and frequency spectrum are affected by the estimated position signal and the position obtained from the encoder. Hence, it is desired to examine the estimation and the encoder signal individually to analyze the cause of the low frequency components in the position error.

To analyze the frequency spectrum of the signals obtained from the encoder and the estimator, the speed measurement is used. The speed measurement is used, as this allows to analyze the variation of the estimation and encoder signal individually. Figure 3.5 shows the frequency spectrum of the variation in the estimated speed and the encoder speed for a laboratory test when the PMSM is run with sensorless FOC at 1800 rpm with 2 Nm load.
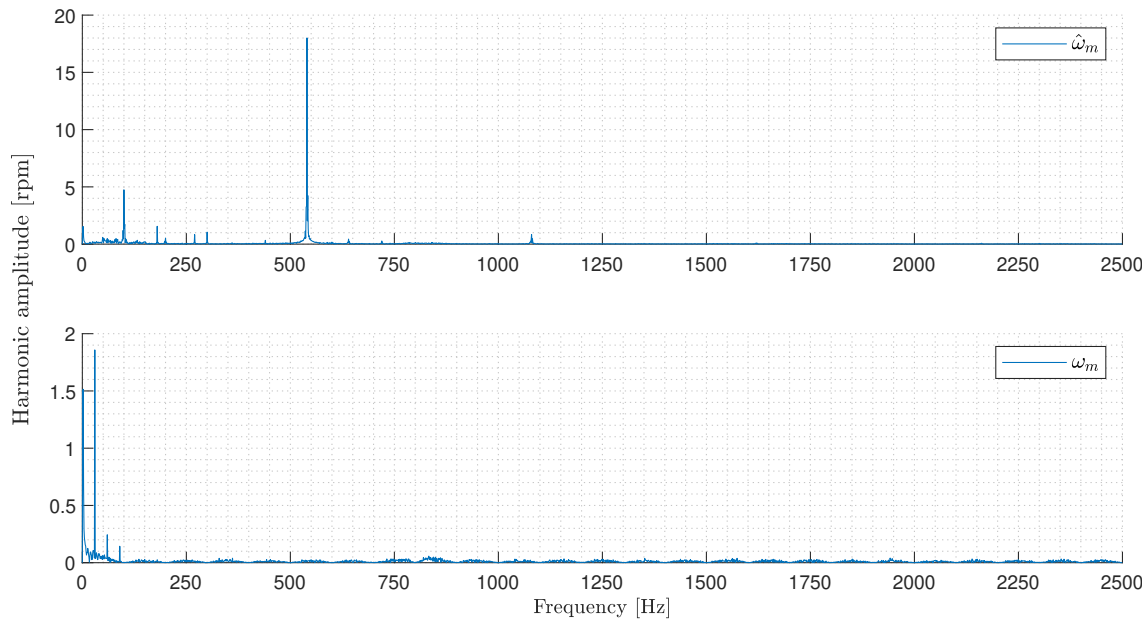
Figure 3.5. Frequency spectrum obtained by FFT analysis of the estimated speed and encoder speed. The PMSM is run sensorless at 1800 rpm with 2 Nm load.

It is seen that the fluctuation in the estimated speed $\hat{\omega}_m$ is dominated by the corresponding 6th order harmonic component. However, the estimated speed fluctuation also contains low frequency components. It is observed that frequencies corresponding to the fundamental (1st), 2nd, and 3rd order harmonic components are present in the estimated speed. From the frequency spectrum of the speed obtained from the encoder ω_m, it is seen that the speed fluctuation has one dominating frequency component along with some noise contribution. It is observed that the dominating frequency of the fluctuation in the encoder speed corresponds to the mechanical frequency of the rotor. As this frequency is only dominant in the encoder speed, it is expected to be caused by the encoder or some mechanical connection with the physical setup. Hence, it is expected that the frequency component corresponding to the mechanical frequency will be present in the estimated speed if the encoder is used as feedback in the control loop. Thus, a test is performed with the encoder used for position and speed feedback with the PMSM run at 1800 rpm and 2 Nm load, to examine whether the encoder signal introduces a frequency component corresponding to the mechanical frequency in the estimated speed. The frequency spectrum of the estimated speed and the encoder speed obtained from the test is illustrated in figure 3.6.
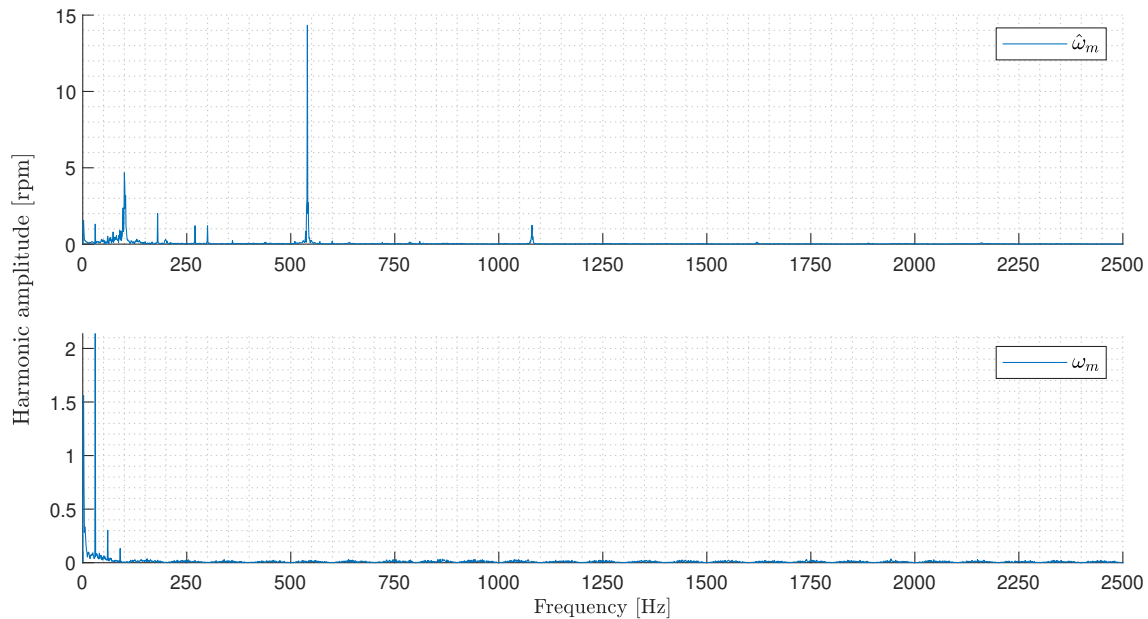
Figure 3.6. Frequency spectrum obtained by FFT analysis of the estimated speed and encoder speed. The PMSM is run with encoder feedback at 1800 rpm with 2 Nm load.

It is seen that when the PMSM is run with encoder feedback, the component corresponding to the mechanical frequency of the rotor is introduced in the frequency spectrum of the estimated speed. Based on the two tests with sensorless control and control with encoder feedback, it is assessed that the introduction of the frequency component corresponding to the mechanical frequency is caused by mechanical issues with the setup. This is assessed based on the mechanical frequency component present in the encoder signal and is only introduced in the estimated speed when the encoder is used as feedback.

It is expected that the same tendencies of present frequencies in the speed are seen in the rotor position. Comparing the frequency spectrum for the estimated speed and the encoder speed with the position error in figure 3.4 it is seen that the position error contains the same frequencies as seen in the speed. The position error will contain the frequencies of both the estimated position and the encoder position due to the definition in (2.12). Thus, the mechanical frequency component is present in the position error due to the encoder relation.

From figure 3.5 and 3.6 it is further observed that frequency components corresponding to the fundamental, 2nd and 3rd order harmonic components are present in the estimated speed. According to Zhang et al. [2021] and Zhang et al. [2022] current measurement errors may introduce multiple frequency components including 1st and 2nd order harmonic components. Current measurement errors may occur due to scaling and offset errors with the current sensors. The effects of current measurement errors are elaborated in the following sections:

Offset error

The offset error is mainly caused by zero drift, residual current of the current sensor, and operational amplifier deviation [Zhang et al., 2021]. The offset error is considered using the expression in (3.8).

$$
\begin{aligned}
i_{a,meas} &= I_m \cdot \cos(\omega_e \cdot t) + \Delta I_{a,offset} \\
i_{b,meas} &= I_m \cdot \cos(\omega_e \cdot t - \frac{2 \cdot \pi}{3}) + \Delta I_{b,offset} \\
i_{c,meas} &= I_m \cdot \cos(\omega_e \cdot t + \frac{2 \cdot \pi}{3}) + \Delta I_{c,offset}
\end{aligned}
\tag{3.8}
$$

Where $i_{a,meas}$, $i_{b,meas}$, and $i_{c,meas}$ are the measured currents used in the control structure. I_m is the amplitude of the sinusoidal three-phase currents, and $I_{a,offset}$, $I_{b,offset}$, and $I_{c,offset}$ are a DC component of the phase currents, respectively. Utilizing reference frame transformation to represent the abc currents in the rotating dq-reference frame with the current vector oriented on the q-axis, the dq currents are expressed as in (3.9).

$$
\begin{aligned}
i_{d,offset} &= \frac{2}{3} \cdot \big(\Delta I_{a,offset} \cdot \cos(\omega_e \cdot t) + \Delta I_{b,offset} \cdot \cos(\omega_e \cdot t) \\
&\quad + \Delta I_{c,offset} \cdot \cos(\omega_e \cdot t) \big) \\
i_{q,offset} &= I_m - \frac{2}{3} \cdot \big(\Delta I_{a,offset} \cdot \sin(\omega_e \cdot t) + \Delta I_{b,offset} \cdot \sin(\omega_e \cdot t) \\
&\quad + \Delta I_{c,offset} \cdot \sin(\omega_e \cdot t) \big)
\end{aligned}
\tag{3.9}
$$

When transformed to the dq-reference frame, the AC component of the abc currents will appear as a DC component with amplitude corresponding to I_m in the q-axis current. The offset current introduce an AC component to both the d- and q-axis current with a frequency corresponding to the fundamental frequency ω_e. The oscillating dq current results in torque ripple, which leads to ripples in the rotor speed with the same frequency as the oscillating dq currents. Hence, the offset error in the current measurement will introduce a frequency component corresponding to the fundamental frequency of the electrical rotor speed and thereby also the rotor position.

Scaling error

The output current from the current sensors is adjusted to match the input range of the analog-to-digital converter, which causes a scaling error in the measured currents [Zhang et al., 2021]. Considering only the scaling error, the measured current is expressed as (3.10).

$$
\begin{aligned}
i_{a,meas} &= k_a \cdot I_m \cdot \cos(\omega_e \cdot t) \\
i_{b,meas} &= k_b \cdot I_m \cdot \cos(\omega_e \cdot t - \frac{2 \cdot \pi}{3}) \\
i_{c,meas} &= k_c \cdot I_m \cdot \cos(\omega_e \cdot t + \frac{2 \cdot \pi}{3})
\end{aligned}
\tag{3.10}
$$

Where k_a, k_b, and k_c are scaling gains for the three-phase currents, respectively. Typically the scaling gain of each phase current is different from each other due to the difference

between the sampling and the adjusting circuits. Due to the scaling error, the three-phase current measurements are asymmetrical.

Applying the symmetrical component method, the asymmetrical three-phase currents in (3.10) are decomposed into positive, negative, and zero sequence components. The decomposed three-phase currents are expressed in (3.11).

$$\boldsymbol{i}_{abc,meas} = \boldsymbol{i}_p \cdot e^{j \cdot \omega_e \cdot t} + \boldsymbol{i}_n \cdot e^{-j \cdot \omega_e \cdot t} + \boldsymbol{i}_z \tag{3.11}$$

Where $\boldsymbol{i}_p$, $\boldsymbol{i}_n$, and $\boldsymbol{i}_z$ are the positive, negative, and zero sequence components, respectively. Utilizing reference frame transformation to express the three-phase currents in the rotating dq-reference frame with the current vector oriented on the q-axis, the dq currents are expressed as in (3.12).

$$i_{d,scaling} = -I_n \cdot sin(2 \cdot \omega_e \cdot t)$$
$$i_{q,scaling} = I_p - I_n \cdot cos(2 \cdot \omega_e \cdot t) \tag{3.12}$$

The positive sequence component will appear as a DC component in the q-axis current. The negative sequence component, when transformed to the dq-reference frame, will introduce an AC component to the dq currents which oscillate with twice the fundamental frequency. Hence the scaling error will introduce a frequency component twice the fundamental of the electrical rotor speed and position.

It is seen that the current measurement error including scaling and offset effects, that frequency components corresponding to the fundamental and twice the fundamental frequency are introduced in the dq currents. The oscillating currents affect the torque and rotor speed, which will have ripples corresponding to the same frequency components. Figure 3.7 illustrates the dq currents and frequency spectrum when the PMSM is run with sensorless control at 1800 rpm and applying 2 Nm load to the system.
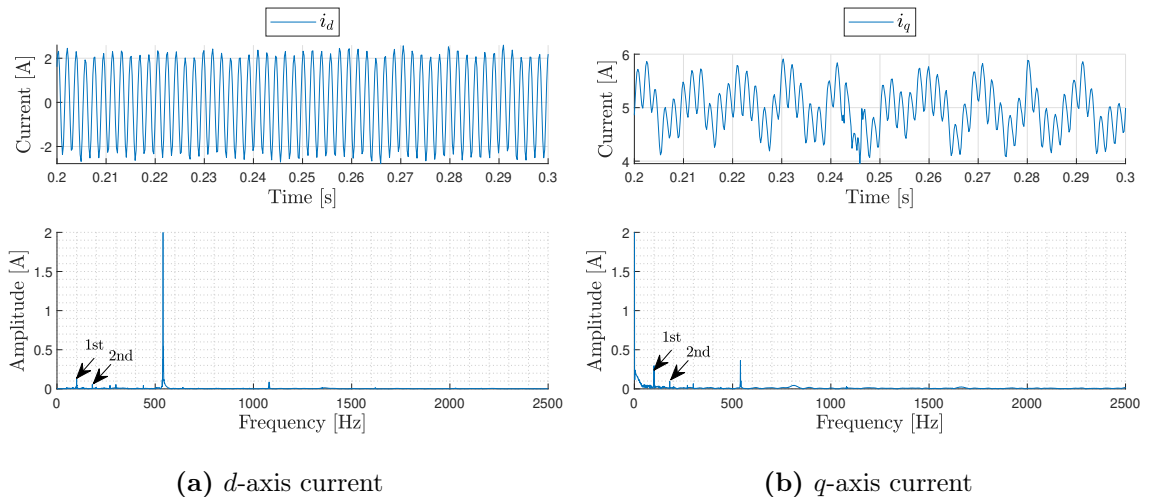

(a) d-axis current   **(b)** q-axis current

Figure 3.7. Waveform and amplitudes in the frequency spectrum of the dq currents. The data is obtained running the PMSM with sensorless control at 1800 rpm with 2 Nm load applied to the system.

It is seen that the d-axis current oscillates around zero amplitude, while the q-axis current oscillates around a DC value of approximately 5 A. In the frequency spectrum of both the

dq currents, components of the 1st and 2nd order harmonics are present. However, it is further seen that the oscillation of the *dq* currents is mainly caused by the nonlinearities of the inverter, as the dominating frequency component corresponds to the 6th order harmonic component.

Based on the analysis of the effects of current measurement error, including scaling error and offset error, the frequency components related to the 1st and 2nd order harmonic components seen in the estimated rotor speed in figure 3.5 and 3.6 and in the position error in figure 3.4 are expected to be caused by current measurement errors.
The objective of this thesis is to suppress the dominating 6th order harmonic component in the estimated position caused by nonlinearities in the inverter and flux spatial harmonics. It is seen from the test illustrated in figures 3.4, 3.5, and 3.6 that the 6th order harmonic component is still more dominant. Thus, no further action is made to reduce or remove the influence of current measurement errors.

Complex-coefficient Synchronous Frequency Filter 4

In this chapter, the complex-coefficient synchronous frequency filter (CCSFF) from Wu et al. [2022] is presented to filter out the (6 ± 1)th order harmonic component in the estimated flux to suppress the 6th order component in the estimated position and speed. Firstly the structure of the CCSFF is presented along with its filtering capability at the synchronous frequency. Furthermore, the CCSFF combined with the PLL is Laplace transformed and a transfer function is established to set up design guidelines for parameters. Secondly, the harmonic suppression capability along with the effects of the filter parameter design is examined experimentally using the laboratory setup. Lastly, is the dynamic performance examined of the control system with the CCSFF. The performance of the CCSFF is compared to when no filtering is performed. In addition to this, an adaptive approach to the parameter design is proposed to improve the dynamic performance when using the CCSFF.

4.1 Filter structure

The presented CCSFF is a complex bandpass filter with unity gain and zero-phase shift at the synchronous frequency $\hat{\omega}_e$. According to Wu et al. [2022], the filter possesses an adaptive-frequency bandpass-filtering characteristic, removing the harmonics in the estimated flux and reducing the oscillating error in the estimated position. The filter is implemented such that the estimated active flux $\lambda_{\alpha\beta,af}$ is filtered through the CCSFF before it is used in the PLL as illustrated in figure 4.1 with $z_{\alpha\beta} = \lambda_{\alpha\beta,af}$
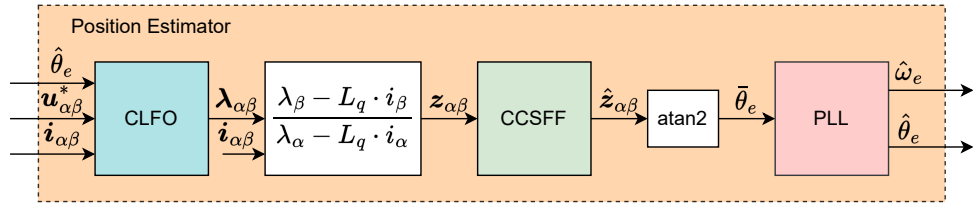
Figure 4.1. Block diagram of the CLFO-CCSFF-PLL-based position estimation system.

The inputs to the CCSFF are defined as in (4.1).

$$z_\alpha \approx Z \cdot \cos(\omega_e \cdot t) + Z_{6\pm 1} \cdot \cos(\pm(6 \pm 1) \cdot \omega_e \cdot t)$$
$$z_\beta \approx Z \cdot \sin(\omega_e \cdot t) + Z_{6\pm 1} \cdot \sin(\pm(6 \pm 1) \cdot \omega_e \cdot t) \tag{4.1}$$

Figure 4.2 illustrates the working principle of the CCSFF system.

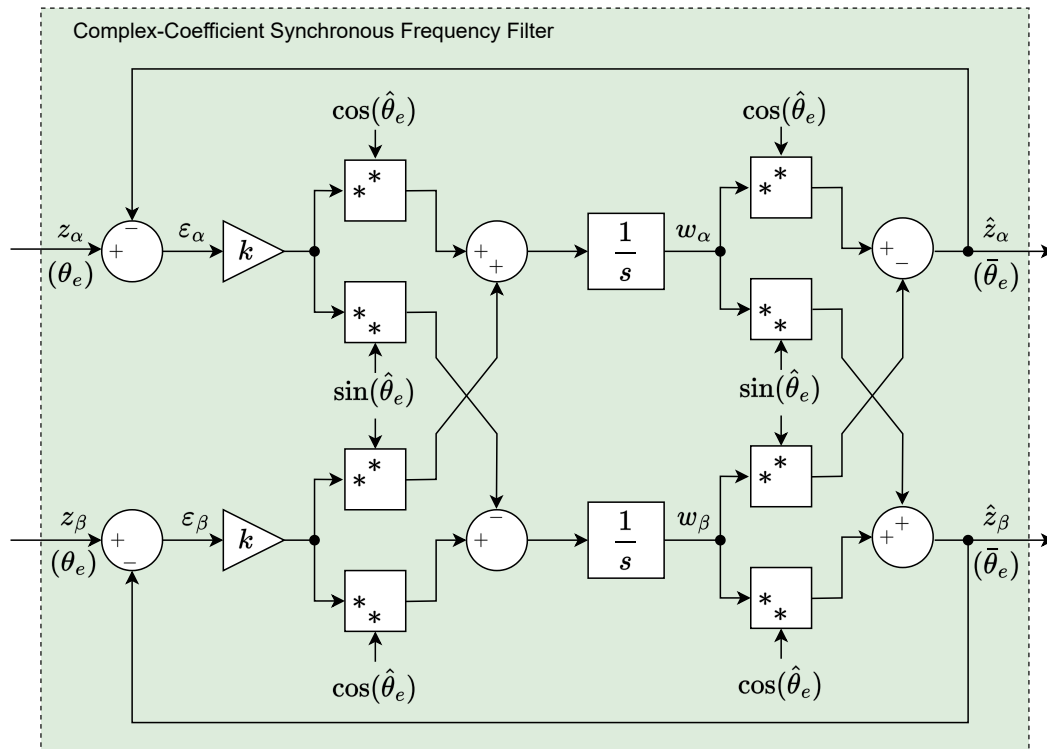**Figure 4.2.** Block diagram of the CCSFF system [Wu et al., 2022].

Where $\boldsymbol{z}_{\alpha\beta}$ is the active flux containing harmonic distortion, $\hat{\boldsymbol{z}}_{\alpha\beta}$ is the filtered flux which ideally only contains the fundamental frequency, $\boldsymbol{\varepsilon}_{\alpha\beta}$ is the error signal between the estimated flux $\boldsymbol{z}_{\alpha\beta}$ and the filtered flux $\hat{\boldsymbol{z}}_{\alpha\beta}$, k is the damping factor, $\sin(\hat{\theta}_e)$ and $\cos(\hat{\theta}_e)$ determines the synchronous frequency $\hat{\omega}_e$ of the desired fundamental signal, hence $\hat{\theta}_e = \hat{\omega}_e \cdot t$. $w_{\alpha\beta}$ is a variable used to derive the method.

It can be proven that the filter does not change the magnitude and no phase shift occurs at the synchronous frequency $\hat{\omega}_e$. From (4.2) to (4.9) the transfer function of the CCSFF is derived [Wu et al., 2022]. In figure 4.2 it is seen that the CCSSF output signals can be expressed as in (4.2).

$$
\begin{aligned}
\hat{z}_\alpha &= w_\alpha \cdot \cos(\hat{\omega}_e \cdot t) - w_\beta \cdot \sin(\hat{\omega}_e \cdot t) \\
\hat{z}_\beta &= w_\alpha \cdot \sin(\hat{\omega}_e \cdot t) + w_\beta \cdot \cos(\hat{\omega}_e \cdot t)
\end{aligned}
\tag{4.2}
$$

By differentiating (4.2) with respect to time (4.3) is given.

$$
\begin{aligned}
\dot{\hat{z}}_\alpha &= \dot{w}_\alpha \cdot \cos(\hat{\omega}_e \cdot t) - \dot{w}_\beta \cdot \sin(\hat{\omega}_e \cdot t) - \hat{\omega}_e \cdot \big(w_\alpha \cdot \sin(\hat{\omega}_e \cdot t) + w_\beta \cdot \cos(\hat{\omega}_e \cdot t) \big) \\
\dot{\hat{z}}_\beta &= \dot{w}_\alpha \cdot \sin(\hat{\omega}_e \cdot t) - \dot{w}_\beta \cdot \cos(\hat{\omega}_e \cdot t) + \hat{\omega}_e \cdot \big(w_\alpha \cdot \cos(\hat{\omega}_e \cdot t) - w_\beta \cdot \sin(\hat{\omega}_e \cdot t) \big)
\end{aligned}
\tag{4.3}
$$

From figure 4.2, the derivative of ω_α and ω_β can be expressed as in (4.4).

$$
\begin{aligned}
\dot{w}_\alpha &= k \cdot \big(\varepsilon_\alpha \cdot \cos(\hat{\omega}_e \cdot t) + \varepsilon_\beta \cdot \sin(\hat{\omega}_e \cdot t) \big) \\
\dot{w}_\beta &= k \cdot \big(- \varepsilon_\alpha \cdot \sin(\hat{\omega}_e \cdot t) + \varepsilon_\beta \cdot \cos(\hat{\omega}_e \cdot t) \big)
\end{aligned}
\tag{4.4}
$$

From figure 4.2, ε_α and ε_β are expressed as in (4.5).

$$
\varepsilon_\alpha = z_\alpha - \hat{z}_\alpha, \quad \varepsilon_\beta = z_\beta - \hat{z}_\beta
\tag{4.5}
$$

Based on (4.4) and (4.5), (4.3) can be simplified to (4.6).

$$\dot{\hat{z}}_\alpha = -\hat{\omega}_e \cdot \underbrace{\left(w_\alpha \cdot \sin(\hat{\omega}_e \cdot t) + w_\beta \cdot \cos(\hat{\omega}_e \cdot t)\right)}_{\hat{z}_\beta} - k \cdot (\hat{z}_\alpha - z_\alpha)$$

$$\dot{\hat{z}}_\beta = \hat{\omega}_e \cdot \underbrace{\left(w_\alpha \cdot \cos(\hat{\omega}_e \cdot t) - w_\beta \cdot \sin(\hat{\omega}_e \cdot t)\right)}_{\hat{z}_\alpha} - k \cdot (\hat{z}_\beta - z_\beta) \qquad (4.6)$$

Applying the Laplace transform to (4.6), the expression can be written as in (4.7)

$$(s + k) \cdot \hat{z}_\alpha(s) = k \cdot z_\alpha(s) - \hat{\omega}_e \cdot \hat{z}_\beta(s)$$
$$(s + k) \cdot \hat{z}_\beta(s) = k \cdot z_\beta(s) + \hat{\omega}_e \cdot \hat{z}_\alpha(s) \qquad (4.7)$$

By defining (4.8), the transfer function of the CCSFF is obtained in (4.9)

$$\boldsymbol{z}_{\alpha\beta}(s) = z_\alpha(s) + j \cdot z_\beta(s), \qquad \hat{\boldsymbol{z}}_{\alpha\beta}(s) = \hat{z}_\alpha(s) + j \cdot \hat{z}_\beta(s) \qquad (4.8)$$

$$G_{CCSFF}(s) = \frac{\hat{\boldsymbol{z}}_{\alpha\beta}}{\boldsymbol{z}_{\alpha\beta}}(s) = \frac{k}{s - j \cdot \hat{\omega}_e + k} \qquad (4.9)$$

The bode diagram of 4.9 is illustrated in figure 4.3, for different k values. The synchronous frequency $\hat{\omega}_e$ is set to $500\,\text{rad/s}$.
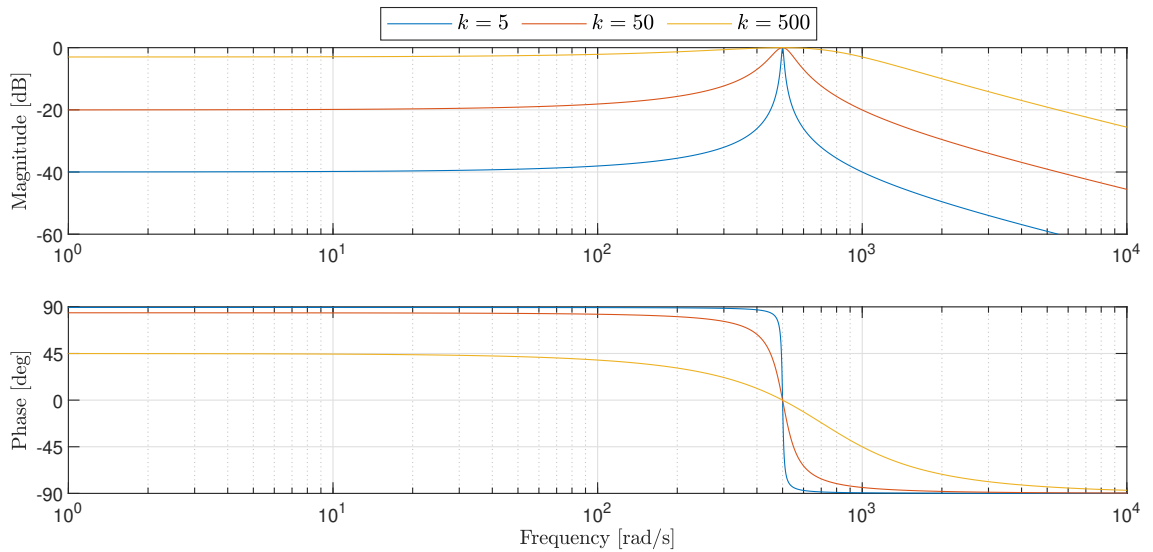
Figure 4.3. Bode diagram of the CCSFF for various values of k with $\hat{\omega}_e = 500\,\text{rad/s}$.

From the bode diagram of the CCSFF in figure 4.3 it is seen that it provides the characteristic of a bandpass filter at the synchronous frequency $\hat{\omega}_e$ and can pass the fundamental component without magnitude attenuation and phase delay. The magnitude at the synchronous frequency is also given in (4.10). Hence $\omega = \hat{\omega}_e$.

$$\left| \frac{\hat{\boldsymbol{z}}_{\alpha\beta}(j \cdot \omega)}{\boldsymbol{z}_{\alpha\beta}(j \cdot \omega)} \right|_{\omega = \hat{\omega}_e} = \frac{k}{\sqrt{k^2}} = 1 \qquad (4.10)$$

Furthermore, it is seen that the CCSFF's ability to suppress the harmonic components is strictly related to the damping factor k. This is also given in (4.11) where the magnitude of the (6 ± 1)th harmonics are used for calculation.

$$\left| \frac{\hat{\boldsymbol{z}}_{\alpha\beta}(j \cdot \omega)}{\boldsymbol{z}_{\alpha\beta}(j \cdot \omega)} \right|_{\omega = \pm(6\pm1)\hat{\omega}_e} = \frac{k}{\sqrt{(\pm6\hat{\omega}_e)^2 + k^2}} = \mu \tag{4.11}$$

According to (4.11), μ determines the harmonic suppression capability. It is seen that the harmonic suppression can be improved by decreasing μ which implies that the damping factor should be low, depending on the desired filtering performance.

Therefore, the output from the CCSFF can be expressed as in (4.12) if μ is assumed to be small ($\mu \approx 0$).

$$\hat{z}_\alpha \approx \hat{Z} \cdot \cos(\hat{\omega}_e \cdot t) + \mu \cdot \hat{Z}_{6\pm1} \cdot \cos(\pm(6 \pm 1) \cdot \hat{\omega}_e \cdot t) \approx \hat{Z} \cdot \cos(\hat{\omega}_e \cdot t)$$
$$\hat{z}_\beta \approx \hat{Z} \cdot \sin(\hat{\omega}_e \cdot t) + \mu \cdot \hat{Z}_{6\pm1} \cdot \sin(\pm(6 \pm 1) \cdot \hat{\omega}_e \cdot t) \approx \hat{Z} \cdot \sin(\hat{\omega}_e \cdot t) \tag{4.12}$$

According to (4.12) the CCSFF eliminates the harmonics and passes the fundamental component if k is designed properly such that $\mu \approx 0$. The filter is tested on the system illustrated in figure 4.1. For simplicity, the CLFO is disregarded and a distorted waveform containing (6 ± 1)th order harmonic components as expressed in (4.1) is used as input to the CCSFF. The magnitude of the fundamental, 5th, and 7th order harmonic components used in the tests are $Z = 1$, $Z_{5th} = 0.2$, and $Z_{7th} = 0.1$, respectively. The CCSFF is tested for different k values when $\omega_m = 900\,\mathrm{rpm}$. The feedback $\hat{\theta}_e$ used in the CCSFF is fixed at the same frequency of the input signal, hence $\omega_e = \hat{\omega}_e$. The result is illustrated in figure 4.4.
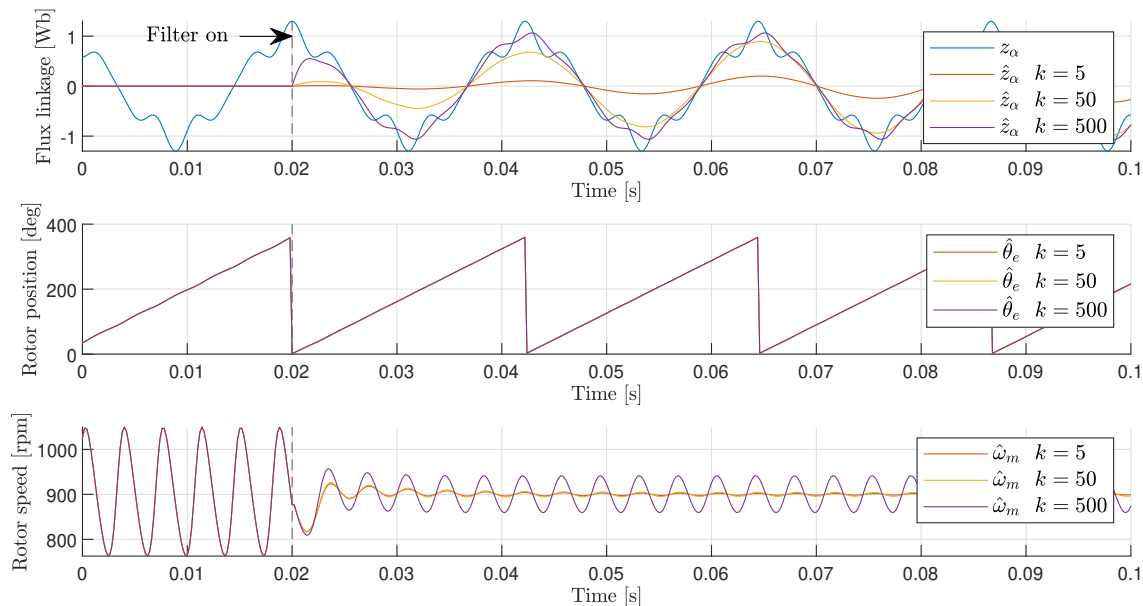

Figure 4.4. Filtering capability of the CCSFF with θ_e used as feedback.

From the active flux waveform, it is seen that the CCSFF starts to track the frequency of the input signal as it is enabled. Furthermore, it is seen that by lowering the damping

factor k, the filtering capability can be improved. This is further seen in the estimated speed as the oscillations are decreased. However, it is also seen that the k value affects the settling time of the CCSFF. When $k = 5$ the settling time of the CCSFF is slow. However, over time the CCSFF will track the fundamental component of the input signal.

In figure 4.4 the feedback $\hat{\theta}_e$ is fixed at the same frequency as the input signal. To make the CCSFF frequency adaptive, the frequency of the feedback signal $\hat{\theta}_e$ should change if the input signal does. In real application, the frequency is expected to change as the motor is run at different speeds which will change the frequency of the input signal. To cope with this, the estimated position from the PLL can advantageously be used as feedback in the CCSFF system as the real frequency of the input signal $Z_{\alpha\beta}$ may not be available. The same test as in figure 4.4 is performed while using the estimated position from the PLL as feedback. The results are illustrated in figure 4.5.
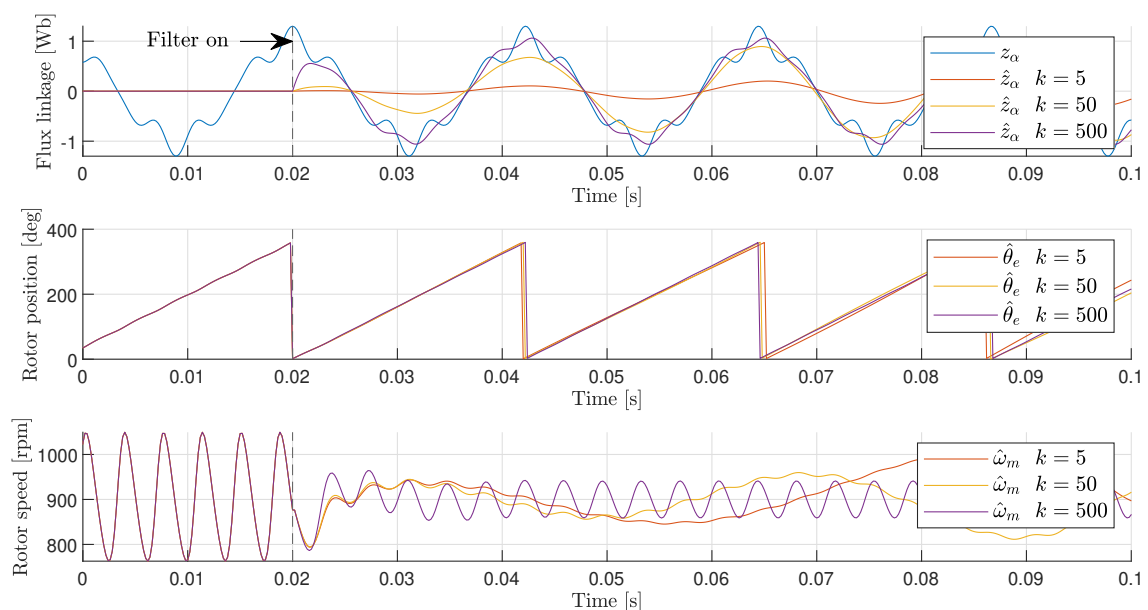
Figure 4.5. Filtering capability of the CCSFF with estimated position $\hat{\theta}_e$ used as feedback.

From the tests it is seen that using the estimated position as feedback, the estimated position and speed are not estimated properly for $k = 5$ and $k = 50$. It is noticed that the system becomes unstable. This is due to the settling time of the CCSFF response which is slow when k is designed too small. When the response of the CCSFF is too slow, the PLL cannot estimate the position properly. As the CCSFF uses the estimated position as feedback, it cannot run. Thus, the settling time should be considered when designing the CCSFF, as the estimated position $\hat{\theta}_e$ is obtained from the PLL and used as feedback in the CCSFF. Hence, proper parameters in the CCSFF and PLL are essential to suppress the harmonic components and ensure a precise position estimation.

The CCSFF-PLL system is linearized to analyze the dynamic interaction between the CCSFF and PLL to ensure precise harmonic suppression and precise position estimation. The input and output signal in the CCSFF can be derived as in (4.13) according to figure 4.2.

$$z_\alpha = Z \cdot \cos(\theta_e), \qquad z_\beta = Z \cdot \sin(\theta_e)$$
$$\hat{z}_\alpha = \hat{Z} \cdot \cos(\bar{\theta}_e), \qquad \hat{z}_\beta = \hat{Z} \cdot \sin(\bar{\theta}_e) \tag{4.13}$$

The angle $\bar{\theta}_e$ is obtained utilizing arctangent as in (4.14).

$$\bar{\theta}_e = \arctan\frac{\hat{z}_\beta}{\hat{z}_\alpha} \tag{4.14}$$

The time derivative of (4.14) is given in (4.15).

$$\frac{d\bar{\theta}_e}{dt} = \frac{\hat{z}_\alpha \frac{d\hat{z}_\beta}{dt} - \hat{z}_\beta \frac{d\hat{z}_\alpha}{dt}}{(\hat{z}_\alpha)^2 + (\hat{z}_\beta)^2} \tag{4.15}$$

The time derivative of $\hat{\boldsymbol{z}}_{\alpha\beta}$ is given in (4.16) by rearranging (4.7) and applying the inverse Laplace transform.

$$\frac{d\hat{z}_\alpha}{dt} = -\hat{\omega}_e \cdot \hat{z}_\beta + k \cdot (z_\alpha - \hat{z}_\alpha)$$
$$\frac{d\hat{z}_\beta}{dt} = \hat{\omega}_e \cdot \hat{z}_\alpha + k \cdot (z_\beta - \hat{z}_\beta) \tag{4.16}$$

By substituting (4.16) into (4.15), (4.17) is given.

$$\frac{d\bar{\theta}_e}{dt} = \hat{\omega}_e + \frac{k \cdot (z_\beta \cdot \hat{z}_\alpha - z_\alpha \cdot \hat{z}_\beta)}{(\hat{z}_\alpha)^2 + (\hat{z}_\beta)^2} \tag{4.17}$$

By substituting the input and output signals in (4.13), (4.17) is simplified to (4.18).

$$\frac{d\bar{\theta}_e}{dt} = \hat{\omega}_e + k \cdot \frac{Z}{\hat{Z}} \cdot \sin(\theta_e - \bar{\theta}_e) \tag{4.18}$$

By introducing (4.19), (4.18) is simplified to (4.20).

$$\theta_e \approx \bar{\theta}_e, \qquad Z \approx \hat{Z} \tag{4.19}$$

$$\frac{d\bar{\theta}_e}{dt} = \hat{\omega}_e + k(\theta_e - \bar{\theta}_e) \tag{4.20}$$

Based on (4.20), a transfer function for the CCSFF system can be established as in (4.21).

$$G_{CCSFF}(s) = \frac{\bar{\theta}_e}{\theta_e} = \frac{1}{\theta_e} \cdot \frac{k \cdot \theta_e + s \cdot \hat{\theta}_e}{s + k} \tag{4.21}$$

The transfer function for the whole CCSFF-PLL system can be derived as in (4.23), based on the transfer function for the CCSFF and PLL in (4.21) and (4.22), respectively.

$$G_{PLL}(s) = \frac{\hat{\theta}_e}{\bar{\theta}_e} = \frac{s \cdot k_p + k_i}{s^2 + s \cdot k_p + k_i} \tag{4.22}$$

$$G(s) = \frac{\bar{\theta}_e}{\theta_e} \cdot \frac{\hat{\theta}_e}{\bar{\theta}_e} = \frac{\hat{\theta}_e}{\theta_e} = \frac{s \cdot k \cdot k_p + k \cdot k_i}{s^3 + s^2 \cdot k + s \cdot k \cdot k_p + k \cdot k_i} \tag{4.23}$$

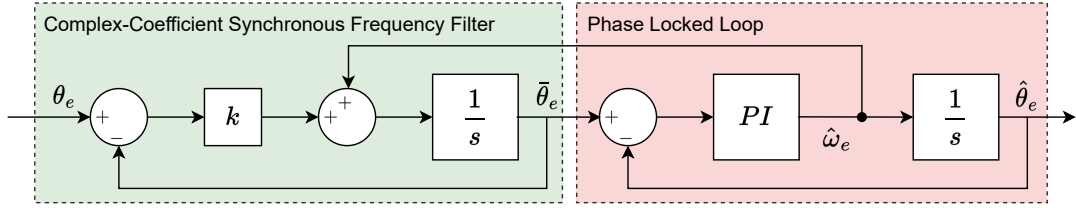The system is illustrated in figure 4.6.

Figure 4.6. Block diagram of the linearized CCSFF-PLL system.

With the established transfer function it can simultaneously be proven that the system adds no phase shift to the rotor position in steady state utilizing the final value theorem. For a normal PLL type filter there is no phase shift in steady state [Wang et al., 2017]. The same calculations as in [Wang et al., 2017] is derived for the CCSFF-PLL system. The error can be defined as in (4.24) using the definition given in (2.12).

$$\tilde{\theta}_e(s) = (G(s) - 1) \cdot \theta_e(s) \tag{4.24}$$

For a ramp input, θ_e can be written as $\theta_e = a \cdot t$ where a is the slope of θ_e. The error of the CCSFF-PLL system converges as in (4.25).

$$\begin{aligned}
\lim_{t \to \infty} \tilde{\theta}_e &= \lim_{s \to 0} s \cdot \tilde{\theta}_e(s) = \lim_{s \to 0} s \cdot (G(s) - 1) \cdot \frac{a}{s^2} \\
&= \lim_{s \to 0} s \cdot \left(\frac{s \cdot k \cdot k_p + k \cdot k_i}{s^3 + s^2 \cdot k + s \cdot k \cdot k_p + k \cdot k_i} - 1 \right) \cdot \frac{a}{s^2} \\
&= \lim_{s \to 0} -\frac{s \cdot a \cdot (k + s)}{s^3 + (s^2 + s \cdot k_p + k_i) \cdot k} = 0
\end{aligned} \tag{4.25}$$

From (4.25) it is seen that the error converges to zero for a ramp input, hence no phase shift is added to the estimated position at steady state.

Utilizing the PI parameters $k_p = 403$ and $k_i = 40648$ for the PLL obtained in section 2.3.2, the effects of the damping factor gain k on the CCSFF-PLL system are analyzed. In figure 4.7 a pole/zero map of the CCSFF-PLL system is illustrated when the damping factor gain k is varied.
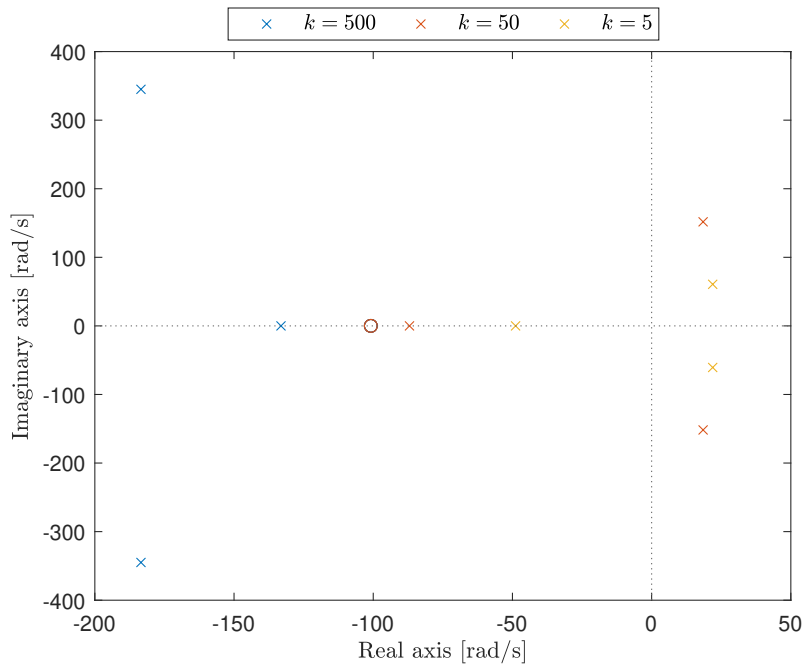
Figure 4.7. Pole/zero map of the CCSFF-PLL system for different k values.

It is seen that the placement of the zero is not affected by the value of k, as for all analyzed values of k the zero is placed at approximately -101. It is observed that the complex set of poles enters the right half plane when k is decreased. This means that the CCSFF-PLL becomes unstable if the damping factor k is chosen too low. This also appears in the test illustrated in figure 4.5 where only the CCSFF-PLL with $k = 500$ are capable of estimating the position.

In the previous analysis, it is mentioned that the k gain should be designed with a low value to obtain sufficient harmonic suppression capability. However, the pole/zero map in figure 4.7 and the results in figure 4.5 shows that the minimum value of k is limited to ensure a stable system. Hence it is desired to examine whether a design approach can be used to determine the CCSFF-PLL parameters.

From (4.23) and figure 4.6 it is seen that the CCSFF-PLL system is a third order system. By introducing the structure of a third order system in (4.26), the parameters can be defined as in (4.27).

$$G(s) = \frac{s \cdot \omega_n^2 \cdot (2 \cdot \zeta + 1) + \omega_n^3}{s^3 + s^2 \cdot \omega_n \cdot (2 \cdot \zeta + 1) + s \cdot \omega_n^2 \cdot (2 \cdot \zeta + 1) + \omega_n^3} \tag{4.26}$$

$$k = (2 \cdot \zeta + 1) \cdot \omega_n, \quad k \cdot k_p = (2 \cdot \zeta + 1) \cdot \omega_n^2, \quad k \cdot k_i = \omega_n^3 \tag{4.27}$$

Where ζ is the damping ratio and ω_n is the natural frequency. Setting the damping ratio to $\zeta = 1$ the parameters in the CCSFF-PLL can be designed as in (4.28).

$$k = 3 \cdot \omega_n, \quad k_p = \omega_n, \quad k_i = \frac{\omega_n^2}{3} \tag{4.28}$$

A linear relationship between the natural frequency ω_n and the bandwidth ω_c is established to determine the parameters in (4.28). Figure 4.8 illustrates the bode diagram of $G(s)$ in (4.26) for different ω_n.
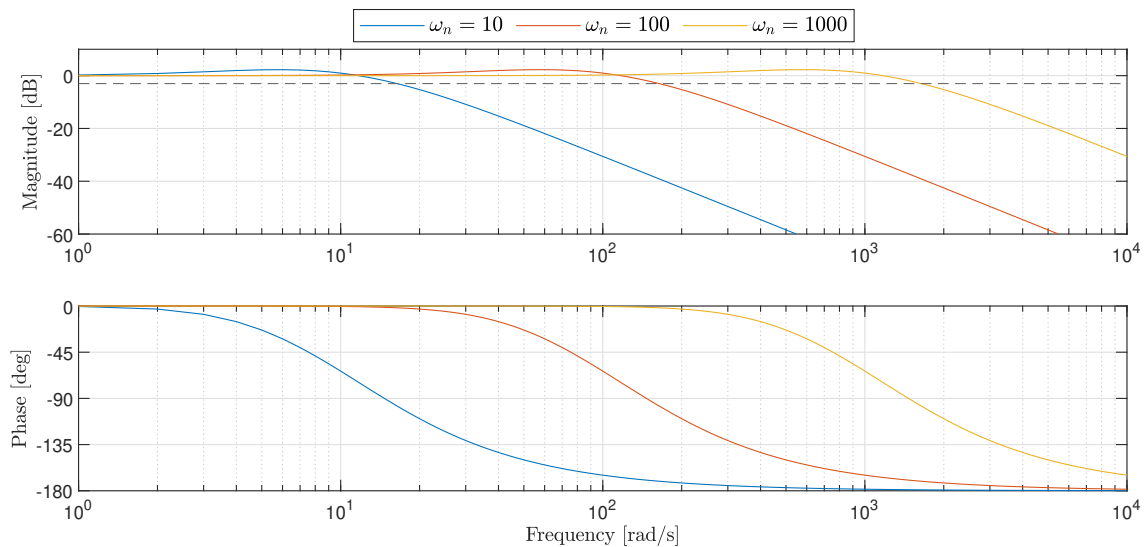

Figure 4.8. Bode diagram of the CCSFF-PLL system.

From the bode diagram, the bandwidth is allocated at $-3\,\text{dB}$. Based on this, a linear relationship between the natural frequency ω_n and the bandwidth ω_c is established such that $\omega_c = 1.64 \cdot \omega_n$. From the bode diagram, it is seen that by increasing the natural frequency ω_n, the CCSSF-PLL bandwidth is increased which improves the transient response but degrades the filtering capability. Thus, the CCSFF should be designed such that the natural frequency gives the desired bandwidth. It is revealed in section 3.1 that the dominant position harmonic frequency is $6 \cdot \omega_e$. Thus, the CCSFF-PLL is designed to have a bandwidth less than the 6th harmonic frequency to ensure harmonic suppression capability, hence $\omega_c < 6 \cdot \omega_e$.

To evaluate the parameter design of the CCSFF-PLL's effects on the harmonic suppression capability and the dynamic performance, two systems are designed with bandwidth $\omega_c = 250\,\text{rad/s}$ and $\omega_c = 500\,\text{rad/s}$. The CCSFF-PLL parameters are calculated utilizing (4.28) and are listed in table 4.1. To evaluate the performance using the respective designed CCSFFs, two PLL systems are designed with similar bandwidths for comparison. The PLL parameters are calculated utilizing (2.23) and are listed in table 4.1.

Position estimator	k_p	k_i	k	$\omega_c[\text{rad/s}]$
CCSFF 1	152	7746	457	250
CCSFF 2	305	30984	915	500
PLL 1	202	10162	-	250
PLL 2	403	40648	-	500

Table 4.1. CCSFF-PLL and PLL parameters.

Based on the designed systems the expected filtering capability can be shown utilizing the

derived transfer functions for the PLL and CCSFF-PLL in (4.22) and (4.23) respectively. Figure 4.9 illustrates the magnitude plot for the systems listed in table 4.1. The corresponding frequency of the 6th order harmonic is indicated when $\omega_m = 360$ rpm and $\omega_m = 1800$ rpm as the designed systems is analyzed through experimental tests at these speeds in section 4.3.
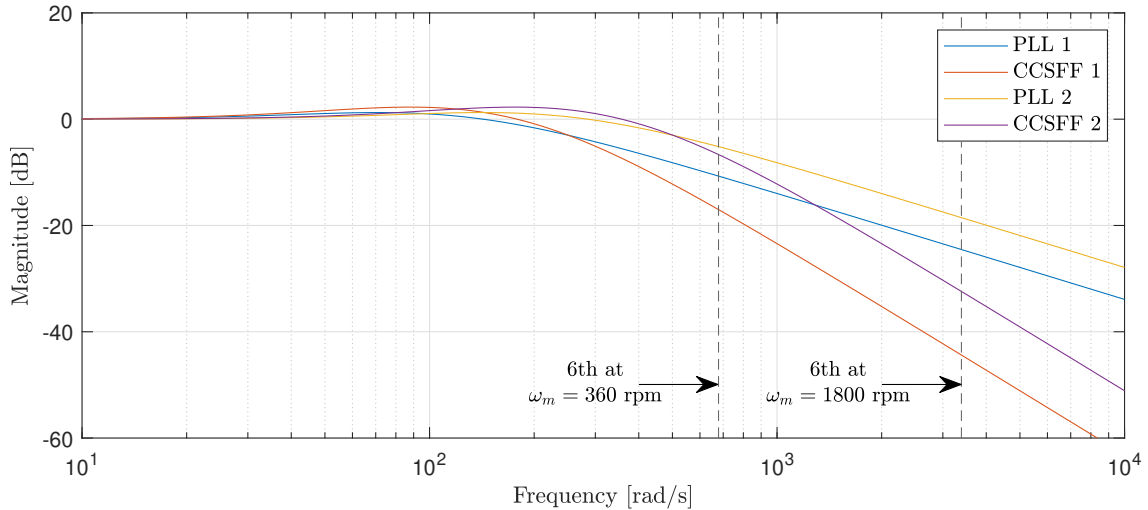

Figure 4.9. Magnitude plot of the PLL and CCSFF-PLL listed in table 4.1.

From the magnitude plot, the expected attenuation of the 6th order harmonic performed by the CCSFF relative to the PLL is obtained. It is seen, that when the PMSM is run at 360 rpm, only a small difference is seen between PLL 2 and CCSFF 2. Thus, the harmonic suppression capability of the CCSFF 2 at this speed is not sufficient. However, as the speed is increased the harmonic suppression of the CCSFF 2 is improved compared to PLL 2. The ratio of the magnitude between CCSFF 1 and PLL 1 is larger, compared to CCSFF 2 and PLL 2. Thus, the CCSFF 1 ensures better harmonic suppression capability.

4.2   Harmonic supression capability

The harmonic suppression capability of the CCSFF is validated by examining the estimated active flux input to the CCSFF and the output active flux from the CCSFF. The input and output $\alpha\beta$ active flux is illustrated in figure 4.10 along with the frequency spectrum obtained from FFT analysis of the active flux. The test is performed with the PMSM run at 1800 rpm with 2 Nm load applied using the CCSFF 1 from table 4.1.
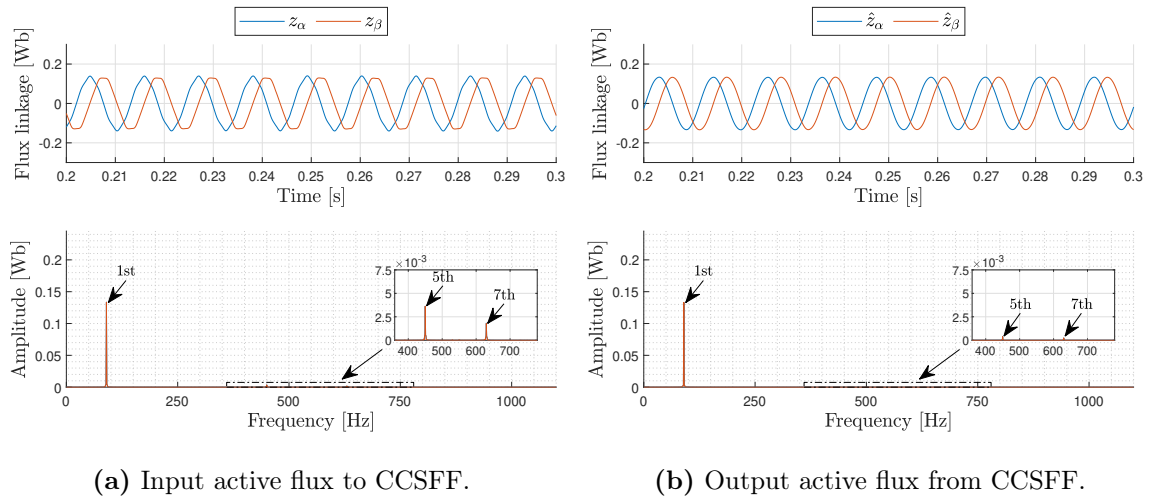
(a) Input active flux to CCSFF.

(b) Output active flux from CCSFF.

Figure 4.10. $\alpha\beta$ active flux and the frequency spectrum of the input and output of the filter using the CCSFF 1. The PMSM is run at 1800 rpm with 2 Nm load applied.

From figure 4.10(a) it is seen, that the active flux waveform of the input to the CCSFF is distorted. The frequency spectrum of the active flux shows, that the distortion is caused mainly by the (6 ± 1)th order harmonic components. Figure 4.10(b) shows that the active flux waveform of the output of the CCSFF becomes more sinusoidal. From the frequency spectrum, it is further seen that the amplitude of the (6 ± 1)th order harmonic components are reduced significantly, leading to a more sinusoidal waveform. This indicates that the proposed CCSFF provides fine harmonic suppression capabilities.

The harmonic suppression capabilities are further analyzed by examining the estimated position and the position error. The estimated position and position error obtained using CCSFF 1 and CCSFF 2 are compared to analyze the effect of the parameter design. Figures 4.11 and 4.12 illustrates the electrical rotor position and the position error when the PMSM is run at 360 rpm and 1800 rpm, respectively. The tests are performed with 2 Nm load applied to the system.
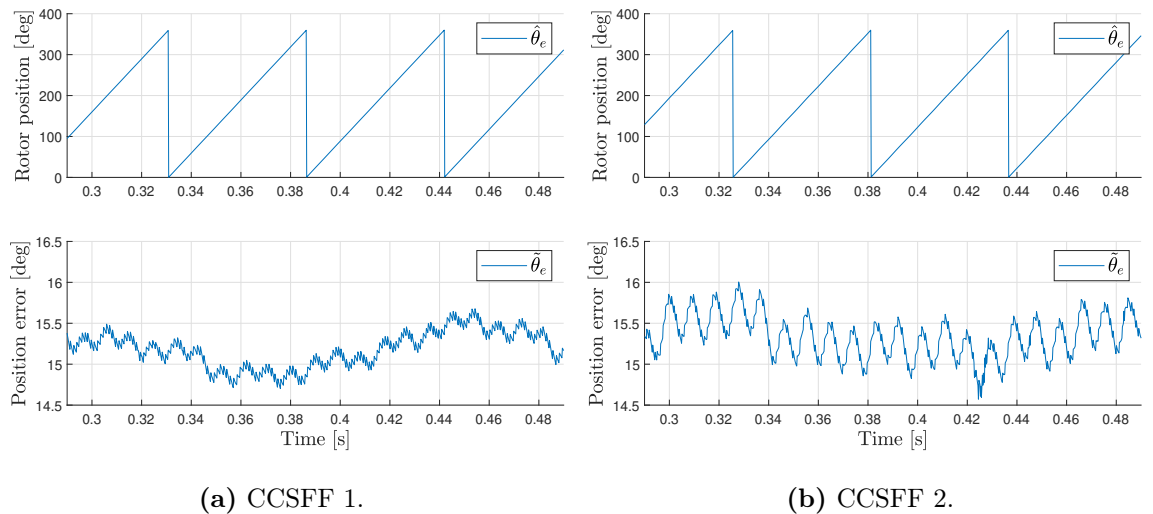

(a) CCSFF 1.

(b) CCSFF 2.

Figure 4.11. Electrical rotor position and the position error when the PMSM is run at 360 rpm with 2 Nm load.

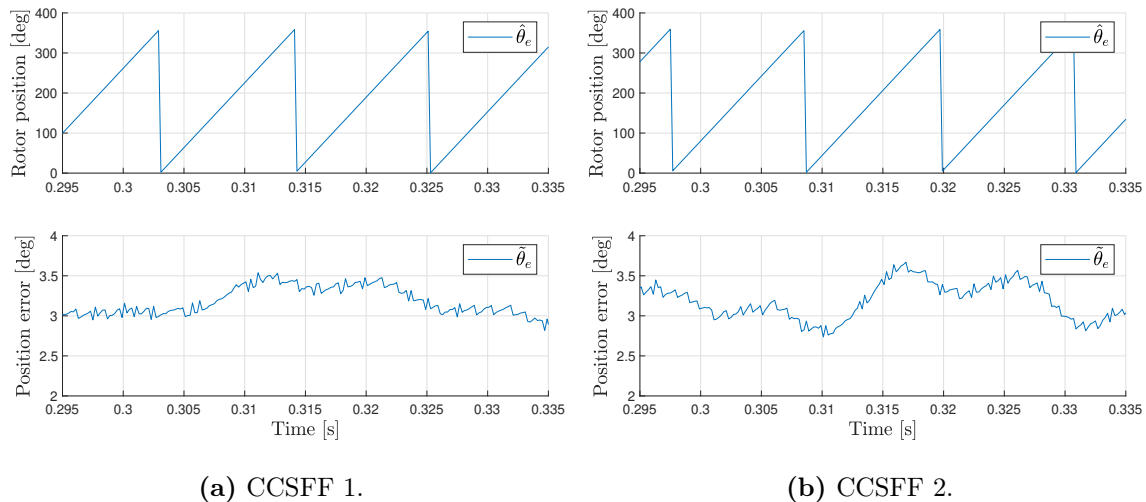(a) CCSFF 1.   (b) CCSFF 2.

Figure 4.12. Electrical rotor position and the position error when the PMSM is run at 1800 rpm with 2 Nm load.

When the PMSM is run at 360 rpm, obvious 6th order harmonic ripples are seen in the position error when using either CCSFF 1 or CCSFF 2, as seen in figure 4.11. However, it is seen, that the 6th order harmonic ripples in the position error are less significant when using the CCSFF 1 parameters. When the PMSM is run at 1800 rpm it is seen from 4.12 that the 6th order harmonic ripples are removed using either of the CCSFF-PLL designs from table 4.1. From the position error, there seems no difference using either of the CCSFF-PLL designs.

The harmonic suppression capability of the two designed CCSFFs seen in figures 4.11 and 4.12 is consistent with the observations seen from the magnitude plot illustrated in figure 4.9. The bandwidth of the CCSFF 1 is smaller than the CCSFF 2 as described in section 4.1. Thus, it is expected that the harmonic suppression capability is better using the CCSFF 1 rather than the CCSFF 2. However, using the CCSFF 1 when the PMSM is run at 360 rpm, the 6th order harmonic component is not completely removed. As the speed increases, the two designed CCSFF-PLL systems seem to have comparable suppression capabilities as seen from figure 4.12. When the PMSM is run at 1800 rpm both designed CCSFF-PLL system provide sufficient suppression of the 6th order harmonic component.

Based on the analysis of the estimated active flux and the position error, it is seen that the CCSFF method is able to detect and suppress the harmonic distortion caused by the inverter nonlinearities and spatial flux harmonics as intended. The parameter design and particularly the bandwidth of the filter highly affects the harmonic suppression capability. Operating the PMSM at a lower speed range, the CCSFF-PLL must be designed with low bandwidth to suppress the 6th order harmonic component in the estimated rotor position. However, in the higher speed range, the bandwidth can be designed higher as the frequency of the 6th order harmonic component increases as well. The dynamic performance using the CCSFF method along with the effects of the parameter design is further elaborated in the following section.

4.3   Performance evaluation

As the principal of the CCSFF method and the functionality is validated in the previous section, the CCSFFs listed in table 4.1 are tested with the laboratory setup at different conditions to analyze dynamic performance along with further analysis of the harmonic suppression capability. To elaborate on whether the dynamic performance is affected by the CCSFF, tests are performed using PLLs which are designed with the same bandwidth as the CCSFF-PLL systems in table 4.1. The parameters of the designed PLLs are listed in table 4.1 as well.

The dynamic performance is examined by accelerating the PMSM from 900 rpm to 1800 rpm. Figure 4.13 illustrates the estimated rotor speed and the position error for tests using the designed PLLs and CCSFFs listed in table 4.1. The tests are performed with 2 Nm load applied to the system.
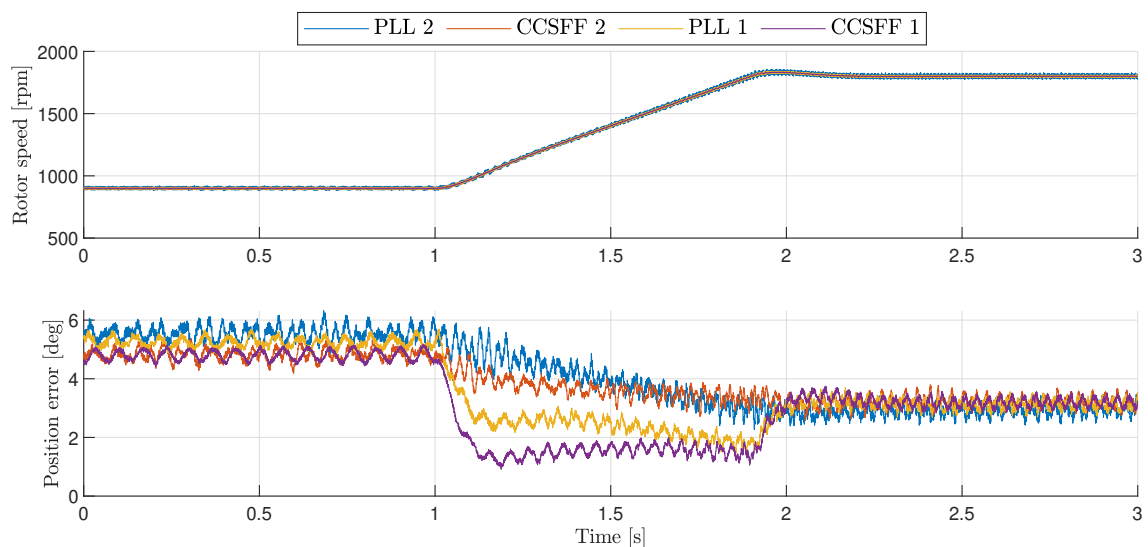
Figure 4.13. Estiamted rotor speed and position error for tests using the PLL 1, CCSFF 1, PLL 2, and CCSFF 2 listed in table 4.1 when the PMSM is accelerated.

It is seen, that the estimated speed for all tests is similar. From the tests it is seen, that the position error at time $0 \leq t \leq 1$ is less using the CCSFF method compared to using only PLL with same bandwidth. When the speed is 1800 rpm at time $2 \leq t \leq 3$ the position error for all test are more similar. When the PMSM is accelerated, the response of the position error for tests with PLL 2 and CCSFF 2 are similar. For the PLL 1 and CCSFF 1 it is seen, that when the speed starts to accelerate, the position error drops before it is stabilized when the speed reaches steady state. This indicates a delay in the position estimator, as the estimated position does not follow the real speed as the speed is accelerated. The PLL 1 and CCSFF 1 have lower bandwidth, hence the dynamic performance is expected to be different from PLL 2 and CCSFF 2.

The dynamic performance is further examined by exposing the system to a sudden load change. Tests are performed with sensorless control with a speed reference at 360 rpm with 2 Nm load applied using the load motor. During the tests, a step load is applied increasing

the load from 2 Nm to 6 Nm and from 6 Nm to 2 Nm to examine the dynamic response of the system. Figure 4.14 illustrates the estimated rotor speed and the position error for the tests.
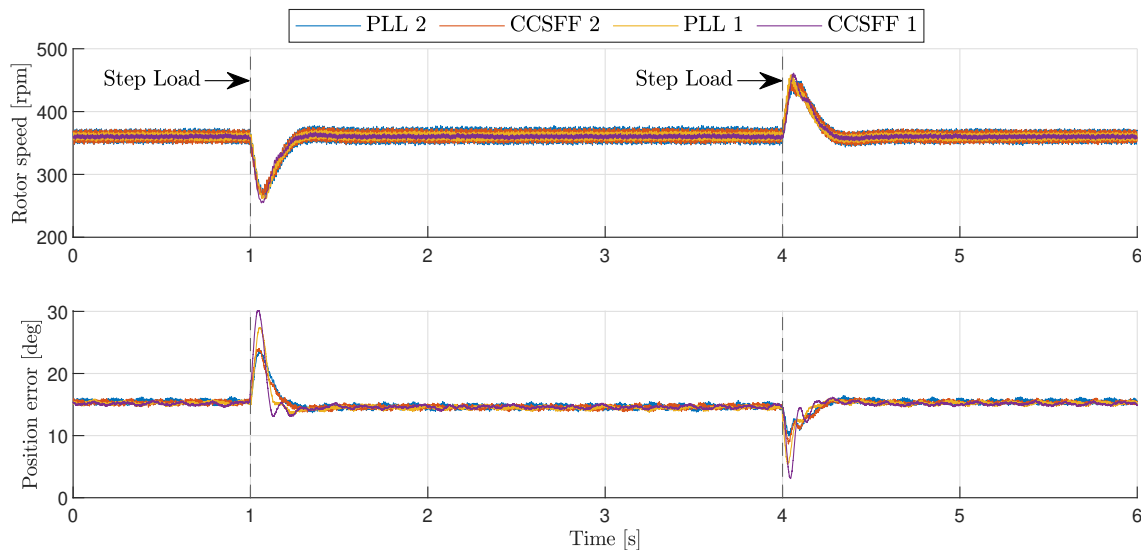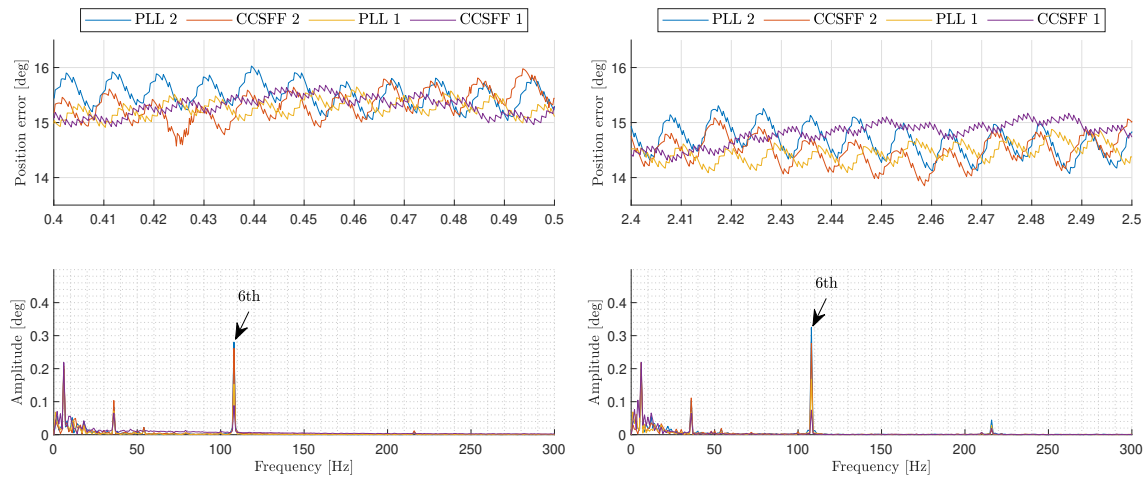

Figure 4.14. Estiamted rotor speed and position error for tests using the PLL 1, CCSFF 1, PLL 2, and CCSFF 2 listed in table 4.1 when a 4 Nm step load is applied to the system.

It is seen, that when a step load is exposed to the system, a delay between the estimated signal and the encoder occurs, as the position error changes when the load is applied. As the bandwidth of the PLL 2 and CCSFF 2 is designed larger than PLL 1 and CCSFF 1, it is expected, that the transient response of PLL 2 and CCSFF 2 is better. This is further seen in the figure as the peak in the position error is smaller compared to PLL 1 and CCSFF 1. When the CCSFF 2 system is used, the response is comparable with the test using only a PLL structure without a filter with the same bandwidth. Thus, when the bandwidth of the CCSFF-PLL system is designed high enough, the CCSFF structure will not introduce further delays to the system.

The PLL 1 and CCSFF 1 are designed with half the bandwidth of PLL 2 and CCSFF 2, hence the dynamic performance of the low bandwidth systems is expected to be worse. This is further seen in the figure, as when the step load is applied, the position error is larger compared to the other tests with higher bandwidth. Comparing the CCSFF 1 and PLL 1 it is seen that the CCSFF 1 introduces further delay to the estimation, as the peak of the position error is larger than when the PLL 1 is used. Furthermore, the position error converges slower to a steady state value using the CCSFF compared to the PLL 1 test.

The CCSFF 2 does not introduce a remarkable difference in the transient response compared to only using a PLL. The CCSFF 1 is designed with lower bandwidth, hence a larger delay is introduced which affects the transient response. However, it is seen from the estimated speed response and the position error, that the CCSFF 2 seems more fluctuating, compared to the CCSFF 1. This indicates that when using the CCSFF 2, the harmonic suppression capability is poor. Thus, to analyze more the harmonic suppression capability of the two designed CCSFFs, a FFT analysis is performed at steady state speed which is

illustrated in figure 4.15 along with the position error. Figure 4.15(a) is based on the data before the step load is applied at time $0 \leq t \leq 1$ and figure 4.15(b) is based on the data at time $2 \leq t \leq 3$.

(a) 2 Nm load at time $0 \leq t \leq 1$ from figure 4.14.

(b) 6 Nm load at time $2 \leq t \leq 3$ from figure 4.14.

Figure 4.15. Position error and harmonic amplitude obtained from FFT analysis for tests using the PLL 1, CCSFF 1, PLL 2, and CCSFF 2 listed in table 4.1. FFT analysis is performed at steady state speed.

It is seen, that the position error using the low bandwidth filter CCSFF 1 is more constant, with only small fluctuation caused by high frequency noise. The CCSFF 2 has a similar position error as PLL 2, which indicates that the filter does not suppress the 6th harmonic component sufficiently. This is the case when either 2 Nm or 6 Nm is applied to the system. This is further seen from the illustration of the harmonic amplitude from the FFT. It is seen that when CCSFF 2 is used, the 6th harmonic component is not reduced to the same extent as using CCSFF 1. This substantiates the analysis of the harmonic capability of the CCSFF shown in section 4.2. The CCSFF 2 does suppress the 6th order harmonic component to some extent, compared to using the PLL 2, which has the same bandwidth. However, the effects of the CCSFF 2 are not sufficient. Using the CCSFF 1, which has smaller bandwidth, the amplitude of the 6th harmonic component is reduced significantly. The CCSFF 1 also provides better harmonic suppression capabilities than using the PLL 1 with the same bandwidth. To better evaluate the suppression of the 6th order harmonic component, the amplitude of the corresponding 6th order harmonic component for the results illustrated in figure 4.15 are listed in table 4.2.

	6th amplitude [deg]	
	$\tau_L = 2\,\text{Nm}$	$\tau_L = 6\,\text{Nm}$
PLL 1	0.1533	0.1678
CCSFF 1	0.0881	0.0746
PLL 2	0.2812	0.3253
CCSFF 2	0.2625	0.2764

Table 4.2. Amplitude of the 6th order harmonic component in the position error $\tilde{\theta}_e$ using PLL 1, PLL 2, CCSFF 1, and CCSFF 2 listed in table 4.1 when $\omega_m = 360\,\text{rpm}$.

From the table it is seen when CCSFF 1 is used, the 6th order harmonic component is approximately halved compared to using PLL 1, which has similar bandwidth. The CCSFF 2 does not suppress the 6th order harmonic component in the estimated position significantly compared to the PLL 2, which has similar bandwidth. This is the case either when 2 Nm or 6 Nm is applied to the system.

It is expected that the CCSFF 2 will provide poor harmonic suppression capability at lower speed. However, as the speed of the PMSM increases, the harmonic suppression capability is expected to be improved. Hence, similar tests with the two CCSFFs and the PLLs are performed at 1800 rpm, to see whether differences in the harmonic suppression capability, as well as the transient response, are seen. Figure 4.16 illustrates the estimated rotor speed and the position error for tests using the two designed CCSFFs and the PLLs listed in table 4.1. A FFT analysis is performed at steady state speed which is illustrated in figure 4.17 along with the position error. Figure 4.17(a) is based on the data before the step load is applied at time $0 \leq t \leq 1$ and figure 4.17(b) is based on the data at time $2 \leq t \leq 3$.
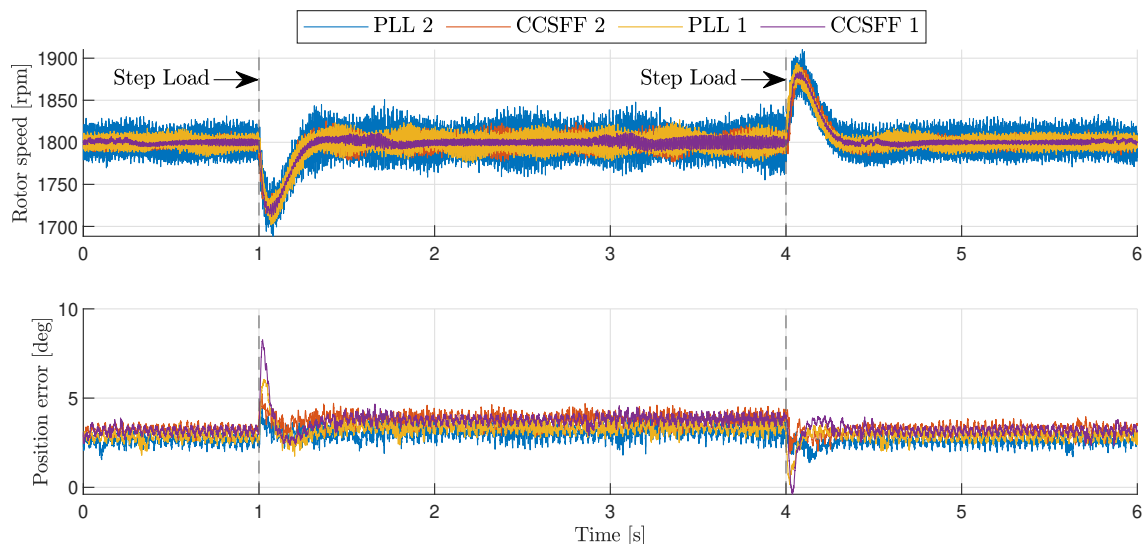

Figure 4.16. Estiamted rotor speed and position error for tests using the PLL 1, CCSFF 1, PLL 2, and CCSFF 2 listed in table 4.1 when a 4 Nm step load is applied to the system.

Examining figure 4.16 the same tendencies of the dynamic performance is seen compared to the test at 360 rpm seen in figure 4.14. The high bandwidth systems, PLL 2 and CCSFF 2,

have similar responses when a step load is applied to the system as seen from the position error. However, the CCSFF 2 seems to have an offset in the position error compared to the PLL 2 test. The lower bandwidth PLL 1 and CCSFF 1 systems have larger peak position errors when the step load is applied. Further, the CCSFF 1 has a larger peak than is the case with the PLL 1. From the estimated speed at time $1 \leq t \leq 4$ when $6 \, \text{Nm}$ load is applied to the system it is seen, that the speed ripples vary. This is the case for all tests. From figure 4.16 it seems only to be the case when $6 \, \text{Nm}$ load is applied. The cause of these ripple variations in the estimated speed is not further examined as it is seen in all tests, hence it is not introduced by the implementation of the CCSFF method.
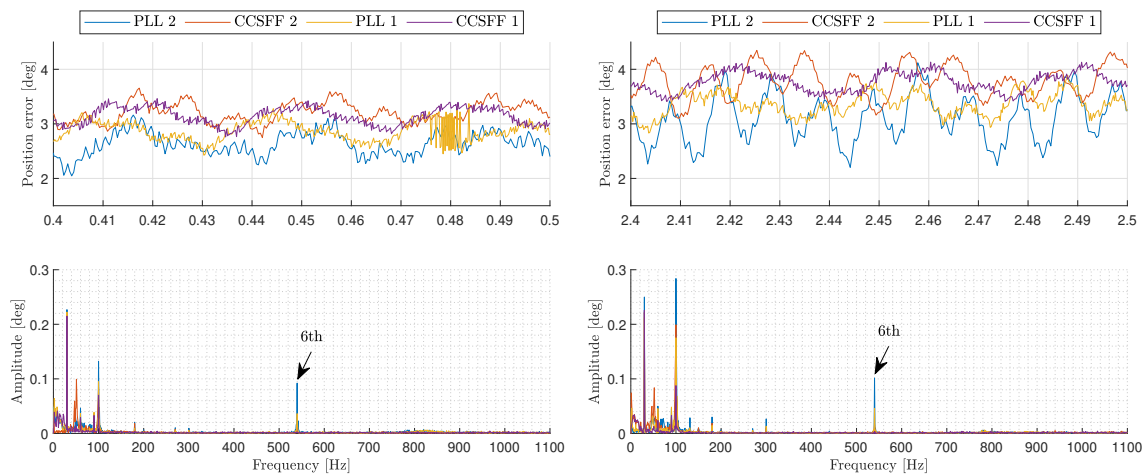
(a) $2 \, \text{Nm}$ load at time $0 \leq t \leq 1$ from figure 4.16.

(b) $6 \, \text{Nm}$ load at time $2 \leq t \leq 3$ from figure 4.16.

Figure 4.17. Position error and harmonic amplitude obtained from FFT analysis for tests using the PLL 1, CCSFF 1, PLL 2, and CCSFF 2 listed in table 4.1. FFT analysis is performed at steady state speed.

It is seen from figure 4.17, that the CCSFF 1 still provides good harmonic suppression capability. From the position error, the CCSFF 1 seems to have the same small fluctuations as seen at $360 \, \text{rpm}$. The CCSFF 1 has a significantly lower bandwidth than the 6th order harmonic component at $1800 \, \text{rpm}$, hence good harmonic suppression capability is seen, as the 6th order harmonic component is reduced to be insignificant. The position error for the CCSFF 2 is now more similar to CCSFF 1. From the frequency spectrum it is further seen, that the CCSFF 2 now is capable of suppressing the 6th order harmonic component to an insignificant level. It is seen, that the amplitude of the 6th order harmonic component is reduced using the CCSFF 2 compared to the PLL 2, which has the same bandwidth. The frequency of the 6th order harmonic component is larger than the bandwidth, hence the harmonic suppression capability is increased at higher speeds. To better evaluate the suppression of the 6th order harmonic component, the amplitude of the corresponding 6th order harmonic component for the results illustrated in figure 4.17 are listed in table 4.3.

	6th amplitude [deg]	
	$\tau_L = 2\,\mathrm{Nm}$	$\tau_L = 6\,\mathrm{Nm}$
PLL 1	0.0388	0.0439
CCSFF 1	0.0027	0.0038
PLL 2	0.0940	0.1008
CCSFF 2	0.0154	0.0177

Table 4.3. Amplitude of the 6th order harmonic component in the position error $\tilde{\theta}_e$ using PLL 1, PLL 2, CCSFF 1, and CCSFF 2 listed in table 4.1 when $\omega_m = 1800\,\mathrm{rpm}$.

From the table it is seen that both the suppression capability of both CCSFFs is improved compared to when the PMSM is run at 360 rpm in table 4.2. Both CCSFFs suppress the 6th order harmonic component significantly compared to when only a PLL with similar bandwidth is used. As the speed of the PMSM is increased, the frequency of the corresponding 6th order harmonic component is also increased. This means that the CCSFFs will be capable of better attenuating the 6th order harmonic component due to the structure of the CCSFF.

The tests of the two CCSFFs and PLLs show that the design of the CCSFF has a significant impact on the performance. To achieve sufficient harmonic suppression capability in a wide speed range, the bandwidth of the CCSFF-PLL system must be designed to be lower than the least 6th order harmonic component within the speed range. However, a low bandwidth of the CCSFF-PLL system introduces undesired phase delays in the position and speed estimation, which affects the dynamic performance. Thus, it is desired to examine the possibilities of improving the transient response of the CCSFF 1.

The transient response may be improved by adopting an adaptive approach to the parameter design. ω_c is made adaptive using (4.29) [Wang et al., 2017].

$$\omega_c = c \cdot |\hat{\omega}_e - \omega_e^*| + \omega_{c0} \tag{4.29}$$

where c is a constant and ω_{c0} is an initial value for the bandwidth. When a speed transient occurs e.g. due to a load change, the estimated speed differs from the reference speed. As the difference increases, ω_c will increase as well hence the bandwidth of the CCSFF-PLL system increases and improve the transient response. It is seen from (4.29) that ω_c is only affected when a speed difference occurs, hence the adaptive approach does not affect the harmonic suppression capability at steady state. The adaptive ω_c is implemented in the control system in the laboratory using the parameters listed in table 4.4.

Position estimator	c	ω_{c0} [rad/s]
ACCSFF 1	1	250
ACCSFF 2	10	250
ACCSFF 3	25	250

Table 4.4. Adaptive CCSFF-PLL parameters.

Figure 4.18 illustrates the estimated rotor speed and the position error for the test using the CCSFF 1 parameters from table 4.1 and tests with the adaptive method with the

ACCSFF 1, 2, and 3 from table 4.4. The tests are performed with sensorless control with a speed reference at 360 rpm with 2 Nm load applied using the load motor. During the tests, a step load is applied increasing the load from 2 Nm to 6 Nm and from 6 Nm to 2 Nm to examine the dynamic response of the system. The adaptive CCSFFs are also tested when the PMSM is run at 1800 rpm, which is illustrated in figure 4.19.
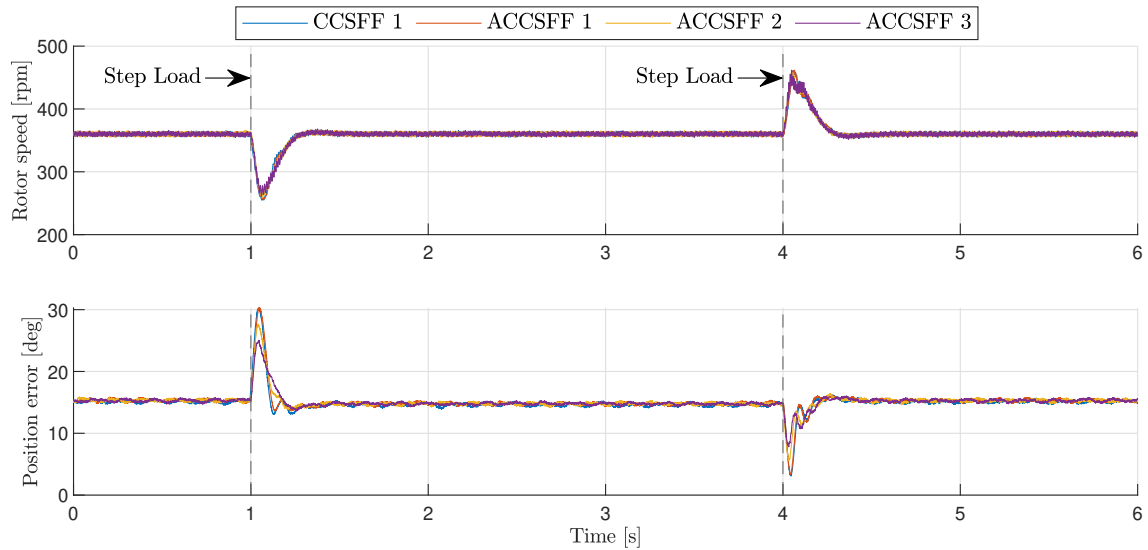

Figure 4.18. Estiamted rotor speed and position error for tests using the CCSFF 1 from table 4.1 and ACCSFF 1, ACCSFF 2, and ACCSFF 3 listed in table 4.4
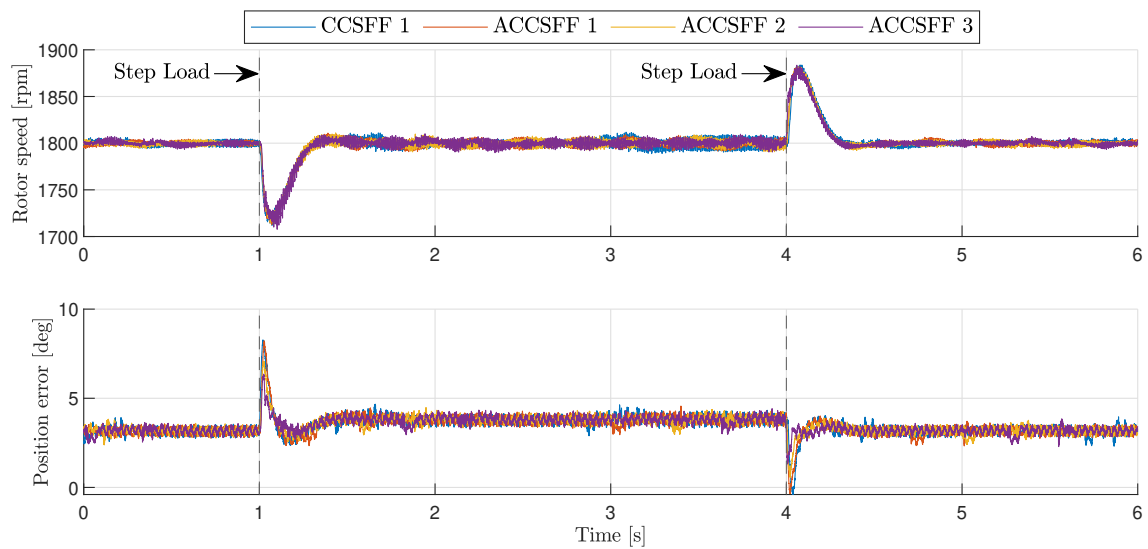
Figure 4.19. Estiamted rotor speed and position error for tests using the the CCSFF 1 from table 4.1 and ACCSFF 1, ACCSFF 2, and ACCSFF 3 listed in table 4.4

It is seen that using the adaptive method for the CCSFF parameters, the transient response is improved significantly. This is the case for both the tests at 360 rpm and 1800 rpm. c influences the improvement in the transient response. Choosing $c = 1$, the reduction in the peak position error compared to using the CCSFF 1 is very small. The bandwidth is not increased sufficiently to improve the transient response. Increasing c to $c = 10$, the

transient response is improved, and the delay in the estimation is decreased. Increasing c further to $c = 25$, it is seen that the delay in the estimation is further reduced, as the peak position error and speed are lowered. This is valid for when the PMSM is run at 360 rpm and 1800 rpm. At steady state, the responses seem similar as expected. This is seen further in figure 4.20 which illustrates the position error along with the harmonic amplitudes obtained from FFT analysis at steady state when the PMSM is run at 360 rpm. Figure 4.20(a) is based on the data before the step load is applied at time $0 \geq t \leq 1$ and figure 4.20(b) is based on the data at time $2 \geq t \leq 3$.
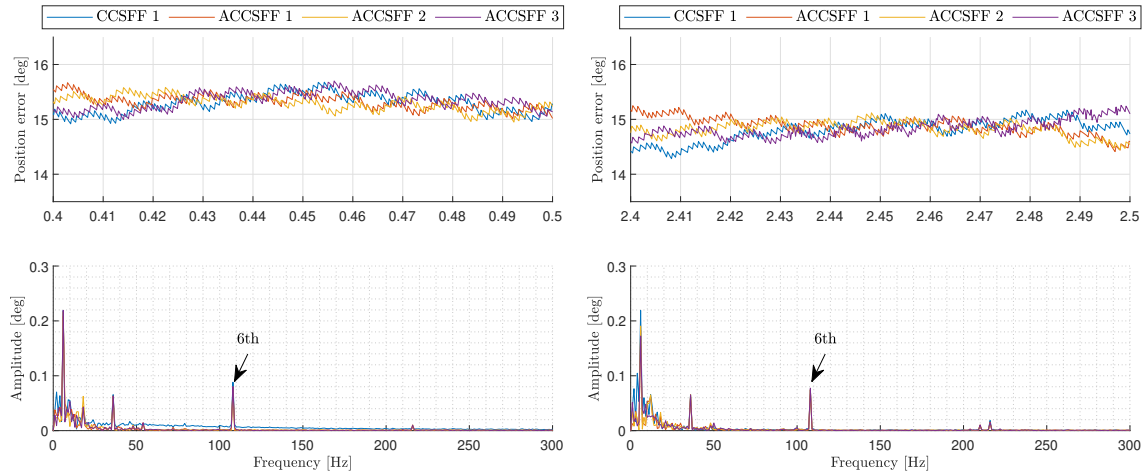
(a) 2 Nm load at time $0 \geq t \leq 1$ from figure 4.18.

(b) 6 Nm load at time $2 \geq t \leq 3$ from figure 4.18.

Figure 4.20. Position error and harmonic amplitude obtained from FFT analysis for tests using the PLL 1, CCSFF 1, PLL 2, and CCSFF 2 listed in table 4.1. FFT analysis is performed at steady state speed.

It is seen, that the position error for all tests seems similar and the same frequency fluctuations occur. From the frequency spectrum, it is further seen that the amplitudes of the different frequency components are similar for the tests. Hence, the adaptive method does not affect the harmonic suppression capability of the CCSFF.

The adaptive CCSFF method is further examined by accelerating the PMSM from 900 rpm to 1800 rpm, which is illustrated in figure 4.21. The estimated rotor speed and the position error are illustrated for the experimental tests.
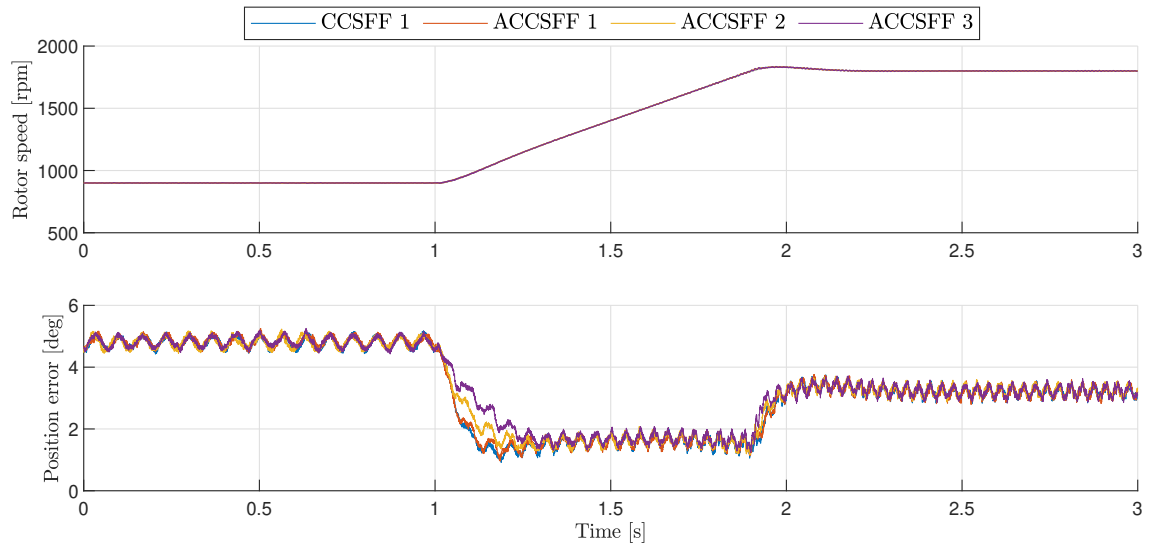
Figure 4.21. Estiamted rotor speed and position error for tests using the CCSFF 1 from table 4.1 and ACCSFF 1, ACCSFF 2, and ACCSFF 3 listed in table 4.4 when the PMSM is accelerated.

It is seen that when the PMSM starts to accelerate, the estimated speed seems similar for all tests. Further, it is seen that the response of the position error as the PMSM starts to accelerate is affected by c. As c is increased the change in the position error is decreased. However, for all tests the position error drops to approximately 1.5 deg before the reference speed 1800 rpm is reached. Thus, from the position error it is seen that the adaptive CCSFF only introduces a small improvement to the transient response when the PMSM is accelerated.

Bilinear Recursive Least Square adaptive filter 5

In this chapter, the bilinear recursive least square (BRLS) adaptive filter from Wu et al. [2020] is presented to filter out the (6 ± 1)th order harmonic component in the estimated flux to suppress the 6th order component in the estimated position and speed. Firstly the structure of the BRLS adaptive filter is presented along with the parameters influence on its filtering capability. Secondly, the harmonic suppression capability along with the effects of the filter parameter design is evaluated experimentally using the laboratory setup. Lastly, the dynamic performance of the control system with the presented BRLS adaptive filter implemented is analyzed. The performance with the filter is compared to the performance without a filter.

5.1 Filter structure

This section presents a bilinear recursive least square (BRLS) adaptive filter for suppression of the (6 ± 1)th order harmonic components in the estimated active flux. According to Wu et al. [2020], the presented filter adaptively tracks the harmonic components by online updating the filter coefficients utilizing the BRLS algorithm. The distorted input signal to the BRLS adaptive filter is then filtered to suppress the desired harmonic components to obtain the fundamental of the active flux and reduce the oscillation in the estimated position and speed.

The filter is implemented such that the active flux $\boldsymbol{z}_{\alpha\beta}$ is filtered through the BRLS adaptive filter before it is used in the PLL to obtain the estimated position and speed as it is illustrated in figure 5.1.
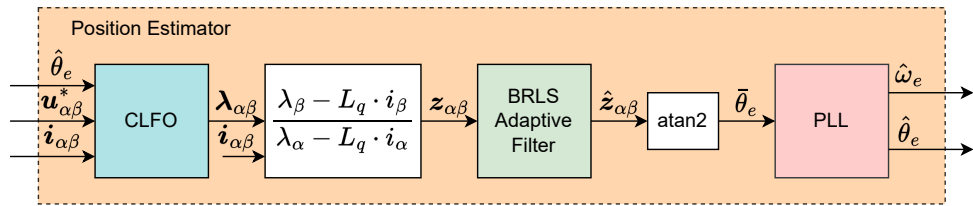

Figure 5.1. Block diagram of the CLFO-BRLS-PLL-based position estimation system.

The BRLS adaptive filter is used to detect and suppress the dominant (6 ± 1)th order harmonic components in the estimated active flux $z_{\alpha\beta}$. Hence, the BRLS adaptive filter is constructed as illustrated in figure 5.2.
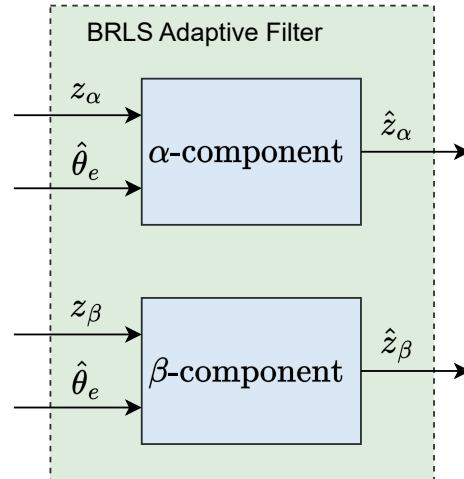
Figure 5.2. Block diagram of the BRLS adaptive filter.

In the following, the suppression of the (6 ± 1)th order harmonic components in the α-component of the active flux is used as an example to explain and elaborate further on the principles of the BRLS adaptive filter. The structure of the BRLS adaptive filter for the α-component is illustrated in figure 5.3.
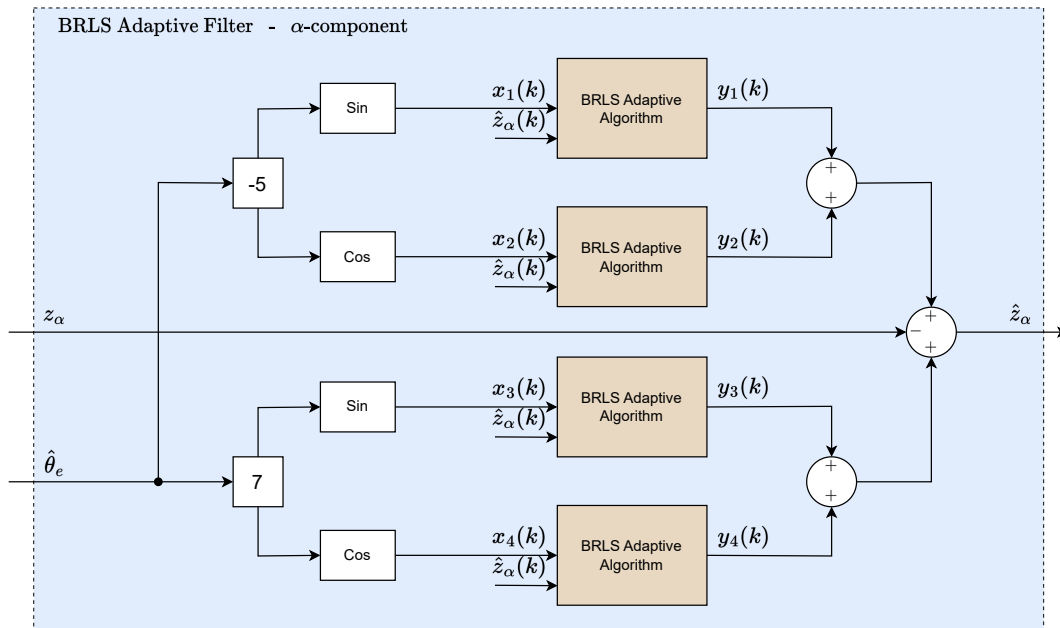

Figure 5.3. Block diagram of the BRLS adaptive filter for the α-component.

It is seen that the BRLS adaptive algorithm is used to estimate the (6 ± 1)th order harmonic components. The estimate of the harmonic components is then subtracted from the distorted estimate of the active flux z_α, which will output the filtered active flux $\hat{z}_\alpha$ used as input to the PLL. Figure 5.4 illustrates the BRLS adaptive algorithm.
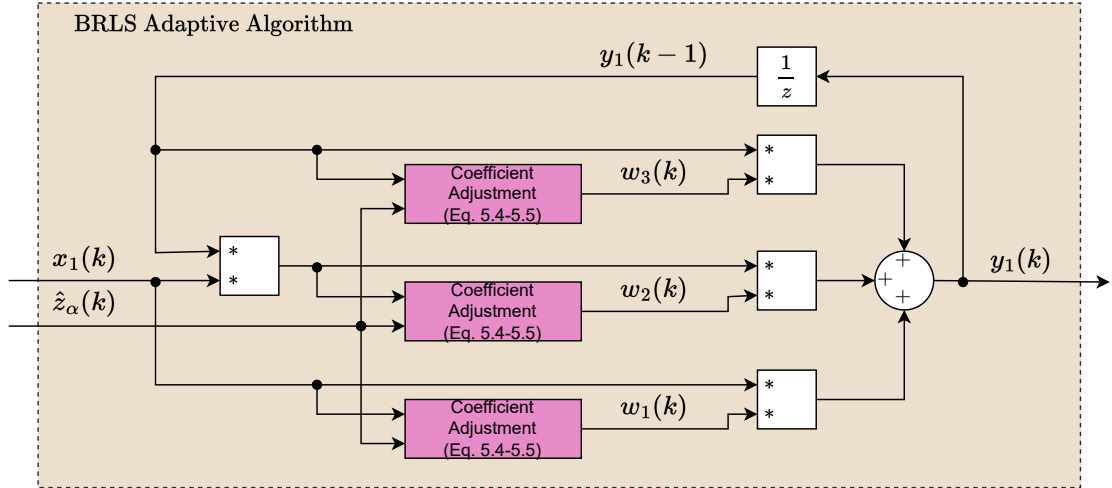
Figure 5.4. Block diagram of the BRLS adaptive algorithm.

The BRLS adaptive algorithm is used to update the filter coefficients based on the specific harmonic component reconstructed from the estimated position and the output of the BRLS adaptive filter $\hat{z}_\alpha$. This allows the adaptive filter, based on the BRLS adaptive algorithm, to detect the specified harmonic component which is present in the estimated active flux.

The input signal $x_n(k)$ is a sine or cosine function of the (6 ± 1)th order of the estimated position $\hat{\theta}_e$ corresponding to $\cos(\pm(6 \pm 1) \cdot \hat{\theta}_e)$ and $\sin(\pm(6 \pm 1) \cdot \hat{\theta}_e)$. The input signal along with the output signal $y_n(k)$ are used in the harmonic information vector $\phi(k)$. The output signal is introduced to the information vector to enhance the harmonic suppression capability of the BRLS adaptive filter. The harmonic information vector is given as (5.1) [Wu et al., 2020].

$$\phi(k) = [x(k) \; y(k-1) \; x(k) \cdot y(k-1)]^T \tag{5.1}$$

The output signal $y(k)$ is formed as the dot product of the harmonic information vector $\phi(k)$ and the filter coefficient vector $w(k)$. As the BRLS adaptive filter converges, the output signal $y(k)$ corresponds to the specified harmonic component of the distorted original signal. Thus, the output signal $y(k)$ is calculated as (5.2) [Wu et al., 2020].

$$y(k) = \phi^T(k) \cdot w(k) \tag{5.2}$$

The output of the BRLS adaptive filter $\hat{z}_\alpha$ is the error term between the distorted active flux z_α and the sum of the outputs from the BRLS adaptive algorithm, which is expressed as in (5.3). Ideally, the output $\hat{z}_\alpha$ will appear as the fundamental component of the distorted active flux z_α.

$$\hat{z}_{\alpha\beta} = z_{\alpha\beta} - \sum_{n=1}^{4} y_n(k) \tag{5.3}$$

The filter coefficients are updated continuously based on the harmonic characteristics in the estimated active flux, which makes it possible for the BRLS adaptive filter to detect

and suppress the (6 ± 1)th order harmonic components. The coefficients are updated using the expression in (5.4) [Wu et al., 2020].

$$\boldsymbol{w}(k+1) = \boldsymbol{w}(k) + S_D(k+1) \cdot \boldsymbol{\phi}(k) \cdot \hat{z}_{\alpha\beta} \tag{5.4}$$

Where $S_D(k)$ is given as (5.5) [Wu et al., 2020].

$$S_D(k+1) = \frac{1}{\lambda} \cdot \left(S_D(k) - \frac{S_D(k) \cdot \boldsymbol{\phi}^T(k) \cdot \boldsymbol{\phi}(k) \cdot S_D(k)}{\lambda + \boldsymbol{\phi}^T(k) \cdot S_D(k) \cdot \boldsymbol{\phi}(k)} \right) \tag{5.5}$$

Where λ is the forgetting factor, which is usually set as a positive constant with a value close to 1 i.e. $0 << \lambda < 1$ [Wu et al., 2020].
λ is used to increase the weight on the current information vector $\boldsymbol{\phi}(k)$, which results in the output signal $y(k)$ being able to detect the harmonic components adaptively. λ directly affects the convergence speed and the harmonic suppression capability. If the value of λ is large, the speed of the filter coefficient update and convergence will be slow. However, good harmonic detection and low misadjustment of the coefficients are obtained. For a smaller value of λ, the filter coefficients and the convergence speed is increased. However, the harmonic detection accuracy is worsened and the misadjustment of the filter coefficients is increased. [Wu et al., 2020]

When implemented in the control system of the laboratory setup, $S_D(k)$ and $\boldsymbol{w}(k)$ need to be initialized. $S_D(k)$ and $\boldsymbol{w}(k)$ are initialized as (5.6).

$$\boldsymbol{w}(k) = 0$$
$$S_D(k) = \sigma \tag{5.6}$$

Where σ is the initial value of $S_D(k)$. According to Wu et al. [2020] the selection of σ can be chosen based on the harmonic distortion level in the estimated active flux.

To analyze more on the influence of λ and σ, the BRLS adaptive filter is tested with the system illustrated in figure 5.1. For simplicity, the CLFO is disregarded, and a distorted waveform containing (6 ± 1)th order harmonic components is used as input to the BRLS adaptive filter. The magnitude of the fundamental, 5th and 7th order harmonic components used in the tests are $Z = 1$, $Z_{5th} = 0.2$, and $Z_{7th} = 0.1$, respectively. Firstly, the influence of λ is analyzed by testing the BRLS adaptive filter for different values of λ while $\sigma = 0.001$. The tests are performed with $\omega_m = 900$ rpm. Figure 5.5 illustrates the results obtained from the tests using different values for λ. For convenience, only the α-component is shown.
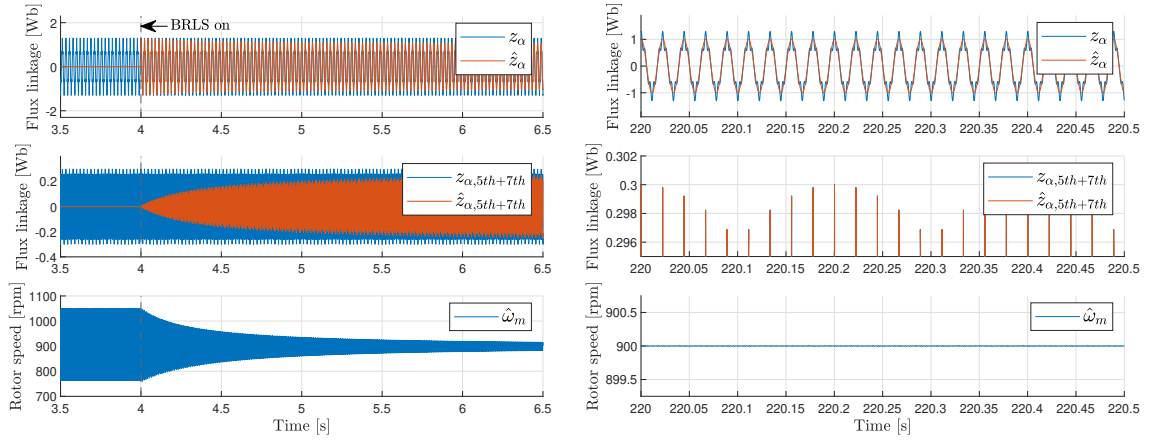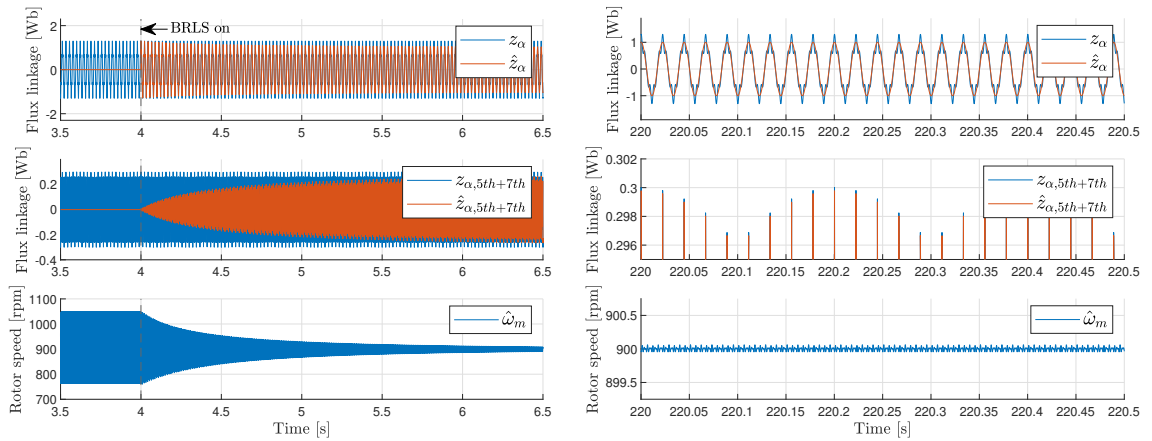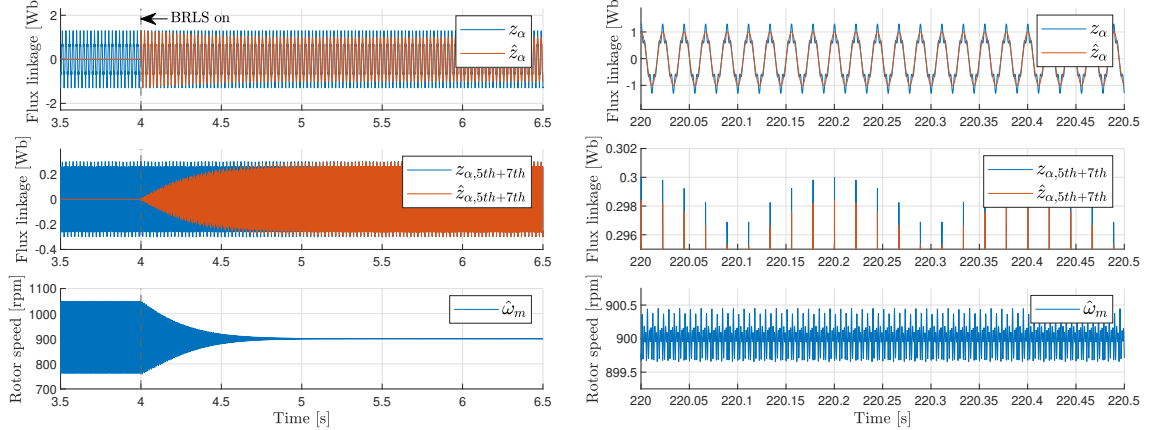
(a) Enable the BRLS adaptive filter using $\lambda = 0.99999$.

(b) Steady state condition using $\lambda = 0.99999$.

(c) Enable the BRLS adaptive filter using $\lambda = 0.9999$.

(d) Steady state condition using $\lambda = 0.9999$.

(e) Enable the BRLS adaptive filter using $\lambda = 0.999$.

(f) Steady state condition using $\lambda = 0.999$.

Figure 5.5. Illustration of the estimated rotor speed $\hat{\omega}_m$, input z_α and output $\hat{z}_\alpha$ of the BRLS adaptive filter, and the real (6 ± 1)th order harmonic component and the (6 ± 1)th order harmonic component estimated by the BRLS adaptive algorithm. The tests are performed when $\omega_m = 900\,\mathrm{rpm}$ and $\sigma = 0.001$.

Generally for all tests it is seen, that when the BRLS adaptive filter is enabled, the (6 ± 1)th order harmonic component $\hat{z}_{\alpha,5th+7th}$ starts to converge. As the (6 ± 1)th order harmonic components converges, the output of the BRLS adaptive filter $\hat{z}_\alpha$ begins to take the form of the fundamental component of the input z_α, as the estimated (6 ± 1)th order harmonic components are subtracted from the original distorted signal z_α. As the output of the BRLS adaptive filter $\hat{z}_\alpha$ becomes more sinusoidal due to the compensation of the (6 ± 1)th order harmonic components, the oscillations in the rotor speed $\hat{\omega}_m$ are reduced and a more smooth speed estimation is obtained.

Comparing figures 5.5(a), 5.5(c), and 5.5(e) it is seen that the selection of λ has an influence on the converging speed. This is seen both from the estimates speed and the estimate of the (6 ± 1)th order harmonic component $\hat{z}_{\alpha,5th+7th}$. When $\lambda=0.99999$ the speed ripples are reduced to the level illustrated in figure 5.5(b) when the BRLS adaptive filter has been enabled for approximately $210\,\mathrm{s}$. Choosing $\lambda=0.9999$, the speed ripples are reduced to the level seen in figure 5.5(d) when the BRLS adaptive filter has been enabled for approximately $21\,\mathrm{s}$. The speed ripples illustrated in figure 5.5(f) are obtained with the BRLS adaptive filter being enabled for approximately $2.1\,\mathrm{s}$. Thus, the convergence speed is changed with a factor of 10 when λ is changed the same. Hence, choosing λ close to one i.e. $\lambda=0.99999$ will increase the convergence speed significantly.

However, comparing figures 5.5(b), 5.5(d), and 5.5(f) it is seen that selecting λ close to one i.e. $\lambda=0.99999$ the harmonic suppression capability is improved. This is seen both from the estimate of the (6 ± 1)th order harmonic component $\hat{z}_{\alpha,5th+7th}$ and the estimated speed. It is seen in figure 5.5(f) that choosing $\lambda=0.999$ affects $\hat{z}_{\alpha,5th+7th}$ as it deviates more from the real value of the (6 ± 1)th order harmonic component $z_{\alpha,5th+7th}$. The $(6\pm1)$the order harmonic distortion is not ideally compensated, meaning the 6th order harmonic component in the estimated position and speed is not reduced sufficiently. As the value for λ is increased i.e. $\lambda=0.9999$ and $\lambda=0.99999$ seen in figures 5.5(b), and 5.5(d) the estimate of $\hat{z}_{\alpha,5th+7th}$ is improved. This reduces the magnitude of the 6th order harmonic component in the estimated position and speed, hence the ripples in the estimated speed seen in figures 5.5(b), and 5.5(d) are smaller compared to figure 5.5(f).

The tests performed with different values of λ show, that choosing a large value i.e. $\lambda=0.99999$ increases the converge speed. However, the harmonic suppression capability is improved due to less misadjustment of the filter coefficients, hence the estimation of the specific harmonic components is more accurate. Choosing a smaller value of λ i.e. $\lambda=0.999$ will improve the converge speed significantly. However, this will increase the misadjustment of the filter coefficient, leading to a worse estimation of the specific harmonic components. This affects the harmonic suppression capability which will be worsened, leading to larger ripples in the estimated speed. Hence, the selection of λ is a trade-off between fast converge speed and good harmonic suppression capability. The value of λ is determined based on experimental tests using the laboratory setup, which is elaborated in section 5.2.

With the influence of λ examined, the influence of σ is analyzed. Tests are performed with $\lambda=0.9999$ with different values for σ. The tests are performed when $\omega_m=900\,\mathrm{rpm}$. Figure 5.6 illustrates the results obtained from the tests using different values for σ. For convenience, only the α-component is shown.
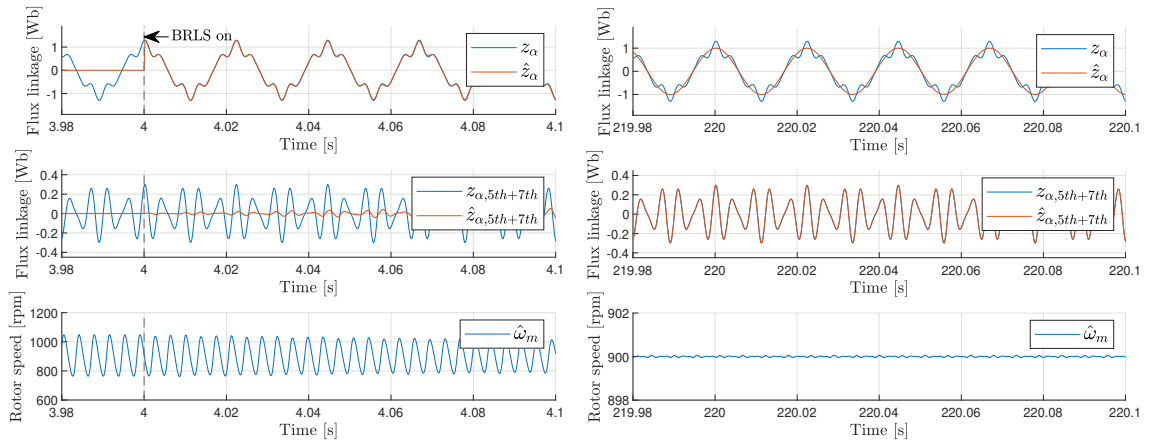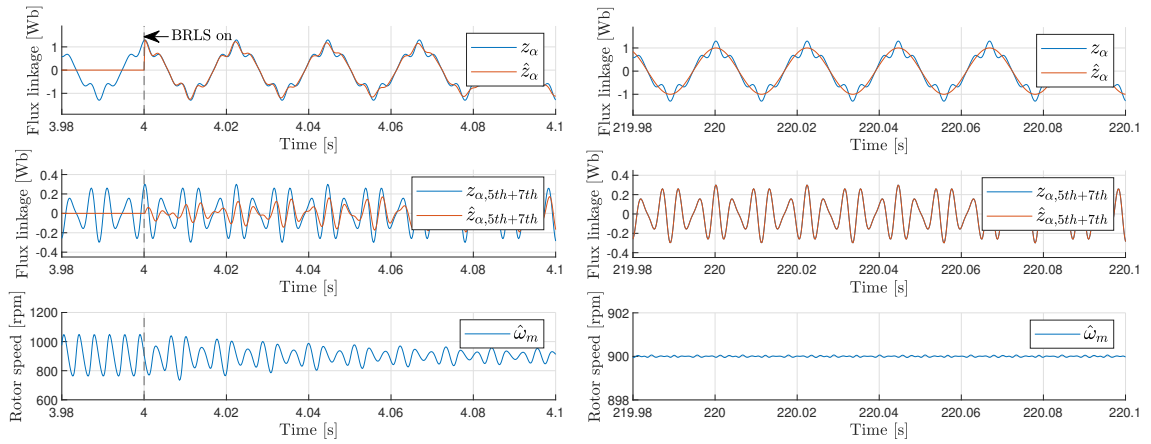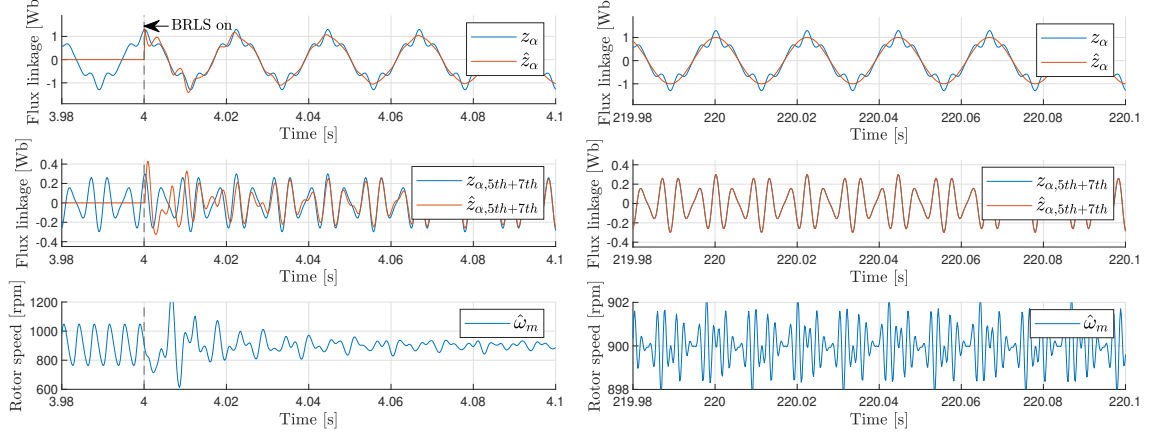
(a) Enable the BRLS adaptive filter using $\sigma = 0.001$.

(b) Steady state condition using $\sigma = 0.001$.

(c) Enable the BRLS adaptive filter using $\sigma = 0.01$.

(d) Steady state condition using $\sigma = 0.01$.

(e) Enable the BRLS adaptive filter using $\sigma = 0.1$.

(f) Steady state condition using $\sigma = 0.1$.

Figure 5.6. Illustration of the estimated rotor speed ω_m, the input z_α and output $\hat{z}_\alpha$ of the BRLS adaptive filter, and the real (6 ± 1)th order harmonic component and the (6 ± 1)th order harmonic component estimated by the BRLS adaptive algorithm. The tests are performed when $\omega_m = 900$ rpm and $\lambda = 0.9999$.

Figure 5.6(a) illustrates the results when $\sigma = 0.001$. It is seen, that when the BRLS adaptive filter is enabled, the BRLS algorithm starts to estimate the (6 ± 1)th harmonic components of the distorted input signal. The estimation of the (6 ± 1)th order harmonic component $\hat{z}_{\alpha,5th+7th}$ slowly increases, hence only small changes are seen in the output of the BRLS adaptive filter $\hat{z}_\alpha$ compared to the input signal z_α. Eventually, the BRLS adaptive filter is capable of tracking the specific harmonic component more accurately, as the filter coefficients converge. This is seen in figure 5.6(b), as $\hat{z}_\alpha$ appears more sinusoidal, and the (6 ± 1)th order harmonic component estimated by the BRLS algorithm seems to track the real (6 ± 1)th order harmonic component.

Figure 5.6(c) illustrates the results when $\sigma = 0.01$. It is seen, that when the BRLS adaptive filter is enabled, the initial value of the BRLS algorithm estimate of the (6 ± 1)th harmonic components is larger compared to when $\sigma = 0.001$. Hence, the estimation of the (6 ± 1)th order harmonic component $\hat{z}_{\alpha,5th+7th}$ increases faster. In figure 5.6(d) it is seen, that the output active flux of the BRLS adaptive filter $\hat{z}_\alpha$ appears more sinusoidal and the (6 ± 1)th order harmonic component estimated by the BRLS algorithm seems to track the real (6 ± 1)th order harmonic component. The fluctuation in the estimated speed as the BRLS adaptive filter converge seems similar compared to when $\sigma = 0.001$ as seen in figure 5.6(b).

Figure 5.6(e) illustrates the results when $\sigma = 0.1$. It is seen, that when the BRLS adaptive filter is enabled, the initial value of the BRLS algorithm estimate of the (6 ± 1)th harmonic components is larger compared to when $\sigma = 0.01$. It is further seen, that the estimate of the (6 ± 1)th harmonic components is larger than the real value after the first estimates. This affects the magnitude of the speed ripple, as it becomes larger than before the BRLS adaptive filter is enabled where after the ripple magnitude of the estimated speed decreases. This is due to the initial estimation of the (6 ± 1)th harmonic component. The BRLS algorithm compensates too aggressively on the (6 ± 1)th harmonic component. In figure 5.6(f) it is seen, that $\hat{z}_\alpha$ appears more sinusoidal, and the (6 ± 1)th order harmonic component estimated by the BRLS algorithm seems to track the real (6 ± 1)th order harmonic component. However, the fluctuation in the estimated speed does not reduce to the same extent as seen in figure 5.6(b) and 5.6(d). It seems that the overcompensation of the (6 ± 1)th harmonic component as the BRLS adaptive filter is enabled affects the harmonic suppression capability.

From figure 5.6 it is seen, that the selection of σ has an influence on the converging speed and the harmonic suppression. It is further seen from the figure, that the first estimate of the (6 ± 1)th order harmonic component $\hat{z}_{\alpha,5th+7th}$, after the BRLS adaptive filter is enabled, is dependent on the selection of σ. σ is the initial value of $S_D(k)$ as given in (5.6). Thus, the first estimate of the (6 ± 1)th order harmonic component is affected by the value of σ. According to Wu et al. [2020] the selection of σ can be chosen based on the harmonic distortion level in the estimated active flux. For a larger distortion level, a higher value of σ can be selected. Conversely, a smaller value of σ can be selected for a smaller distortion level. The distorted signal z_α used for parameter analysis has magnitudes of 0.2 and 0.1 for the 5th and 7th order harmonic component, respectively. Using $\sigma = 0.1$ seems to be too large as seen in figure 5.6. However, this value corresponds to the magnitude of the 7th order harmonic component in the distorted signal fed to the BRLS adaptive filter.

Hence, the initial value for $S_D(k)$ may be too large, and the BRLS adaptive filter is too aggressive when enabled. $\sigma = 0.01$ seems to give better performance, hence it is deemed to be desirable to select the value for σ based on the distortion level of the active flux i.e. the magnitude of the (6 ± 1)th order harmonic components.

The signal used for analyzing the influence of the parameter design of the BRLS adaptive filter is chosen large for a better opportunity to distinguish between the unfiltered and filtered active flux. When the BRLS adaptive filter is implemented and elaborated further with the laboratory setup, a proper selection of σ is elaborated based on the distortion level of the estimated active flux. Based on the analysis of the measured signal elaborated in chapter 3 it is expected that the selection of σ is less than $\sigma = 0.01$ based on the FFT analysis of the estimated active flux seen in figure 3.3.

5.2 Harmonic suppression capability

As described in section 5.1 and illustrated in figures 5.5 and 5.6, the selection of the BRLS algorithm parameters λ and σ affects the performance of the BRLS adaptive filter. Thus, different tests are performed with the laboratory setup to select the proper values for λ and σ before further examination of the BRLS adaptive filter is performed. Figure 5.7 illustrates the input active flux to the BRLS adaptive filter z_α, the output active flux $\hat{z}_\alpha$, the estimated (6 ± 1)th order harmonic component $\hat{z}_{\alpha,5th+7th}$ from the BRLS adaptive filter and the estimated rotor speed $\hat{\omega}_m$ for performed tests with a different selection of λ. For convenience, only the α-component is shown. The tests are performed with the PMSM run with sensorless FOC at 360 rpm and 1800 rpm. σ is selected as 0.001 and the PLL 2 listed in table 4.1 is used in the position estimator.
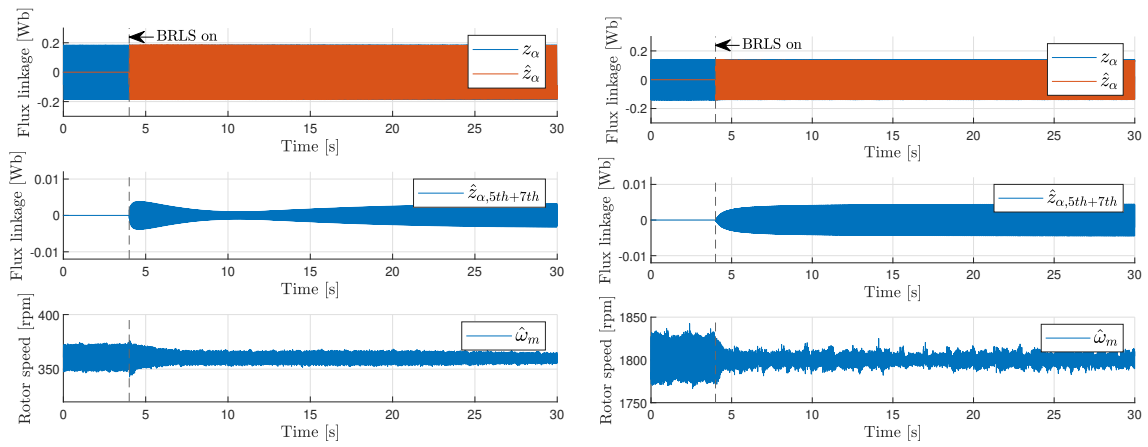
(a) PMSM run at 360 rpm using $\lambda = 0.99999$.   **(b)** PMSM run at 1800 rpm using $\lambda = 0.99999$.
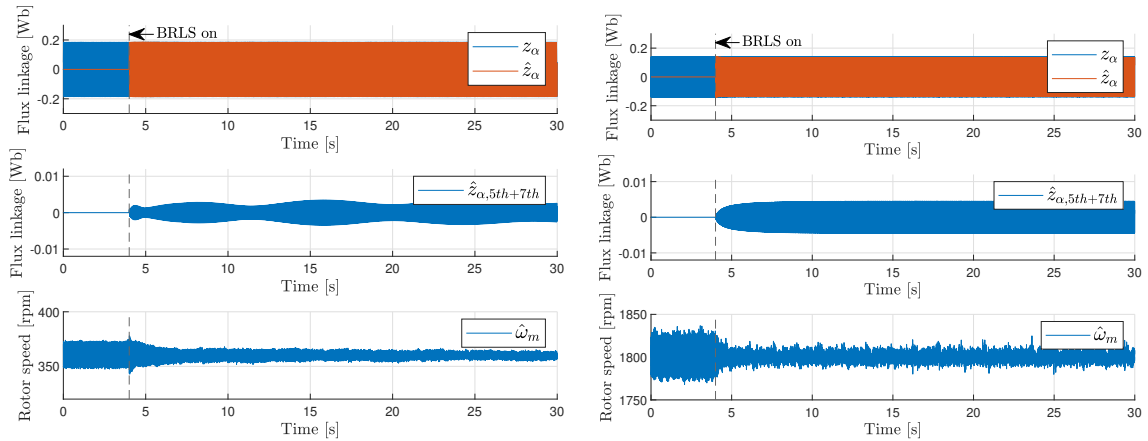
(c) PMSM run at 360 rpm using $\lambda = 0.9999$.   **(d)** PMSM run at 1800 rpm using $\lambda = 0.9999$.
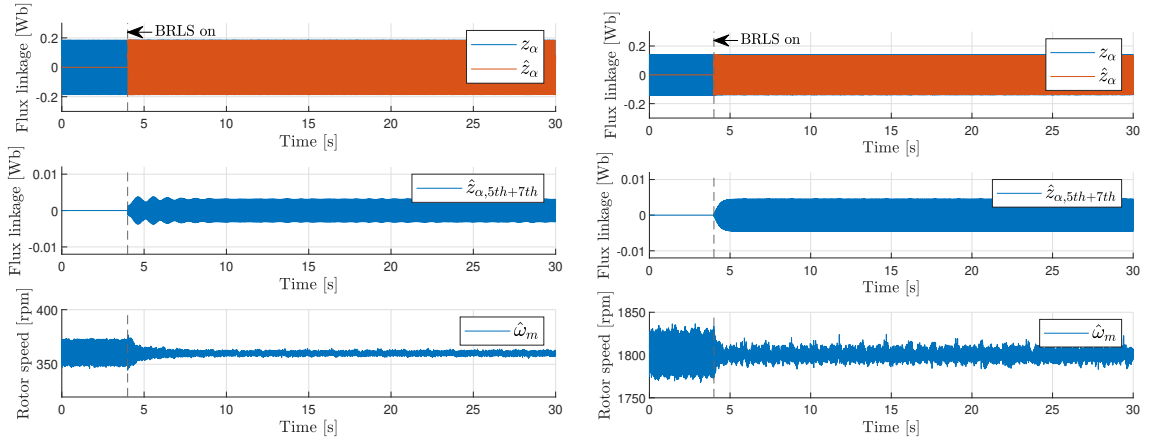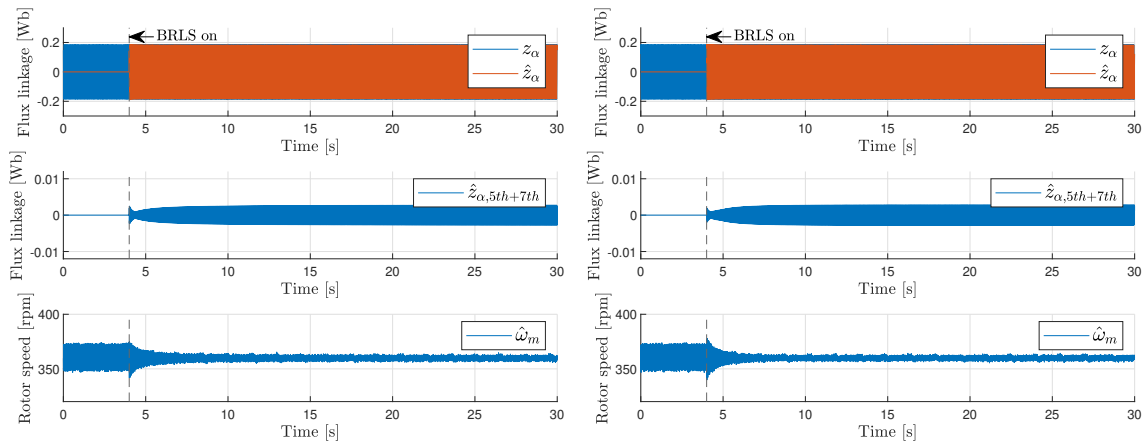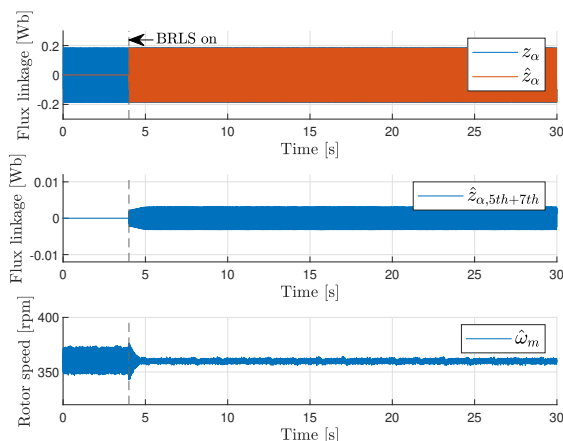
(e) PMSM run at $360\,\mathrm{rpm}$ using $\lambda = 0.999$.   **(f)** PMSM run at $1800\,\mathrm{rpm}$ using $\lambda = 0.999$.

Figure 5.7. Illustration of the estimated rotor speed $\hat{z}\omega_m$, the input z_α and output $\hat{z}_\alpha$ of the BRLS adaptive filter, and the (6 ± 1)th order harmonic component estimated by the BRLS adaptive algorithm. The tests are performed with sensorless FOC using PLL 2 and $\sigma = 0.001$.

Comparing the results seen in figures 5.7(a), 5.7(c), and 5.7(e) when the PMSM is run at $360\,\mathrm{rpm}$ it is seen, that the selection of λ has a big impact on the estimate of the (6 ± 1)th order harmonic component $\hat{z}_{\alpha,5th+7th}$. From figure 5.7(a) it is seen, that when the BRLS adaptive filter is enabled, $\hat{z}_{\alpha,5th+7th}$ begins to increase. At $t \approx 4.5\,\mathrm{s}$ $\hat{z}_{\alpha,5th+7th}$ begins to decrease until $t \approx 10\,\mathrm{s}$ whereafter $\hat{z}_{\alpha,5th+7th}$ increases before it converge at $t \approx 30\,\mathrm{s}$. From the estimated speed it is seen, that when the BRLS adaptive filter is enabled, a larger speed ripple is seen before the speed ripple decrease in magnitude. The magnitude of the speed ripples decreases as $\hat{z}_{\alpha,5th+7th}$ converges.

The same tendencies are seen in figure 5.7(c) when $\lambda = 0.9999$. $\hat{z}_{\alpha,5th+7th}$ is seen to be more oscillating towards convergence. However, it is seen that the magnitude of the speed ripple is reduced more at time $t = 30\,\mathrm{s}$ compared to figure 5.7(a) when $\lambda = 0.99999$. This indicates, that the converge speed is increased using the less value of λ.

In figure 5.7(e) it is seen, that $\hat{z}_{\alpha,5th+7th}$ is much faster to converge. It is seen, that it has the same tendencies as seen in 5.7(c), as $\hat{z}_{\alpha,5th+7th}$ is more oscillating as it converges. However, it converges much faster compared to choosing a higher value of λ. This is also seen in the estimated speed, as the magnitude of the speed ripples decreases faster to the level seen in figures 5.7(a) and 5.7(c). Furthermore, it is seen that using $\lambda = 0.999$, the magnitude of the speed ripple is less compared to the other tests at time $t = 30\,\mathrm{s}$.

Comparing the results seen in figures 5.7(b), 5.7(d), and 5.7(f) when the PMSM is run at $1800\,\mathrm{rpm}$ it is seen, that the selection of λ does not have the same impact on the estimate of the (6 ± 1)th order harmonic component $\hat{z}_{\alpha,5th+7th}$. However, it is seen that a higher value of λ increases the time for $\hat{z}_{\alpha,5th+7th}$ to converge to the same level. Both from the estimate of the (6 ± 1)th order harmonic component $\hat{z}_{\alpha,5th+7th}$ and the estimated rotor speed $\hat{\omega}_m$ it is seen that the magnitudes after the BRLS adaptive filter has converged are similar regardless of the selection of λ.

The oscillation in the estimate of the (6 ± 1)th order harmonic component $\hat{z}_{\alpha,5th+7th}$ as it converges when the PMSM is run at $360\,\mathrm{rpm}$ is observed to be affected by the position

feedback used in the BRLS adaptive filter to reconstruct the (6 ± 1)th order harmonic components. Figure 5.8 illustrates the input active flux to the BRLS adaptive filter z_α, the output active flux $\hat{z}_\alpha$, the estimated (6 ± 1)th order harmonic component $\hat{z}_{\alpha,5th+7th}$ from the BRLS adaptive filter and the estimated rotor speed $\hat{\omega}_m$ for performed tests with a different selection of λ when the encoder rotor position signal is used in the BRLS adaptive filter.

(a) PMSM run at 360 rpm using $\lambda = 0.99999$. (b) PMSM run at 360 rpm using $\lambda = 0.9999$.
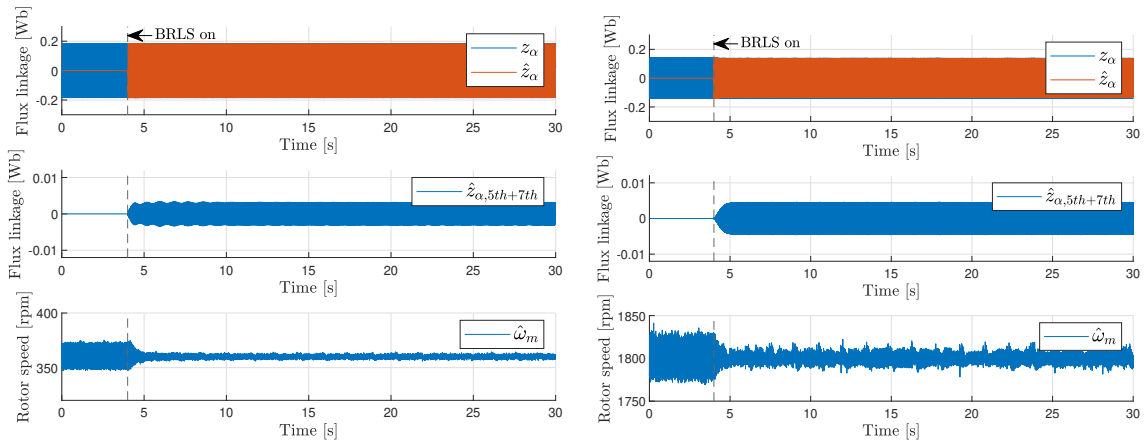

(c) PMSM run at 360 rpm using $\lambda = 0.999$.

Figure 5.8. Illustration of the estimated rotor speed $\hat{z}\omega_m$, the input z_α and output $\hat{z}_\alpha$ of the BRLS adaptive filter, and the (6 ± 1)th order harmonic component estimated by the BRLS adaptive algorithm. The tests are performed with sensorless FOC using PLL 2 and $\sigma = 0.001$. The encoder position is used as feedback in the BRLS for reconstruction of (6 ± 1)th order harmonic components.

It is seen from figure 5.8, that the position feedback used in the BRLS adaptive filter to reconstruct the (6 ± 1)th order harmonic component has an impact on $\hat{z}_{\alpha,5th+7th}$. In figures 5.8(a) and 5.8(b) it is seen, that when the BRLS adaptive filter is enabled, $\hat{z}_{\alpha,5th+7th}$ increases immediately whereafter it decreases a bit before converging. This is also seen when the estimated position is used to reconstruct the (6 ± 1)th order harmonic component illustrated in figure 5.7. However, it is seen that the converging speed is significantly

improved using encoder position feedback in the BRLS algorithm. Furthermore, the oscillation in $\hat{z}_{\alpha,5th+7th}$ as it converges is not that significant. Thus, it is assessed that accurate position estimation is desirable when the PMSM is run at a lower speed range. No further analysis is performed to examine the tendencies of $\hat{z}_{\alpha,5th+7th}$ seen in figure 5.7 when operating the PMSM at 360 rpm and the estimated position is used to reconstruct the (6 ± 1)th order harmonic component. It is seen from figure 5.7 that $\hat{z}_{\alpha,5th+7th}$ converge and the stability is ensured. Thus, it is deemed to be acceptable for further analysis of the BRLS adaptive filter.

Generally, the results seen in figure 5.7 follow the expectations of the influence of the selection of λ. As described in section 5.1, λ is the forgetting factor used to update the coefficients of the BRLS adaptive filter. Using a value of λ close to one i.e. $\lambda = 0.99999$, the correction of the filter coefficients relies more on the past values, hence the converging speed is slower compared to selecting $\lambda = 0.999$. It is observed in the laboratory, that choosing $\lambda < 0.999$ will give some stability issues with the system. Thus, based on the results illustrated in figure 5.7, it is chosen to use $\lambda = 0.999$ for further analysis of the BRLS adaptive filter. This is chosen as this value provides the fastest convergence speed. Furthermore, it does not seem to affect the harmonic suppression capability significantly.

With λ selected, the influence of σ is analyzed. Figure 5.9 illustrates the input active flux to the BRLS adaptive filter z_α, the output active flux $\hat{z}_\alpha$, the estimated (6 ± 1)th order harmonic component $\hat{z}_{\alpha,5th+7th}$ from the BRLS adaptive filter, and the estimated rotor speed $\hat{\omega}_m$ for performed tests with a different selection of σ. For convenience, only the α-component is shown. The tests are performed with the PMSM run with sensorless FOC at 360 rpm and 1800 rpm with 2 Nm load applied. The tests are performed using the PLL 2 listed in table 4.1 in the position estimator.

(a) PMSM run at 360 rpm using $\sigma = 0.0005$.   (b) PMSM run at 1800 rpm using $\sigma = 0.0005$.
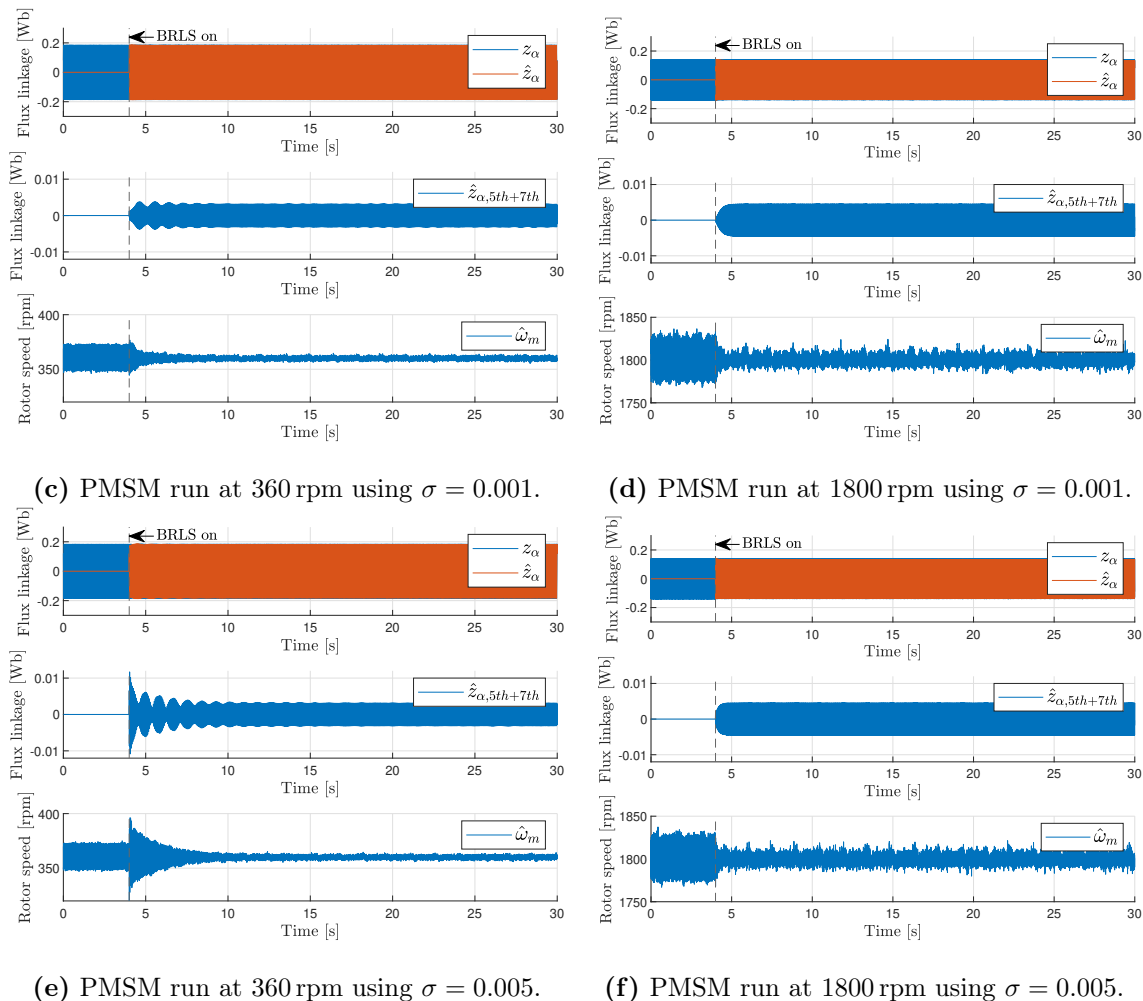
(c) PMSM run at 360 rpm using $\sigma = 0.001$.

(d) PMSM run at 1800 rpm using $\sigma = 0.001$.

(e) PMSM run at 360 rpm using $\sigma = 0.005$.

(f) PMSM run at 1800 rpm using $\sigma = 0.005$.

Figure 5.9. Illustration of the estimated rotor speed $\hat{z}\omega_m$, the input z_α and output $\hat{z}_\alpha$ of the BRLS adaptive filter, and the (6 ± 1)th order harmonic component estimated by the BRLS adaptive algorithm. The tests are performed with sensorless FOC using PLL 2 and $\lambda = 0.999$.

Comparing the results in figures 5.9(a), 5.9(c), and 5.9(e) it is seen, that the selection of σ influences the initial estimate of the (6 ± 1)th order harmonic component $\hat{z}_{\alpha,5th+7th}$. As the value of σ is increased, the initial estimate of $\hat{z}_{\alpha,5th+7th}$ is also seen to be increased. As seen in figure 5.9(e) when $\sigma = 0.005$, the initial estimate of $\hat{z}_{\alpha,5th+7th}$ is much larger than the value when it has converged. This indicates that the initial estimate is too aggressive, meaning the BRLS adaptive filter does not compensate the (6 ± 1)th order distortion accurately. This affects the estimated speed, as the magnitude of the ripples in the speed is seen to be increased when the BRLS adaptive filter is enabled. As $\hat{z}_{\alpha,5th+7th}$ converges, the speed ripples decrease. However, the over-estimation of $\hat{z}_{\alpha,5th+7th}$ at the time when the BRLS adaptive filter is enabled, affects the converging speed. From 5.9(a), 5.9(c), and 5.9(e) it appears as choosing $\sigma = 0.0005$ provides the fastest convergence of $\hat{z}_{\alpha,5th+7th}$. This is also seen in the estimated speed, as the time before reaching minimum ripple magnitude is least choosing this value compared to $\sigma = 0.001$ and $\sigma = 0.005$.

When the PMSM is run at 1800 rpm it seems to be reversed, as seen when comparing figures 5.9(b), 5.9(d), and 5.9(f). It is seen, that the fastest converging speed is obtained

using $\sigma = 0.005$. It is seen from figure 5.9(f), that the estimate of the (6 ± 1)th order harmonic component $\hat{z}_{\alpha,5th+7th}$ does not over-estimate when the BRLS adaptive filter is enabled. $\hat{z}_{\alpha,5th+7th}$ is seen to be smooth and fast towards convergence.

As described in 5.1, the distortion level may affect the selection of σ. Thus, the estimated active flux which is used as input to the BRLS adaptive filter is analyzed to examine the magnitudes of the (6 ± 1)th order harmonic components. Figure 5.10 illustrates the waveform of the estimated active flux along with the frequency spectrum obtained by FFT analysis when the PMSM is run at 360 rpm and 1800 rpm with 2 Nm load is applied.
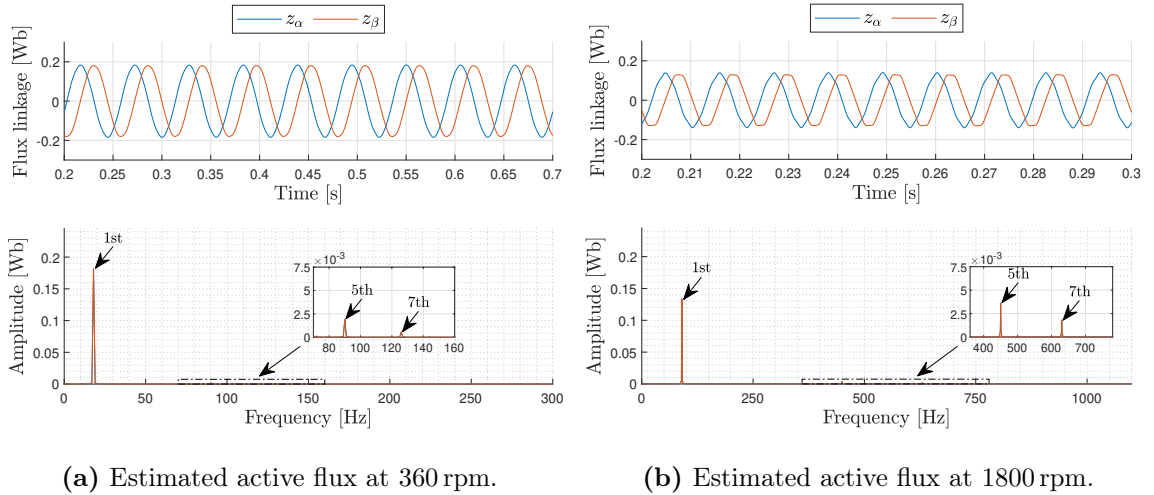

(a) Estimated active flux at 360 rpm.   **(b)** Estimated active flux at 1800 rpm.

Figure 5.10. $\alpha\beta$ active flux and the frequency spectrum of the input to the BRLS adaptive filter. The PMSM is run at 360 rpm and 1800 rpm with 2 Nm load applied.

Comparing the (6 ± 1)th order harmonic components in figures 5.10(a) and 5.10(b) it is seen that the magnitudes are different depending on the operation speed of the PMSM. When the PMSM is run at 360 rpm the magnitudes of the (6 ± 1)th order harmonic components are less compared to when the PMSM is run at 1800 rpm. σ is the initial value of $S_D(k)$ as given in (5.6). Thus, the first estimate of the (6 ± 1)th order harmonic component is affected by the value of σ. If σ is higher than the magnitude of the distortion level, the first estimate of $\hat{z}_{\alpha,5th+7th}$ will be higher than the actual (6 ± 1)th order harmonic components. This is seen in figure 5.9(e) with $\sigma = 0.005$. As seen in figure 5.10(a) the magnitude of the (6 ± 1)th order harmonic components is less than σ. Thus, a relation between the distortion level and σ is seen. When the PMSM is run at 1800 rpm, the magnitude of the (6 ± 1)th order harmonic components are larger, hence a larger value of σ can be selected. This correlates with the results seen in figure 5.9(f), as the first estimate of $\hat{z}_{\alpha,5th+7th}$ is not over-estimated.

Based on the results seen in figure 5.9 and the correlation with the active flux in figure 5.10, it is chosen to select $\sigma = 0.0005$. This is chosen to ensure fast converging speed in the lower speed range and avoid the over-estimate of $\hat{z}_{\alpha,5th+7th}$ when the BRLS adaptive filter is enabled. When the PMSM is operated at 1800 rpm, only a small increase in the converging speed is seen when choosing $\sigma = 0.0005$ compared to either $\sigma = 0.001$ or $\sigma = 0.005$.

As the value for the BRLS adaptive filter parameters λ and σ is selected, the harmonic

suppression capability of the BRLS adaptive filter is further analyzed. The estimated input active flux to the BRLS adaptive filter and the output active flux is examined. The input and output $\alpha\beta$ active flux is illustrated in figure 5.11 along with the frequency spectrum obtained from FFT analysis of the active flux. The test is performed using the laboratory setup with the PMSM run with sensorless FOC at 1800 rpm with 2 Nm load applied using BRLS adaptive filter with $\lambda = 0.999$ and $\sigma = 0.0005$. The data shown in figure 5.11 are achieved when the BRLS adaptive filter has converged.

(a) Input flux to the BRLS adaptive filter.   **(b)** Output flux of the BRLS adaptive filter.
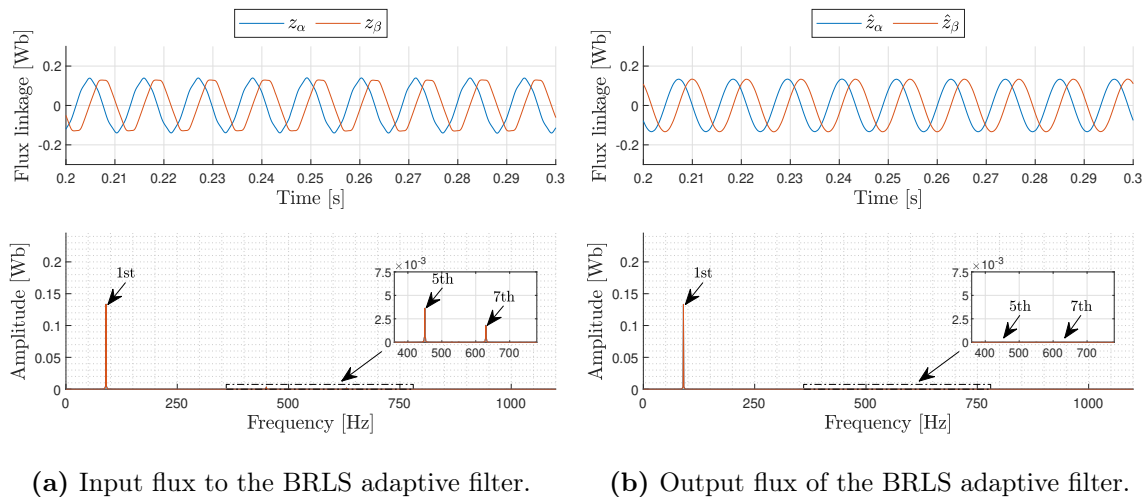
Figure 5.11. $\alpha\beta$ active flux and the frequency spectrum of the input and output of the filter using the BRLS adaptive filter with $\lambda = 0.999$ and $\sigma = 0.0005$. The PMSM is run at 1800 rpm with 2 Nm load applied.

From figure 5.11(a) it is seen, that the active flux waveform of the input to the BRLS adaptive filter is distorted. The frequency spectrum of the active flux shows, that the distortion is caused mainly by the (6 ± 1)th order harmonic components. Figure 5.11(b) shows that the active flux waveform of the output of the BRLS adaptive filter becomes more sinusoidal. From the frequency spectrum it is further seen, that the amplitude of the (6 ± 1)th order harmonic components is reduced significantly i.e. nearly zero. This indicates that the structure of the BRLS adaptive filter provides sufficient harmonic suppression capability when the filter has converged.

The harmonic suppression capabilities are further analyzed by examining the estimated position and the position error. The estimated position and position error obtained using PLL 1 and PLL 2 listed in table 4.1 with the BRLS adaptive filter are compared to see whether the PLL parameters affect the performance of the BRLS filter. Figure 5.12 and 5.13 illustrates the electrical rotor position and the position error when the PMSM is run at 360 rpm and 1800 rpm, respectively. The tests are performed with 2 Nm load applied to the system.
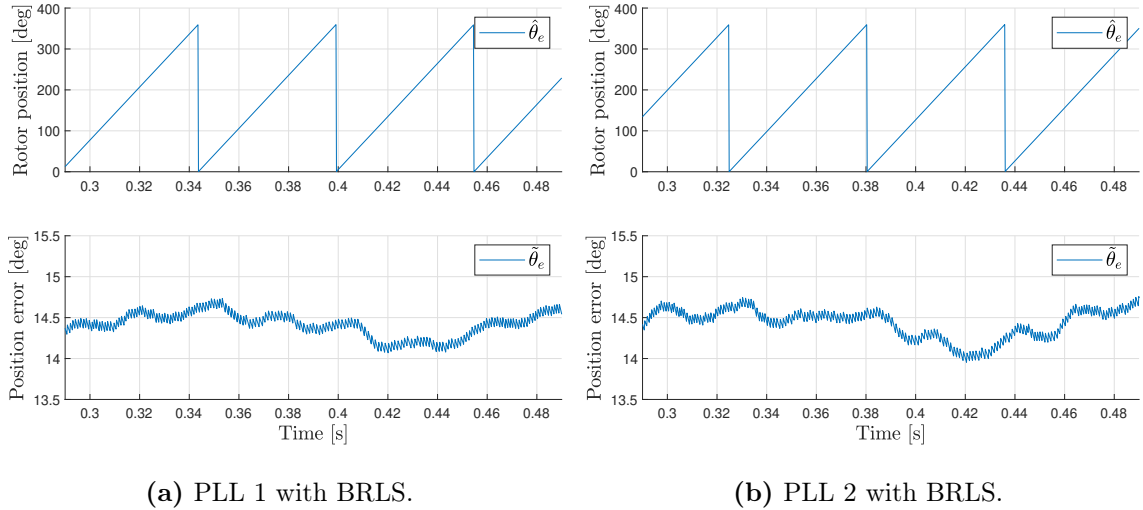
(a) PLL 1 with BRLS.   **(b)** PLL 2 with BRLS.
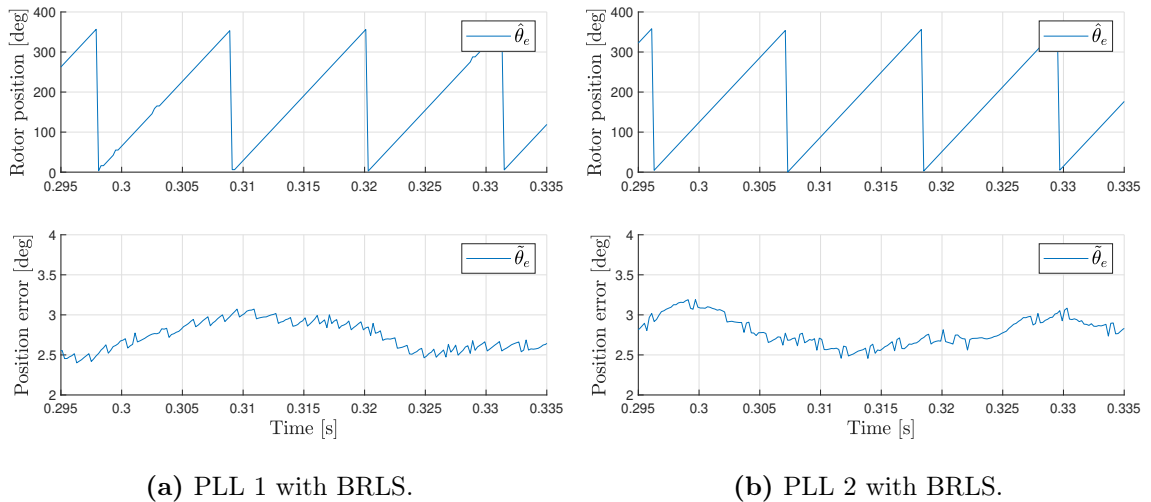
Figure 5.12. Electrical rotor position and the position error when the BRLS adaptive filter with $\lambda = 0.999$ and $\sigma = 0.0005$ is used. The PMSM is run at $360\,\text{rpm}$ with $2\,\text{Nm}$ load.

(a) PLL 1 with BRLS.   **(b)** PLL 2 with BRLS.

Figure 5.13. Electrical rotor position and the position error when the BRLS adaptive filter with $\lambda = 0.999$ and $\sigma = 0.0005$ is used. The PMSM is run at $1800\,\text{rpm}$ with $2\,\text{Nm}$ load.

From figure 5.12 it is seen, that no 6th order harmonic component is present in the position error using either PLL 1 or PLL 2 when the BRLS adaptive filter is enabled. Furthermore, it is seen that a corresponding 2nd order harmonic component is present in the position error along with some high frequency noise using either of the two used PLLs. As described in section 3.3, the 2nd order harmonic component may be caused by current measurement errors. The BRLS adaptive filter seems to provide good suppression of the 6th order harmonic component in the estimated position regardless of the choice of PLL parameters. When the PMSM is run at 1800 rpm it is seen from 5.13 that the 6th order harmonic ripples are removed using either of the PLLs from table 4.1. From the position error, there seems no difference using either of the PLLs. Based on the results illustrated in figures 5.12 and 5.13, the harmonic suppression capability of the 6th order harmonic component does not seem to be affected by the speed or the PLL parameters.

Based on the results illustrated in figures 5.11 to 5.13, the harmonic suppression capability

of the BRLS adaptive filter is considered sufficient. Thus, more analysis is performed to examine whether a difference in the dynamic performance is seen when using the BRLS adaptive filter.

5.3   Performance evaluation

The dynamic performance is examined by accelerating the PMSM from 900 rpm to 1800 rpm. Figure 5.14 illustrates the estimated rotor speed and the position error for tests using the designed PLLs listed in table 4.1 with and without the BRLS adaptive filter. The tests are performed with 2 Nm load applied to the system.
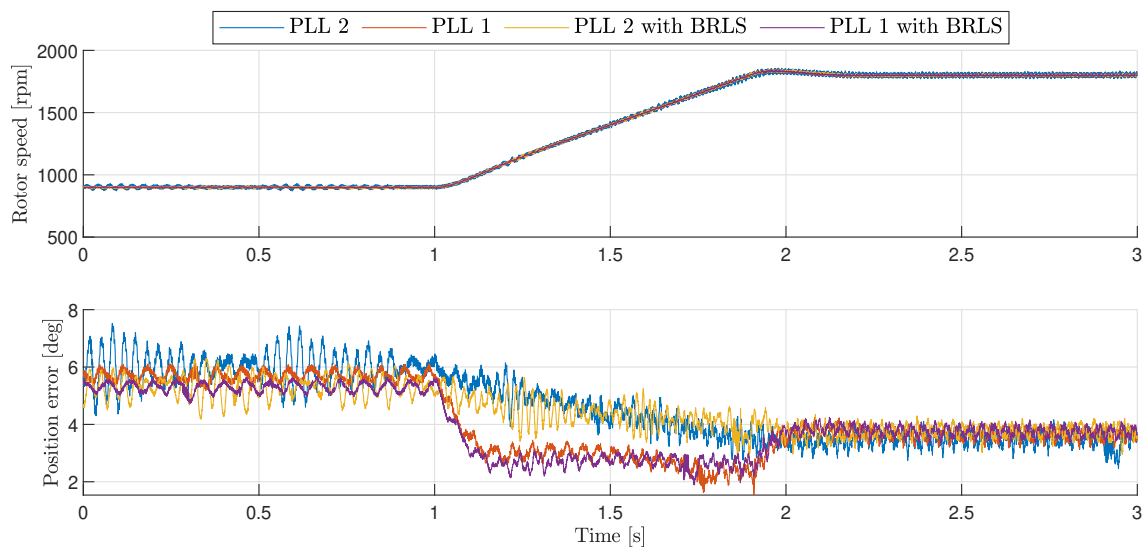
Figure 5.14. Estiamted rotor speed and position error for tests using the PLL 1 and PLL 2 listed in table 4.1 with and without the BRLS adaptive filter when the PMSM is accelerated.

It is seen from the estimated speed, that when the BRLS adaptive filter is not used, the estimated speed appears more fluctuating with larger ripples. This is also seen in the position error. From the position error it is further seen, that at time $0 \leq t \leq 1$ the mean of the position error when the BRLS adaptive filter is used appears to be less compared to the tests without the filter. This is the case using either PLL 1 or PLL 2. As the PMSM is accelerated at time $1 \leq t \leq 2$ the slope of the position error response seems similar with and without using the BRLS adaptive filter. However, it is seen, that as the speed increases, the position error when using the BRLS adaptive filter appears to become larger compared to using no filter. However, the difference in the position error for the tests with or without the BRLS adaptive filter is not significant and the responses when the speed is accelerated appear similar.

The dynamic performance is further examined by exposing the system to a sudden load change. Tests are performed with sensorless control with a speed reference at 360 rpm with 2 Nm load applied using the load motor. During the tests, the a step load is performed increasing the load from 2 Nm to 6 Nm and from 6 Nm to 2 Nm to examine the transient

response of the system. Figure 5.15 illustrates the estimated rotor speed and the position error for the tests.
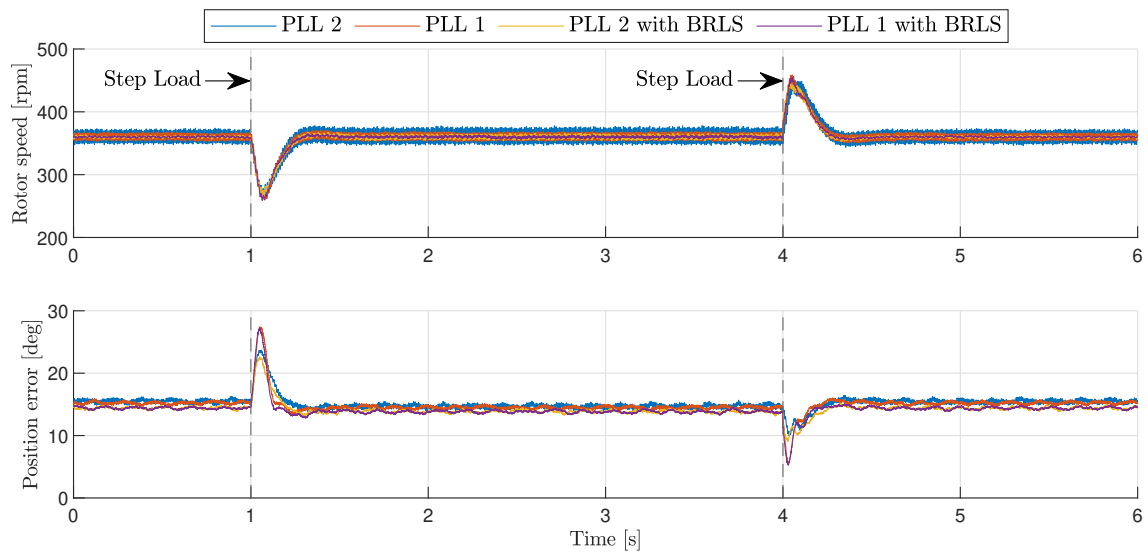

Figure 5.15. Estiamted rotor speed and position error for tests using the PLL 1 and PLL 2 listed in table 4.1 with and without the BRLS adaptive filter when a 4 Nm step load is applied to the system.

From figure 5.15 it is seen, that the estimated speed seems similar for all tests when a step load is applied to the system. From the position error it is seen, that the tests using the PLL 1 have larger peaks when the step load is applied, compared to the tests using PLL 2. This is caused by the difference in the bandwidth of the respective PLLs. From the tests it is further seen, that the position error is less when using the BRLS adaptive filter compared to the tests when the filter is not used. However, the use of the BRLS adaptive filter does not appear to affect the transient response of the system. The transient response when the load is changed is similar with and without the BRLS adaptive filter regardless of the choice of PLL. Hence, the BRLS adaptive filter does not seem to worsen the dynamic performance of the system.

From previous analysis of the BRLS adaptive filter, sufficient harmonic suppression capability is achieved using the filter. This is further seen from the estimated rotor speed and position error. It is seen that for the test using the PLL 2 without filtering the active flux, both the speed and position error is oscillating at steady state conditions. When the BRLS adaptive filter is applied together with the PLL 2, both the estimated speed and position error become more smooth, indicating the magnitude of harmonic components is reduced by the filter. This is further seen from figure 5.16 which illustrates the position error and frequency spectrum obtained from FFT analysis. Figure 5.16(a) is based on the data before the step load is applied at time $0 \leq t \leq 1$ and figure 5.16(b) is based on the data at time $2 \leq t \leq 3$.
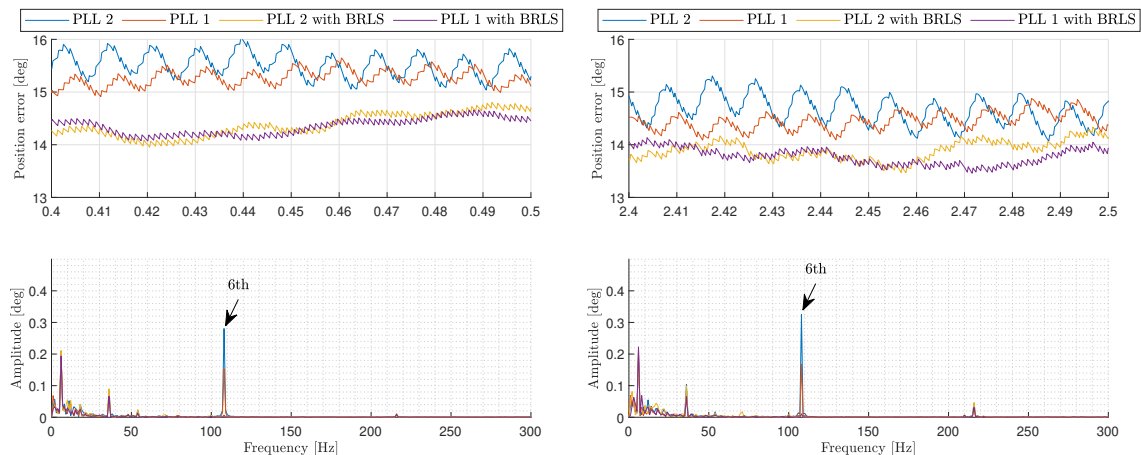
(a) $2\,\mathrm{Nm}$ load at time $0 \leq t \leq 1$ from figure 5.15.

(b) $6\,\mathrm{Nm}$ load at time $2 \leq t \leq 3$ from figure 5.15.

Figure 5.16. Position error and harmonic amplitude obtained from FFT analysis for the tests illustrated in figure 5.15. FFT analysis is performed at steady state speed.

From the position error in figure 5.16(a) and 5.16(b) it is seen, that the tests without BRLS contain a dominant frequency component with high magnitude. From the frequency spectrum it is seen, that the dominating frequency component, when BRLS adaptive filter is not used, corresponds to the 6th order harmonic component. The position error when BRLS is used shows that a more smooth signal is obtained, which seems only to contain some high order noise components. It is further seen, that the position error is approximately $1\,\mathrm{deg}$ less when using the BRLS adaptive filter. To better evaluate the suppression of the 6th order harmonic component, the amplitude of the corresponding 6th order harmonic component for the results illustrated in figure 5.16 are listed in table 5.1.

	6th amplitude [deg]	
	$\tau_L = 2\,\mathrm{Nm}$	$\tau_L = 6\,\mathrm{Nm}$
PLL 1	0.1533	0.1678
PLL 1 + BRLS	0.0057	0.0104
PLL 2	0.2812	0.3253
PLL 2 + BRLS	0.0071	0.0110

Table 5.1. Amplitude of the 6th order harmonic component in the position error $\tilde{\theta}_e$ using different PLL parameters with and without the BRLS adaptive filter when $\omega_m = 360\,\mathrm{rpm}$.

From the table it is seen, that when $2\,\mathrm{Nm}$ is applied the 6th order harmonic component is reduced significantly from the position error when the BRLS adaptive filter is used. This is the case using either PLL 1 or PLL 2 as position and speed estimator. When $6\,\mathrm{Nm}$ is applied, similar tendencies are seen, as the magnitude of the 6th order harmonic component when the BRLS adaptive filter is used is significantly reduced compared to the tests with no filtering. With the BRLS adaptive filter, the 6th order harmonic component is reduced to a level at which it can be neglected. Thus, the BRLS adaptive filter is considered to provide sufficient harmonic suppression capability of the 6th order harmonic component

at different load conditions.

Similar tests with the system are performed at 1800 rpm, to see whether differences in the harmonic suppression capability, as well as the transient response, are seen compared to at lower speeds. Figure 5.17 illustrates the estimated rotor speed and the position error for tests with the laboratory setup using the two PLLs listed in table 4.1 with and without using the BRLS adaptive filter.
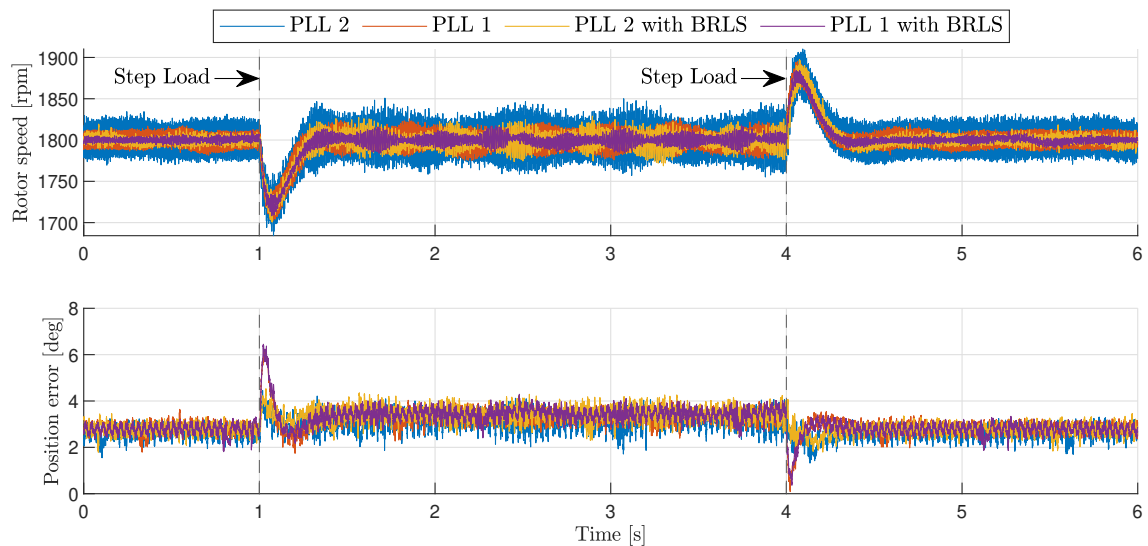

Figure 5.17. Estiamted rotor speed and position error for tests using the PLL 1 and PLL 2 listed in table 4.1 with and without the BRLS adaptive filter when a 4 Nm step load is applied to the system.

From the position error it is seen, that when the load step is applied, the peak is similar for the tests with and without the BRLS adaptive filter. This is the case using either PLL 1 or PLL 2. Hence, the BRLS adaptive filter does not introduce further phase shift to the system. It is further seen, that using the PLL 2 in the position and speed estimator, the signals are more fluctuating. This is due to the high k_p and k_i parameters for this PLL, which results in more noisy signals. However, when the BRLS adaptive filter is used, the peak of the ripples is greatly reduced. From the estimated speed at time $1 \leq t \leq 4$ when 6 Nm load is applied to the system it is seen, that the speed ripples vary. Thus, same tendencies are seen with the BRLS adaptive filter as it is seen with the CCSFF method illustrated in figure 4.16.

Further analysis of the frequency components is performed by FFT analysis of the position error for the respective tests illustrated in figure 5.17. Figure 5.18(a) is based on the data before the step load is applied at time $0 \leq t \leq 1$ and figure 5.18(b) is based on the data at time $2 \leq t \leq 3$.
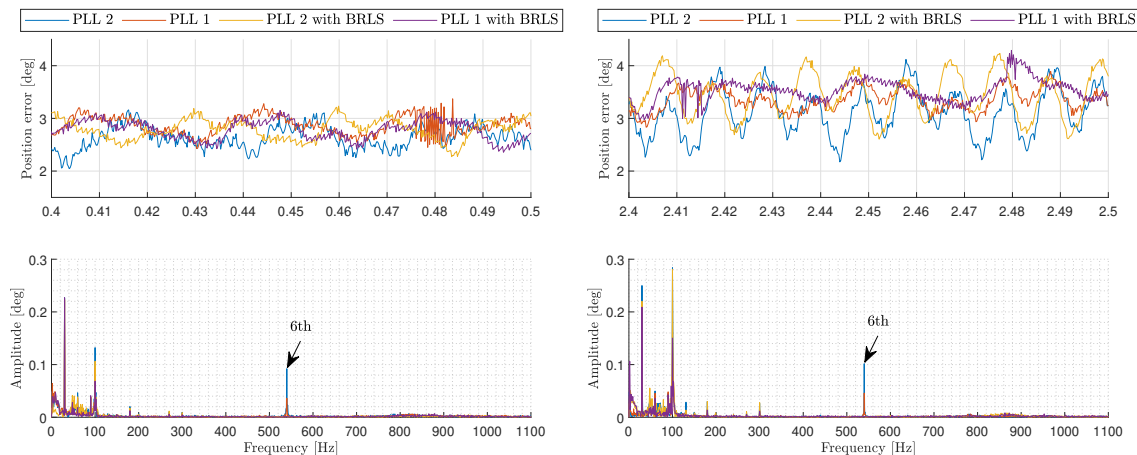
(a) 2 Nm load at time $0 \leq t \leq 1$ from figure 5.17.

(b) 6 Nm load at time $2 \leq t \leq 3$ from figure 5.17

Figure 5.18. Position error and harmonic amplitude obtained from FFT analysis for the tests illustrated in figure 5.17. FFT analysis is performed at steady state speed.

From the frequency spectrum in figures 5.18(a) and 5.18(b) it is seen, that the corresponding 6th order harmonic component is not the dominant component in the position error. It is further seen, that the amplitude of the 6th order harmonic component when using PLL 1 or PLL 2 is less compared to when the PMSM is operated at 360 rpm as seen in figure 5.16. This is expected, as the frequency of the corresponding 6th order harmonic component increases with the speed of the PMSM, hence the 6th order harmonic component will be more attenuated by the PLL itself. Comparing figures 5.18(a) and 5.18(b) it is seen, that when the load is increased to 6 Nm, the amplitude of the 100 Hz frequency component is increased significantly when PLL 2 with high k_p and k_i parameters is used. It is the case with and without the BRLS adaptive filter. Thus, it seems to be affected by the PLL parameters.

To better evaluate the suppression of the 6th order harmonic component, the amplitude of the corresponding 6th order harmonic component for the results illustrated in figure 5.18 are listed in table 5.2.

| | 6th amplitude [deg] ||
	$\tau_L = 2\,\mathrm{Nm}$	$\tau_L = 6\,\mathrm{Nm}$
PLL 1	0.0388	0.0439
PLL 1 + BRLS	0.0016	0.0014
PLL 2	0.0940	0.1008
PLL 2 + BRLS	0.0017	0.0011

Table 5.2. Amplitude of the 6th order harmonic component in the position error $\tilde{\theta}_e$ using different PLL parameters with and without the BRLS adaptive filter when $\omega_m = 1800\,\mathrm{rpm}$.

From the table it is seen, that when 2 Nm is applied the 6th order harmonic component is reduced significantly from the position error when the BRLS adaptive filter is used. This is the case using either PLL 1 or PLL 2 as position and speed estimator. When 6 Nm is

applied, similar tendencies are seen, as the amplitude of the 6th order harmonic component when the BRLS adaptive filter is used is significantly reduced compared to the tests with no filtering. With the BRLS adaptive filter, the 6th order harmonic component is reduced to a level at which it can be neglected.

Based on the examination of the dynamic performance of the system using the BRLS adaptive filter, it is seen that the BRLS adaptive filter is capable of significantly reducing the (6 ± 1)th order harmonic components in the active flux. This affects the position and speed estimation, as the corresponding 6th order harmonic component in the estimated position is reduced to no longer being a dominant component. The BRLS adaptive filter only ensures good harmonic suppression capability of the specified harmonic components i.e. (6 ± 1)th order harmonic components in the active flux corresponding to 6th order harmonic component in estimated position and speed. Regardless of the PLL parameters and the rotor speed, the 6th order harmonic component in the estimated speed is reduced to a level of which it is considered insignificant. From the performance tests when the system is exposed to a sudden load change it is seen, that the BRLS adaptive filter does not affects the dynamic performance.

Filter comparison and results discussion 6

In this chapter the CCSFF and BRLS adaptive filter are compared based on the result from chapter 4 and 5 respectively. The filters are compared based on the criteria in section 1.1. Furthermore, the influence of the filtering capability of the estimated flux is examined to determine the efficiency of filtering the (6 ± 1)th harmonic components.

6.1 Filter comparison

With the CCSFF and the BRLS adaptive filter individually tested and elaborated with the laboratory setup, the performance and results of the two methods are in this section compared. The comparison of the two filtering methods is based on the evaluation criteria set in section 1.1. Figure 6.1 illustrates the estimated rotor speed and the position error for experimental tests performed with the PLL 1 with and without the BRLS adaptive filter, and the CCSFF 1 listed in table 4.1. The tests are performed with the PMSM run at 360 rpm with 2 Nm load applied. During the tests, a step load is applied increasing the load from 2 Nm to 6 Nm and from 6 Nm to 2 Nm.
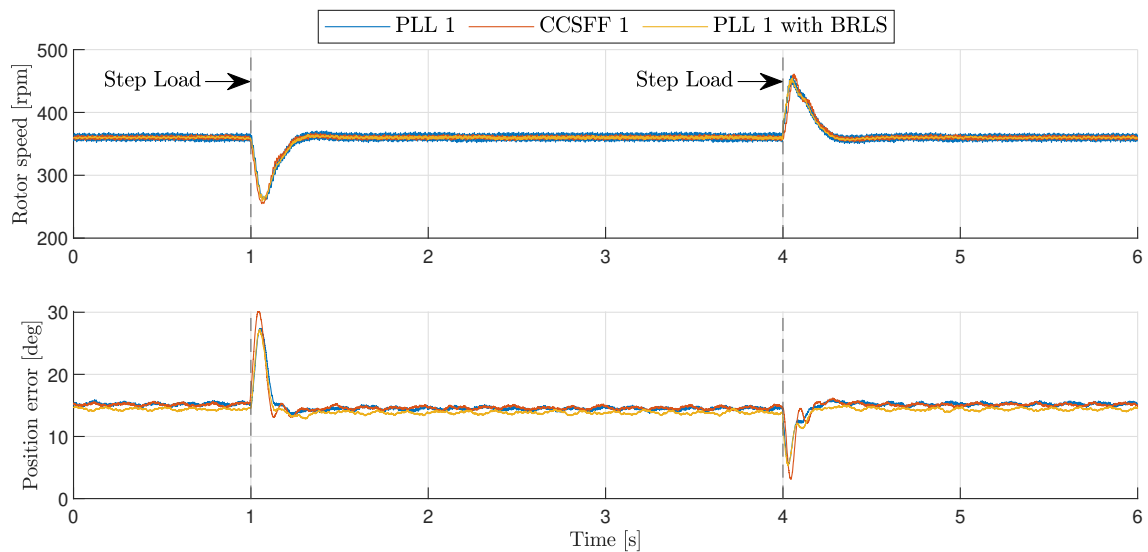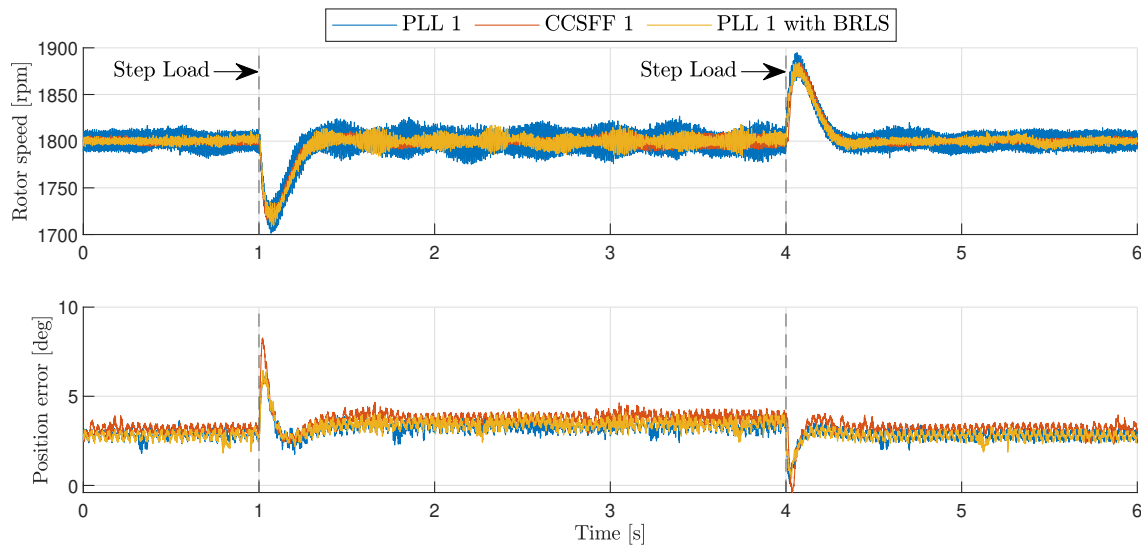

Figure 6.1. Estiamted rotor speed and position error for tests using the PLL 1 with and without the BRLS adaptive filter and the CCSFF 1 listed in table 4.1 when a 4 Nm step load is applied to the system.

From the figure it is seen that the speed response, when a step load is exposed to the system, is similar for the tests. Furthermore, the magnitude of the ripples in the speed estimation is reduced using both filtering methods. This is also seen in the position error. When the load is applied at time $t = 1$ it is seen that similar responses are seen in the position error the PLL 1 is used with and without the BRLS adaptive filter. When the

CCSFF 1 is used, the peak of the position error is increased. This indicates, that the CCSFF introduces further phase delay to the system. However, as evaluated in section 4.3 and seen in figure 4.18 the response of the CCSFF 1 can be improved by making the parameters adaptive. This will increase the bandwidth of the CCSFF 1 and improve the response. The adaptive method to increase the bandwidth is not necessary to implement using the BRLS adaptive filter to achieve the same response as when only the PLL 1 is used. The same tendencies are seen when the PMSM is run at 1800 rpm which is illustrated in figure 6.2.

Figure 6.2. Estiamted rotor speed and position error for tests using the PLL 1 and PLL 2 listed in table 4.1 with and without the BRLS adaptive filter when a 4 Nm step load is applied to the system.

From the estimated speed and position error in figures 6.1 and 6.2 it is seen, that the signals appear less fluctuating when filtering the active flux is performed with either the CCSFF or with the BRLS adaptive filter. In figures 6.3 and 6.4 the position error and the frequency spectrum of the position error obtained from FFT analysis are illustrated for when the PMSM is run at 360 rpm and 1800 rpm, respectively.
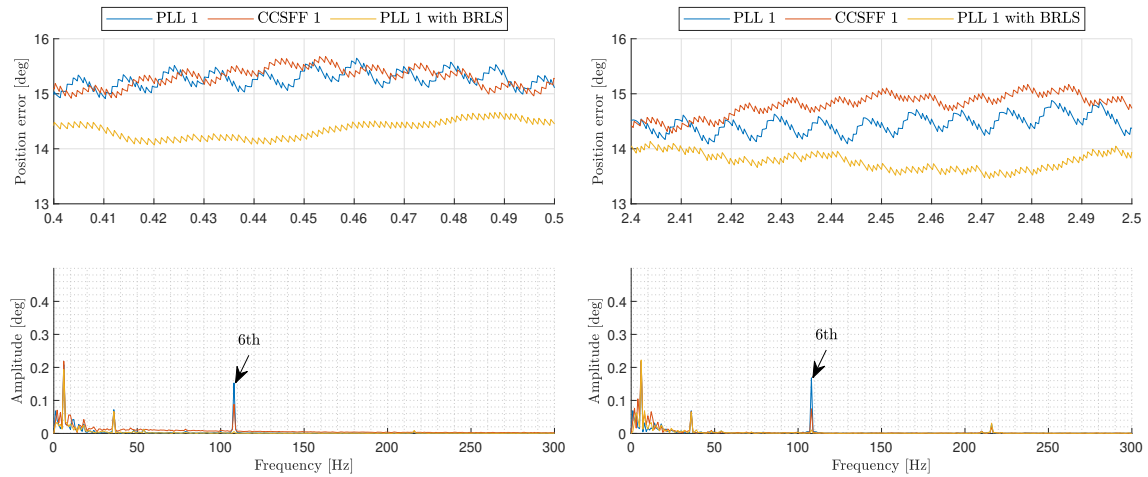
(a) 2 Nm load at time $0 \leq t \leq 1$ from figure 6.1.

(b) 6 Nm load at time $2 \leq t \leq 3$ from figure 6.1

Figure 6.3. Position error and harmonic amplitude obtained from FFT analysis for the tests illustrated in figure 6.1. FFT analysis is performed at steady state speed.
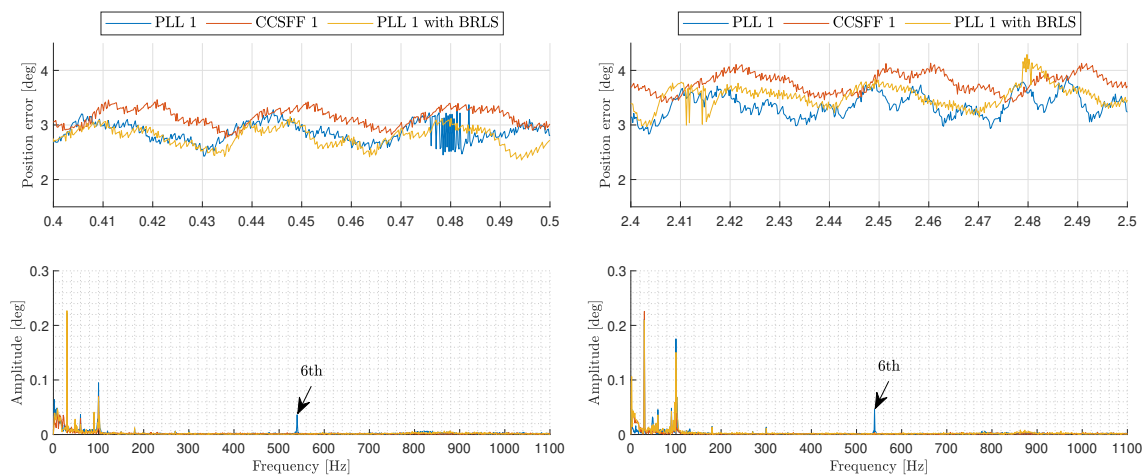
(a) 2 Nm load at time $0 \leq t \leq 1$ from figure 6.2.

(b) 6 Nm load at time $2 \leq t \leq 3$ from figure 6.2

Figure 6.4. Position error and harmonic amplitude obtained from FFT analysis for the tests illustrated in figure 6.2. FFT analysis is performed at steady state speed.

From the frequency spectrum it is seen, that the amplitude of the frequencies besides the corresponding 6th order harmonic component seems similar for all tests. When the PMSM is run at 360 rpm in figure 6.3 it is seen that both filtering methods are capable of attenuating the corresponding 6th order harmonic component in the position error. However, the BRLS adaptive filter seems to provide better suppression capability, as the 6th order harmonic component is nearly zero. The amplitude is approximately halved using the CCSFF 1. When the PMSM is run at 1800 rpm as seen in figure 6.4 the harmonic suppression capability of the CCSFF 1 and BRLS adaptive filter seems to be equally good, with the 6th-order harmonic component reduced to a neglectable level.

Similar tests are performed with the PLL 2 with and without the BRLS adaptive filter,

and the CCSFF 2 listed in table 4.1. Figures 6.5 and 6.6 illustrate the estimated rotor speed and the position error for the experimental tests when the PMSM run at 360 rpm and 1800 rpm, respectively. The tests are performed with 2 Nm load applied. During the tests, a step load is applied increasing the load from 2 Nm to 6 Nm and from 6 Nm to 2 Nm is applied.
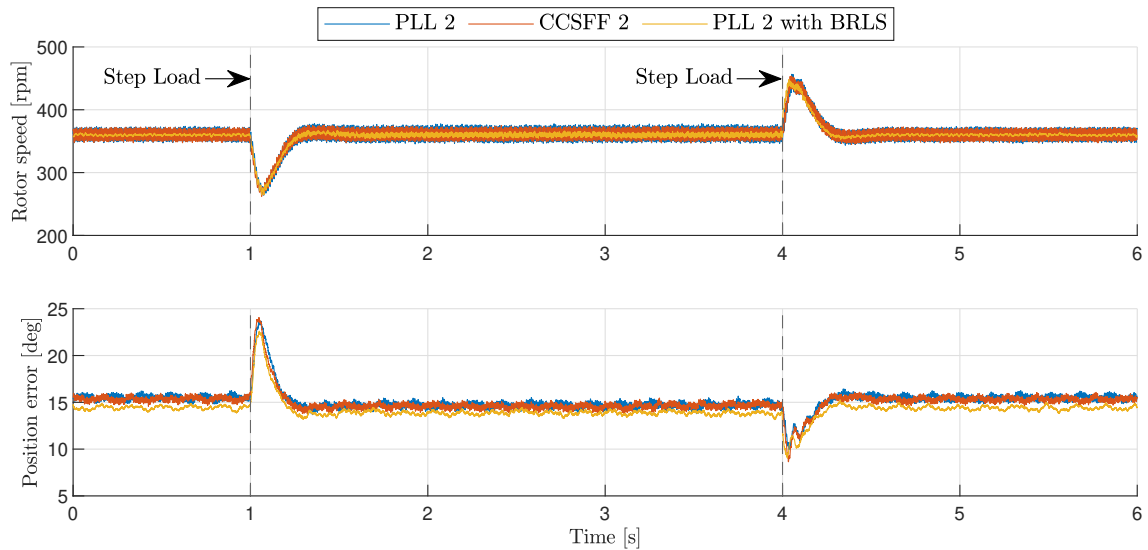

Figure 6.5. Estiamted rotor speed and position error for tests using the PLL 2 with and without the BRLS adaptive filter and the CCSFF 2 listed in table 4.1 when a 4 Nm step load is applied to the system.
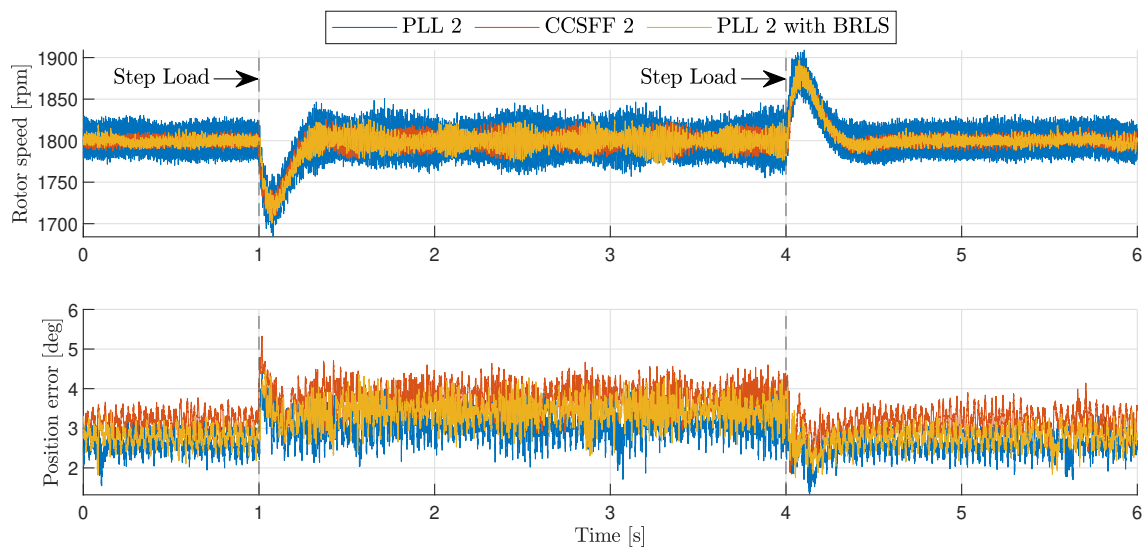

Figure 6.6. Estiamted rotor speed and position error for tests using the PLL 2 with and without the BRLS adaptive filter and the CCSFF 2 listed in table 4.1 when a 4 Nm step load is applied to the system.

From figure 6.5 it is seen that the speed response when a step load is exposed to the system is similar for the tests. Furthermore, the magnitude of the ripples in the speed estimation is reduced using the BRLS adaptive filter. However, the CCSFF 2 has poor

harmonic suppression capability at 360 rpm. When the load is applied at time $t = 1$, similar responses are seen in the position error with PLL 2 and CCSFF 2. The CCSFF 2 provides better dynamic performance due to higher bandwidth compared to what is seen with CCSFF 1. The CCSFF 2 achieves a similar response as the PLL 2 without adding the adaptive parameter method. When the BRLS adaptive filter is used, the peak in the position error when the load is applied appears to be smaller compared to PLL 2 and CCSFF 2. However, the steady state position error is seen to have an offset compared to the other tests. Thus, the change in the position error when a step load is applied appears to be similar for all tests.

From figure 6.6 similar tendencies are seen regarding the dynamic performance of the different tests. The harmonic suppression capability of the CCSFF 2 is improved as the speed increases. This is seen from the estimated speed, as the magnitude of the speed ripples is reduced as is the case using the BRLS adaptive filter. In figures 6.7 and 6.8 the position error and the frequency spectrum of the position error obtained from FFT analysis are illustrated for when the PMSM is run at 360 rpm and 1800 rpm, respectively.
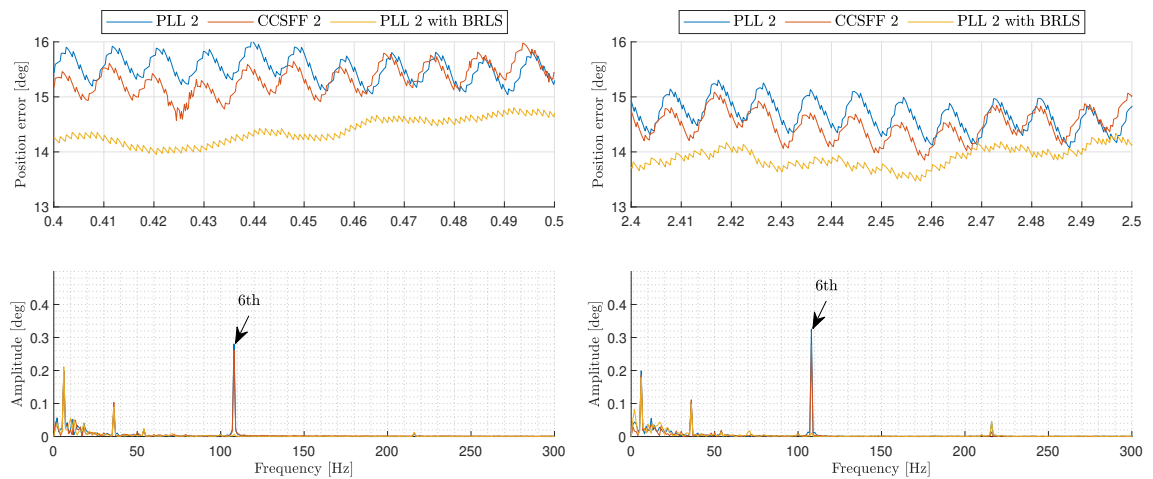
(a) 2 Nm load at time $0 \leq t \leq 1$ from figure 6.5.

(b) 6 Nm load at time $2 \leq t \leq 3$ from figure 6.5

Figure 6.7. Position error and harmonic amplitude obtained from FFT analysis for the tests illustrated in figure 6.5. FFT analysis is performed at steady state speed.
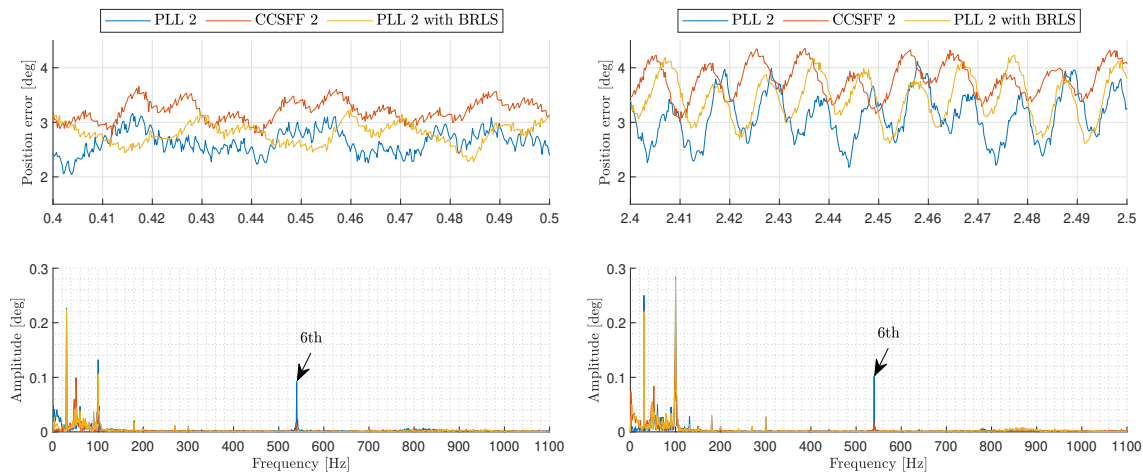
(a) 2 Nm load at time $0 \leq t \leq 1$ from figure 6.6.

(b) 6 Nm load at time $2 \leq t \leq 3$ from figure 6.6

Figure 6.8. Position error and harmonic amplitude obtained from FFT analysis for the tests illustrated in figure 6.6. FFT analysis is performed at steady state speed.

From figure 6.7 it is seen, that the position error when the CCSFF 2 is used is similar to the PLL 2 due to the poor harmonic suppression capability of the CCSFF 2 at lower speed. Using the BRLS adaptive filter the position error is more filtered, as the signal appears more smooth. From the frequency spectrum it is seen, that the amplitude of the frequencies besides the corresponding 6th order harmonic component seems similar for all tests. When the PMSM is run at 1800 rpm the harmonic suppression capability of the CCSFF 2 and BRLS adaptive filter seems to be equally good, with the 6th-order harmonic component reduced to a neglectable level.

In table 6.1, the amplitude of the 6th order harmonic component is listed for the tests illustrated in figures 6.1, 6.2, 6.5, and 6.6.

| | 6th amplitude [deg] | | | |
| | $\omega_m = 360\,\mathrm{rpm}$ | | $\omega_m = 1800\,\mathrm{rpm}$ | |
	$\tau_L = 2\,\mathrm{Nm}$	$\tau_L = 6\,\mathrm{Nm}$	$\tau_L = 2\,\mathrm{Nm}$	$\tau_L = 6\,\mathrm{Nm}$
PLL 1	0.1533	0.1678	0.0388	0.0439
CCSFF 1	0.0881	0.0746	0.0027	0.0038
PLL 1 + BRLS	0.0057	0.0104	0.0016	0.0014
PLL 2	0.2812	0.3253	0.0940	0.1008
CCSFF 2	0.2625	0.2764	0.0154	0.0177
PLL 2 + BRLS	0.0071	0.0110	0.0017	0.0011

Table 6.1. Amplitude of the 6th order harmonic component in the position error $\tilde{\theta}_e$.

From the table it is seen, that the presented filter methods are capable of suppressing the 6th order harmonic component in the estimated position caused by inverter nonlinearities. However, a significant difference in the harmonic suppression capability between the methods is seen. For the CCSFF method, the parameter design has a significant influence on the performance. When the PMSM is run at 360 rpm, the CCSFF 2 does not reduce the

6th order harmonic component to a level of which it is considered to be insignificant. This is due to the bandwidth of the CCSFF being close to the frequency of the corresponding 6th order harmonic component. Hence, it is not attenuated enough. The CCSFF 1 does approximately half the amplitude of the 6th order harmonic component compared to when compared to using a PLL with the same bandwidth. With the BRLS adaptive filter it is seen, that good harmonic suppression capability is obtained regardless of the bandwidth of the PLL. When the PMSM is run at 1800 rpm, the CCSFF 1 and the BRLS adaptive filter provides similar harmonic suppression capability. The CCSFF 2 is capable to reduce the 6th order harmonic component significantly. However, it is not capable of reducing it to the same level as the BRLS adaptive filter.

The BRLS adaptive filter estimates the (6 ± 1)th order harmonic components in the distorted active flux. The estimate is then subtracted from the original distorted active flux signal. Thus, the BRLS adaptive filter is actively compensating for the distortion in the flux to obtain a smooth active flux signal to estimate the position and speed of the rotor. The CCSFF has characteristics of a low pass filter, hence the cut-off frequency of the filter has a huge impact on the suppression capability. This is seen from the results listed in table 6.1. This also means that the CCSFF is capable of attenuating other higher frequency components. The BRLS adaptive filter is only affecting the specified harmonic components, which is only the (6 ± 1)th order harmonic components in this thesis. If desired, the BRLS adaptive filter can be expanded to handle other harmonic components. However, this will require additional coding and will increase the calculations.

6.2   Influence of filtering harmonic

In chapter 4 and 5 it is shown that the CCSFF and BRLS adaptive filter suppresses the (6 ± 1)th order harmonic component in the active flux and the 6th order harmonic component in the estimated position and speed well. By filtering the (6 ± 1)th order harmonic component in the active flux it is seen that the estimated position and speed are significantly improved. The influence of a more accurate position and speed estimation is examined to see whether the filtering improves the general control of the PMSM.

In motor control, high accuracy and efficiency are two key factors when designing the control structure. High accuracy is typically dependent on the application however, this thesis is based on sensorless speed control, hence high accuracy in the real speed is desired. The real rotor speed is therefore relevant to examine. As electrification continues to increase, there is more focus on an energy-efficiency system. Furthermore, a very efficient system lower the cost of operation. To examine the efficiency it is advantageous to look at the currents while running the PMSM.

Figure 6.9 illustrates the estimated and real rotor speed with and without filters. Additionally, the phase a current is illustrated as well. The test is for the PMSM run in sensorless at 360 rpm.
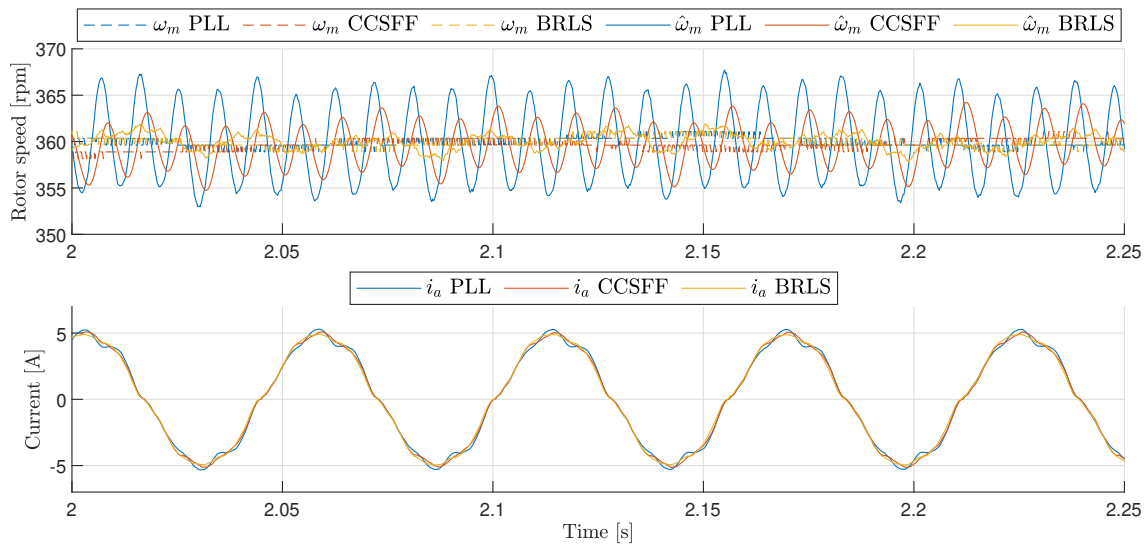
Figure 6.9. Real and estimated rotor speed and phase a current with and without filter when $\omega_m = 360\,\text{rpm}$.

It is seen that the peak-to-peak value in the estimated speed is reduced with filters enabled as expected. However, the real speed is not affected despite the estimation is improved. From the phase a current i_a it is seen that the current is improved when filtering. The current is more sinusoidal and the peak-to-peak value is reduced slightly when filters are enabled. Similar tests are performed while running the PMSM at 1800 rpm. The result is illustrated in figure 6.10.
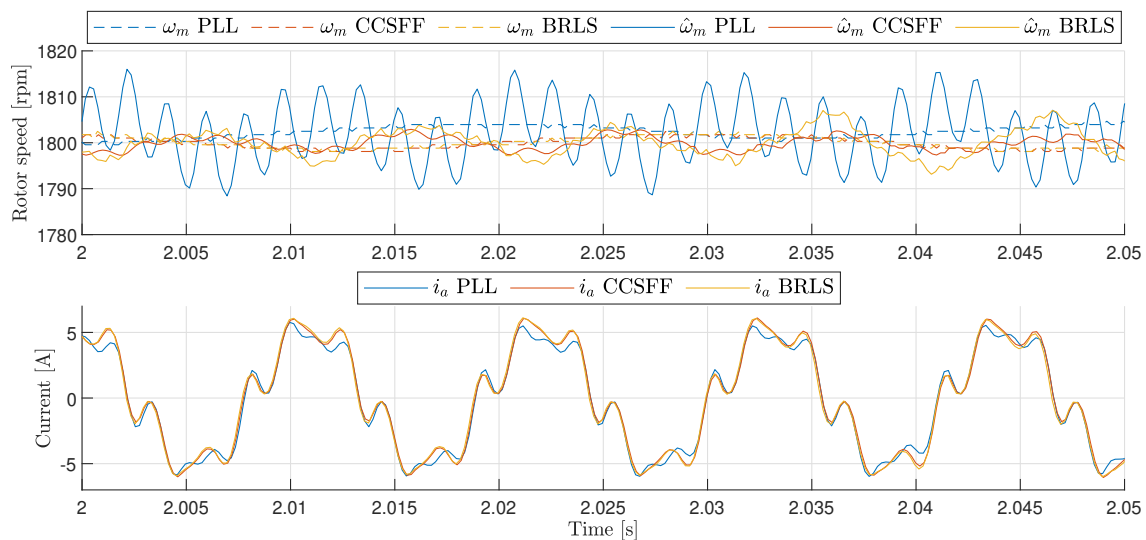

Figure 6.10. Real and estimated rotor speed and phase a current with and without CCSFF or BRLS when $\omega_m = 1800\,\text{rpm}$.

It is seen that the same tendency as in figure 6.9 is seen when comparing the speed. The peak-to-peak value of the estimated speed is significantly lower with filters enabled, however the real rotor speed is not affected by the filters. When looking at the phase a current it is seen that the current is not improved with filter enabled as it is seen in figure

6.9 despite having a better estimation. Instead, the phase a current is worsened slightly as the peak-to-peak value is increased with filter on.
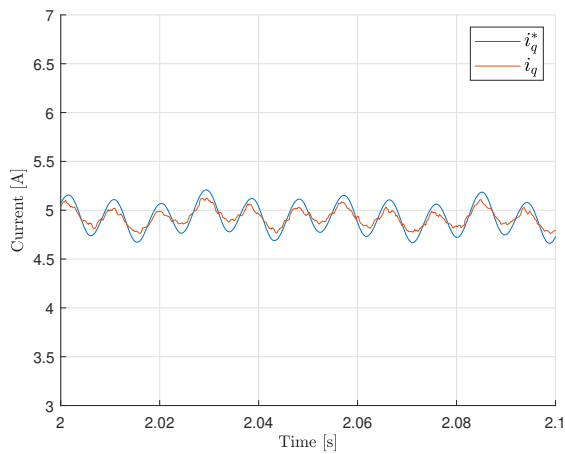
To examine more on this behavior the reference i_q^* and current i_q are illustrated in figure 6.11 while the PMSM is run at $\omega_m = 360$ rpm and $\omega_m = 1800$ rpm.
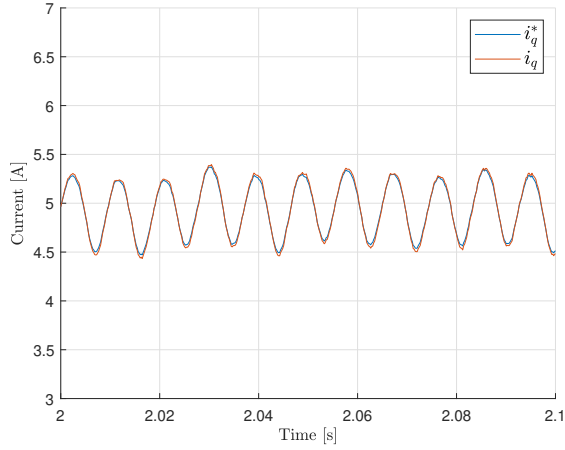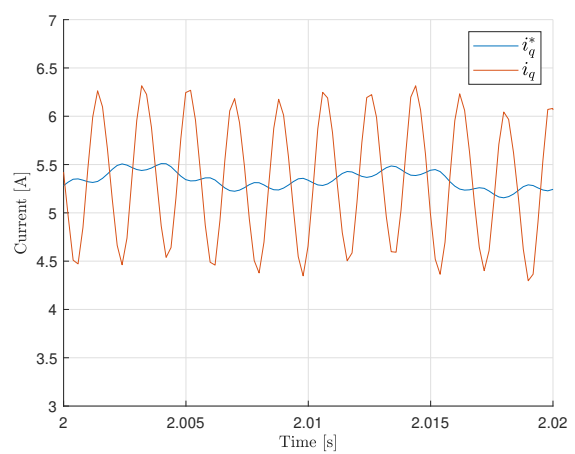
(a) PLL when $\omega_m = 360$ rpm.
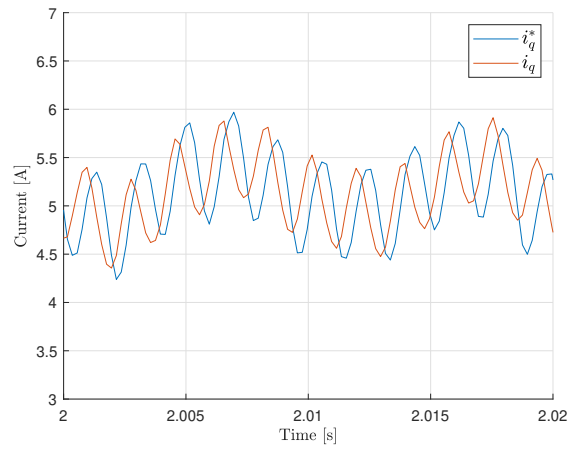
(b) PLL when $\omega_m = 1800$ rpm.

(c) CCSFF when $\omega_m = 360$ rpm.

(d) CCSFF when $\omega_m = 1800$ rpm.

(d) BRLS when $\omega_m = 360\,\mathrm{rpm}$. **(e)** BRLS when $\omega_m = 1800\,\mathrm{rpm}$.
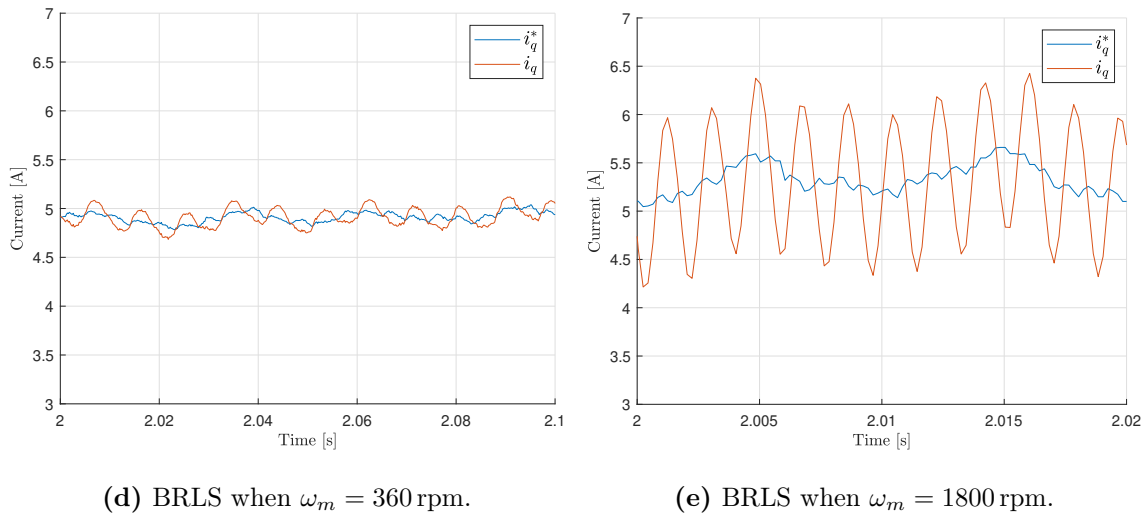
Figure 6.11. Reference and measured q-axis currents with and without filtering of the estimated active flux when the PMSM is run at 360 rpm.

In figure 6.11(a) it is seen that current i_q follows the reference i_q^* well at 360 rpm. Only a slight phase shift is seen between i_q^* and i_q. i_q^* and i_q contains 6th order harmonics. When the speed is increased to 1800 rpm as in figure 6.11(b) it is seen that i_q starts to lag i_q^* significantly more and that the peak to peak value is increased a bit for i_q^* and i_q. In figure 6.11(c) it is seen that the peak-to-peak value of i_q^* is decreased with the CCSFF on as expected. The reduced peak-to-peak value is also seen in the i_q. At 1800 rpm it is seen that i_q^* is reduced further due to the better performance at higher speed for the CCSFF. However, it is seen that i_q is amplified significantly compared to figure 6.11(b) even though i_q^* is reduced. In figure 6.11(d) it is seen that the peak-to-peak value of i_q^* and i_q is reduced with BRLS as for the CCSFF in figure 6.11(c). When the speed is increased same tendency as in figure 6.11(d) is seen.

From figure 6.11 it is seen that at low speed the CCSFF or BRLS reduce the peak-to-peak value in i_q^* and i_q. This is also expected due to the improved phase a current seen in figure 6.9. At 1800 rpm it is seen that i_q is worsened with CCSFF or BRLS, this substantiates why it is seen in figure 6.10 that the CCSFF or BRLS do not improve the phase a current.

According to figure 6.11 the lack of improvement in the phase a current at high speed appears to be caused by the current loop which is not capable of controlling i_q to be equal to i_q^*. At low speed, the current controller is fast enough to make the real current i_q follow the reference current i_q^* and thereby compensate for the voltage drop caused by the inverter nonlinearities and flux spatial harmonics. At high speed, even though the reference current does not contain 6th order ripples, the 6th order voltage ripple caused by inverter non-linearity and flux spatial harmonics cannot be compensated properly by the current controller, which results in large 6th order current ripple in the actual current.

The current loop is limited by the switching frequency and the bandwidth. The current loop is designed in section 2.2. By further examining the current response in figure 2.2 it is seen that a delay is present in the system. The current step response is enlarged and illustrated in figure 6.12.
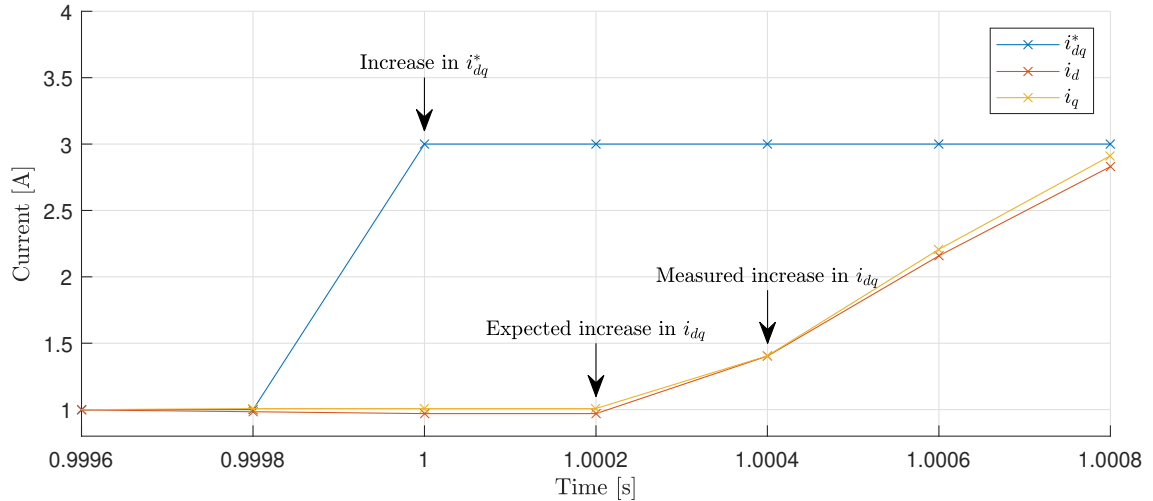
Figure 6.12. Step responses of the *dq*-currents with the PI controllers in (2.9) and (2.10) implemented in the control structure in the laboratory setup.

From figure 6.12 it is seen that as the current reference is increased it is first seen in the measured current two time steps later. At $\omega_m = 360$ rpm this does not affect the performance significantly as the 6th order component is only shifted approximately 8 deg/sample however a minor phase shift in i_q is expected. At $\omega_m = 1800$ rpm the waveform from the 6th order component is shifted 39 deg/sample which will affect the performance of the current control. Besides the switching frequency, the bandwidth of the current loop influences the performance of the current loop. The current loop bandwidth is designed in section 2.2 with a bandwidth of $\omega_c \approx 2000$ rad/s. The frequency of the 6th order harmonic component at 360 rpm and 1800 rpm are $\omega_{e,6th} \approx 679$ rad/s and $\omega_{e,6th} \approx 3393$ rad/s respectively. A bode diagram of the closed loop current system is illustrated in figure 6.13. The closed loop system is given by (6.1) utilizing (2.7) and (2.10) from section 2.2.

$$\frac{i_q}{i_q^*} = \frac{G_{c,q} \cdot G_{p,q}}{1 + G_{c,q} \cdot G_{p,q}} \qquad (6.1)$$
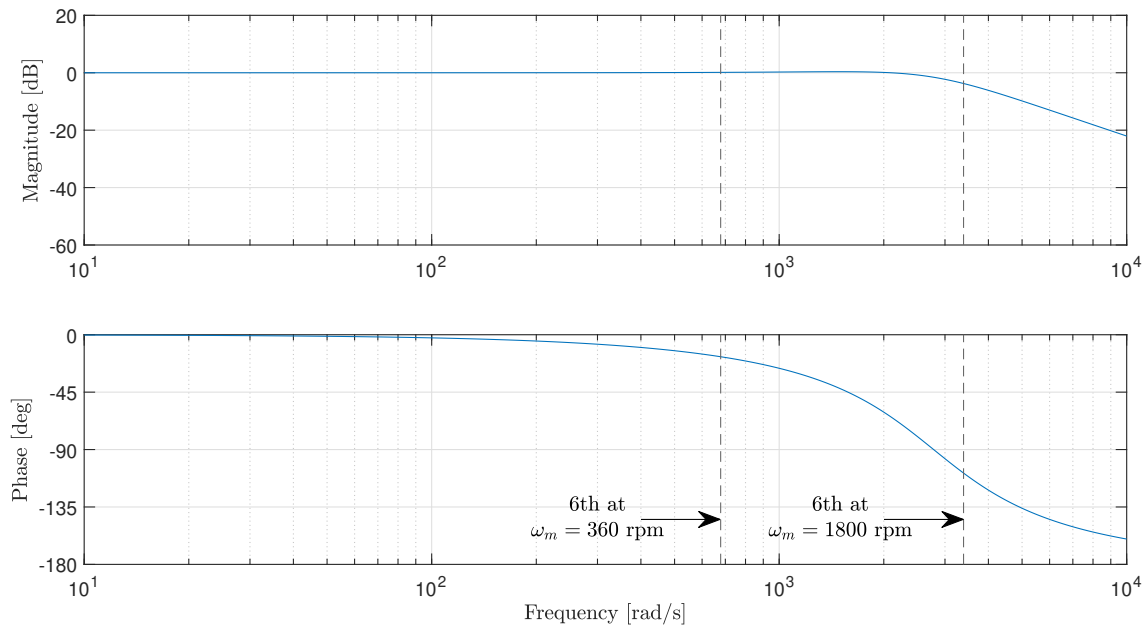
Figure 6.13. Bode diagram of the current loop system in (6.1).

From the bode diagram it is seen that at $679\,\mathrm{rad/s}$ which corresponds to the frequency of the oscillations in i_q at $\omega_m = 360\,\mathrm{rpm}$ the phase is approximately $-20\,\mathrm{deg}$. At $\omega_m = 1800\,\mathrm{rpm}$ the phase is significantly lower at approximately $-110\,\mathrm{deg}$. To reduce the phase shift the bandwidth can be increased. However, from the current step response in figure 2.2 it is seen that the current loop is already designed quite aggressively with a large overshoot. Increasing the bandwidth will increase the overshoot and better performance may not be achieved combined with the limitations from the sample delay discussed earlier.

The improvement of the currents with CCSFF and BRLS adaptive filter seems to be limited by the phase shift mainly caused by the high frequency of the 6th order harmonic. Increasing the speed increases the frequency and worsens the current. These limitations are correlated to the specifications of the system utilized in this thesis. Large phase shift in the 6th order harmonic component per sample are related to the switching frequency as well as the number of pole pairs in the PMSM. In figure 6.14 the 6th order harmonic component phase shift and the frequency of the 6th order harmonic are illustrated for different switching frequencies and number of pole pairs.
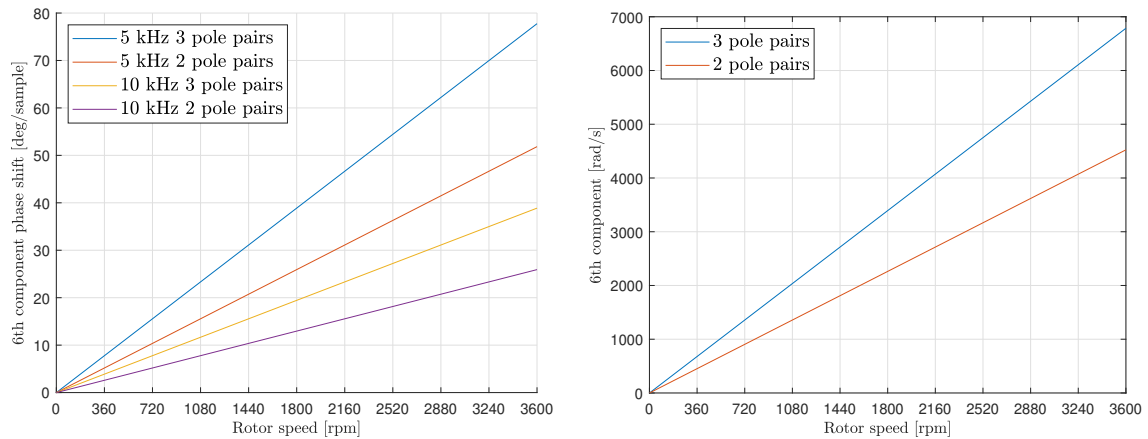
(a) Phase shift of the 6th order harmonic component.

(b) Frequency of the 6th order harmonic component.

Figure 6.14. Influence of switching frequency and number of pole pairs on the 6th order harmonic component.

From figure 6.14(a) it is seen that the phase shift per sample can be mitigated by using a PMSM with less number of pole pairs. This is due to the 6th order harmonic being directly proportional to the number of pole pairs as illustrated in figure 6.14(b). Furthermore, it is seen that the phase shift is inversely proportional to the switching frequency. According to figure 6.14 it is expected that the performance at higher speed with CCSFF or BRLS adaptive filter can be improved by increasing the switching frequency or having less number of pole pairs. Hence the current loop should compensate the 6th order harmonic easier. It should be noticed that having less number of pole pairs may affect the performance of the CCSFF filtering capability due to the reduction in the frequency of the 6th order harmonic.

The performance of the CCSFF and BRLS adaptive filter is mainly shown at 360 rpm and 1800 rpm. It is seen in figure 6.10 that at 1800 rpm the current is less distorted and more sinusoidal without CCSFF or BRLS. To determine at which speed the performance of the PLL overtakes the CCSFF and BRLS the THD of the (6 ± 1)th order harmonic of the phase a current is illustrated for different speeds while running the PMSM with PLL, CCSFF, or BRLS. The result is illustrated in figure 6.15.
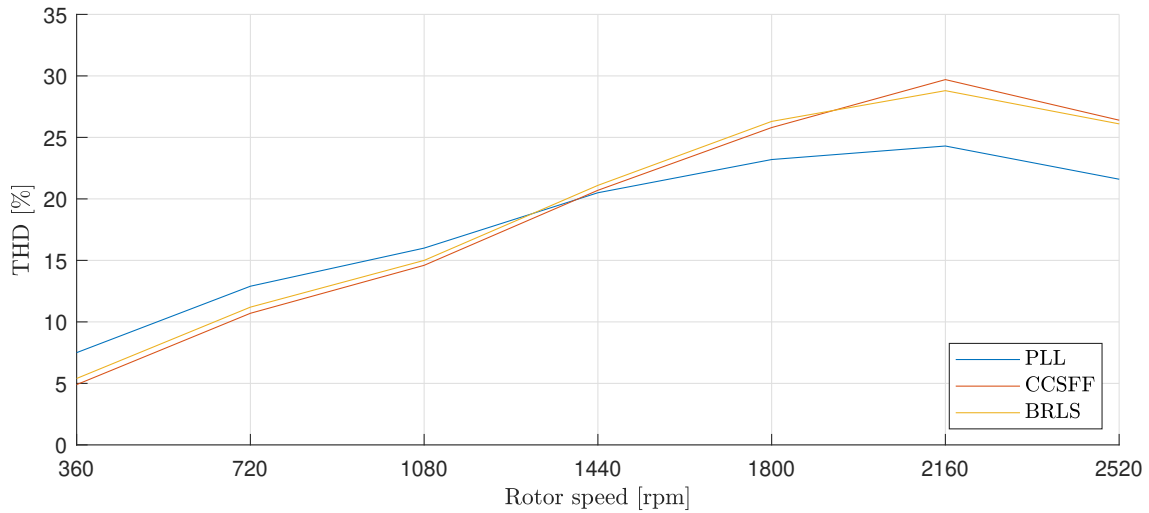
Figure 6.15. THD of the (6 ± 1)th order harmonic in the phase a current for PLL, CCFF, and BRLS at different speeds.

It is seen that at low speed the CCSFF and BRLS adaptive filter perform better than the PLL as expected. At approximately 1300 rpm the PLL starts to perform better than the CCSFF and BRLS when comparing the phase a current. It is seen that the THD for PLL, CCSFF, and BRSL all increases until 2160 rpm. After 2160 rpm the THD starts to decrease. The reason for this may be due to even larger phase shift.

Looking at the THD of the phase a current in figure 6.15 it is seen that regardless of the filter or speed, the THD is larger than 5 %. As the speed increases the THD increases significantly as well. Due to high phase delay it is not expected that the 6th order harmonic can be suppressed fully regardless of the speed. Even at low speed the phase delay from measuring i_q to the compensation limits the suppression capability. Due to poor performance in the phase a current, other methods such as voltage error compensation may be reconsidered for this system.

Conclusion 7

The objective of this thesis is to detect and suppress the (6 ± 1)th order harmonic distortion in the estimated flux corresponding to a 6th order harmonic component in the estimated position and speed caused by voltage source inverter (VSI) nonlinearities and flux spatial harmonics. Two methods are presented to filter the estimated flux. The first method is a complex-coefficient synchronous frequency filter (CCSFF) with zero phase shift in steady state. The dynamic performance and the harmonic suppression capability of the CCSFF heavily depend on the parameter design. Thus, to ensure sufficient harmonic suppression, the bandwidth should be designed to be less than the corresponding 6th order harmonic component. This implies that the operating speed range of the PMSM application should be considered. Designing the bandwidth to be low, degrades the dynamic performance of the control system, hence phase shift is added to the position estimation during speed and load changes. However, adopting an adaptive approach to the parameter design, which increases the bandwidth of the CCSFF system when a difference in the reference and estimated speed occurs improves the dynamic performance.

The second method presented is a bilinear recursive least squares (BRLS) adaptive filter. This method does not affect the dynamic performance of the control system as similar response in the position error is seen when e.g. the load condition is changed instantaneously compared to when none of the two methods are applied. The BRLS adaptive filter is capable of ensuring sufficient harmonic suppression capability. Regardless of the operation speed of the PMSM and the parameters of the PLL, the 6th order harmonic component in the estimated position and speed is reduced to be insignificant.

Despite proper suppression of the 6th order harmonic component in the estimated position and speed with CCSFF or BRLS, the sensorless performance is not improved significantly. The q-axis current still contain high 6th order ripples meaning torque ripple are present even though the q-axis current reference is without 6th order ripples. Thus, the filtering approach for harmonic suppression is not a thorough solution for harmonic suppressing of the current since the 6th order ripple is not appropriately compensated.

Future work 8

This thesis presents two methods to suppress the 6th order harmonic component in the estimated position and speed. The CCSFF is presented in chapter 4. The chapter presents proper design guidelines to easily design the parameters of the CCSFF depending on the desired suppression capability. The BRLS is presented in chapter 5. The influence of the BRLS algorithm parameters λ and σ are analyzed experimentally. However, gaining a deeper comprehension of the BRLS algorithm may pave the way for establishing comparable design guidelines as those applied to the CCSFF. This may result in a more theoretical method of selecting proper values for λ and σ.

In section 6.2 the effects of the harmonic suppression in the estimated position and speed are examined. It is observed that despite proper suppression of the 6th order harmonic component in the estimated position and speed, 6th order harmonic ripples are seen in the q-axis current. When the PMSM is run at 360 rpm, the corresponding 6th order harmonic component in the q-axis current is reduced using the presented methods. However, the ripples are not completely removed. Increasing the speed of the PMSM, decrease the effects of smooth estimated position and speed in the q-axis current. Thus, for future works, different topics are relevant to explore.

The two presented methods suppress the 6th order harmonic component in the estimated speed, leading to a smooth reference q-axis current. However, the current controller is not fast enough to compensate for the 6th order harmonic ripples caused by the inverter nonlinearities and flux spatial harmonics. An analysis of the control system including the voltage error can advantageously be performed. This includes derivation of the system's transfer function, which includes the voltage error. This can be used to analytically examine the effects of the nonlinearities of the VSI and flux spatial harmonics.

Furthermore, voltage error compensation may be considered as an addition to the two presented methods. By actively compensating the command voltage, the distortion in the currents may be reduced and improve the sensorless performance.

Bibliography

Allaoui et al., **2021**. Samia Allaoui, Yahia Laamari, Kheireddine Chafaa and Saad Salah. *Position and Speed Estimation of PMSM Based on Extended Kalman Filter Tuned by Biogeography-Based-Optimization*. 2021. doi: 10.18280/jesa.540405.

Boldea et al., **2008**. Ion Boldea, Mihaela Codruta Paicu and Gheorghe-Daniel Andreescu. *Active Flux Concept for Motion-Sensorless Unified AC Drives*. IEEE Transactions on Power Electronics, 2008. doi: 10.1109/TPEL.2008.2002394.

Bolognani et al., **2003**. S. Bolognani, L. Tubiana and M. Zigliotto. *EKF-based sensorless IPM synchronous motor drive for flux-weakening applications*. IEEE Transactions on Industry Applications, 2003. doi: 10.1109/TIA.2003.810666.

Chen et al., **2020**. Dunzhi Chen, Kaiyuan Lu and Dong Wang. *An I-f Startup Method for Back-EMF based Sensorless FOC of PMSMs with Improved Stability During the Transition*. 2020. doi: 10.1109/INDEL50386.2020.9266266.

Christiansen and Clausen, **2022**. Emil Christiansen and Kasper Juul Clausen. *MTPA control with AC compensation to minimize the copper loss in IPMSM under load varying conditions for compressors*. Master program, 3. semester, 2022.

Dhaouadi et al., **1991**. R. Dhaouadi, N. Mohan and L. Norum. *Design and implementation of an extended Kalman filter for the state estimation of a permanent magnet synchronous motor*. IEEE Transactions on Power Electronics, 1991. doi: 10.1109/63.85891.

Freijedo et al., **2011**. Francisco Freijedo, Alejandro Yepes, Jano Malvar, Oscar Lopez, Pablo Fernández-Comesaña, Ana Vidal and J. Doval-Gandoy. *Frequency tracking of digital resonant filters for control of power converters connected to public distribution systems*. Power Electronics, IET, 2011. doi: 10.1049/iet-pel.2010.0209.

Kim et al., **2010**. Sam-Young Kim, Wootaik Lee, Min-Sik Rho and Seung-Yub Park. *Effective Dead-Time Compensation Using a Simple Vectorial Disturbance Estimator in PMSM Drives*. IEEE Transactions on Industrial Electronics, 2010. doi: 10.1109/TIE.2009.2033098.

Krause et al., **2013**. Paul C. Krause, Oleg Wasynczuk, Scott D. Sudhoff and Steven D. Pekarek. *Analysis of Electric Machinery and Drive Systems*. John Wiley & Sons, 2013. ISBN 978-1118024294.

Lee and Ha, **2012**. Kwangwoon Lee and Jung-Ik Ha. *Evaluation of Back-EMF Estimators for Sensorless Control of Permanent Magnet Synchronous Motors*. Journal of Power Electronics, 2012. doi: 10.6113/JPE.2012.12.4.604.

Lin et al., **2019**. Hao Lin, Abraham M. Alcaide, Feng Wu, Jianxing Liu, Hao Luo, Leopoldo Franquelo and Ligang Wu. *MRAS-Based Sensorless Control of PMSM with BPN in Prediction Mode*. 2019. doi: 10.1109/ISIE.2019.8781197.

Lina et al., **2014**. Wang Lina, Xiao Kun, Liliana de Lillo, Lee Empringham and Pat Wheeler. *PI controller relay auto-tuning using delay and phase margin in PMSM drives*. Chinese Society of Aeronautics and Astronautics and Beihang University, 2014. doi: 10.1016/j.cja.2014.10.019.

Park and Sul, **2012**. Yongsoon Park and Seung-Ki Sul. *A Novel Method Utilizing Trapezoidal Voltage to Compensate for Inverter Nonlinearity*. IEEE Transactions on Power Electronics, 2012. doi: 10.1109/TPEL.2012.2192451.

Seilmeier and Piepenbreier, **2015**. Markus Seilmeier and Bernhard Piepenbreier. *Sensorless Control of PMSM for the Whole Speed Range Using Two-Degree-of-Freedom Current Control and HF Test Current Injection for Low-Speed Range*. IEEE Transactions on Power Electronics, 2015. doi: 10.1109/TPEL.2014.2353215.

Wang et al., **2017**. Dong Wang, Kaiyuan Lu, Peter Omand Rasmussen and Zhenyu Yang. *Comparative Study of Low-Pass Filter and Phase-Locked Loop Type Speed Filters for Sensorless Control of AC Drives*. CES TRANSACTIONS ON ELECTRICAL MACHINES AND SYSTEMS, 2017. doi: 10.23919/TEMS.2017.7961343.

Wang et al., **2019**. Dong Wang, Kaiyuan Lu and Peter Omand Rasmussen. *Improved Closed-Loop Flux Observer Based Sensorless Control Against System Oscillation for Synchronous Reluctance Machine Drives*. IEEE Transactions on Power Electronics, 2019. doi: 10.1109/TPEL.2018.2865348.

Wang et al., **2018**. Hechao Wang, Kaiyuan Lu, Dong Wang and Frede Blaabjerg. *Pulse-Injection-Based Sensorless Control Method with Improved Dynamic Current Response for PMSM*. 2018. doi: 10.23919/IPEC.2018.8507823.

Wu et al., **2020**. Xuan Wu, Sheng Huang, Kan Liu, Kaiyuan Lu, Yashan Hu, Wenli Pan and Xiaoyan Peng. *Enhanced Position Sensorless Control Using Bilinear Recursive Least Squares Adaptive Filter for Interior Permanent Magnet Synchronous Motor*. IEEE Transactions on Power Electronics, 2020. doi: 10.1109/TPEL.2019.2912868.

Wu et al., **2022**. Xuan Wu, Xu Yu, Ting Wu, Kaiyuan Lu, Shoudao Huang, Hesong Cui and Shuangquan Fang. *Complex-Coefficient Synchronous Frequency Filter-Based Position Estimation Error Reduction for Sensorless IPMSM Drives*. IEEE Transactions on Power Electronics, 2022. doi: 10.1109/TPEL.2022.3193221.

Xie et al., **2016**. Ge Xie, Kaiyuan Lu, Sanjeet Kumar Dwivedi, Jesper Riber Rosholm and Frede Blaabjerg. *Minimum-Voltage Vector Injection Method for Sensorless Control of PMSM for Low-Speed Operations*. IEEE Transactions on Power Electronics, 2016. doi: 10.1109/TPEL.2015.2426200.

Zhang et al., **2021**. Qiaofen Zhang, Haohao Guo, Chen Guo, Yancheng Liu, Dong Wang, Kaiyuan Lu, Zhenrui Zhang, Xuzhou Zhuang and Dunzhi Chen. *An adaptive proportional-integral-resonant controller for speed ripple suppression of PMSM drive due to current measurement error*. International Journal of Electrical Power & Energy Systems, 2021. doi: https://doi.org/10.1016/j.ijepes.2021.106866.

Zhang et al., **2022**. Qiaofen Zhang, Haohao Guo, Yancheng Liu, Chen Guo, Kaiyuan Lu, Dong Wang, Zhenrui Zhang and Jianbo Sun. *Robust plug-in repetitive control for speed smoothness of cascaded-PI PMSM drive*. Mechanical Systems and Signal Processing, 2022. doi: https://doi.org/10.1016/j.ymssp.2021.108090.

Zigmund et al., **2011**. Branislav Zigmund, Angela A Terlizzi, Xavier del Toro Garcia, Rastislav Pavlanin and Ligui Salvatore. *Experimental Evaluation of PI Tuning Techniques for Field Oriented Control of Permanent Magnet Synchronous Motors*. Advances in Electrical and Electronic Engineering, 2011.

A.1 Control parameters

Controller	K_p	K_i
Speed loop	0.6	6
Current loop d-axis	4.6	840
Current loop q-axis	7.9	840
CLFO	50	100

Table A.1. PI parameters utilized in the sensorless control system.